

10-25-2022 9:30 AM

Development of a two-axis cyclic loading device for mechanical testing of glenoid component fixation

Cintya Tavares, *The University of Western Ontario*

Supervisor: Ferreira, Louis, *The University of Western Ontario*

A thesis submitted in partial fulfillment of the requirements for the Master of Engineering Science degree in Mechanical and Materials Engineering

© Cintya Tavares 2022

Follow this and additional works at: <https://ir.lib.uwo.ca/etd>



Part of the [Biomechanical Engineering Commons](#)

Recommended Citation

Tavares, Cintya, "Development of a two-axis cyclic loading device for mechanical testing of glenoid component fixation" (2022). *Electronic Thesis and Dissertation Repository*. 8939.
<https://ir.lib.uwo.ca/etd/8939>

This Dissertation/Thesis is brought to you for free and open access by Scholarship@Western. It has been accepted for inclusion in Electronic Thesis and Dissertation Repository by an authorized administrator of Scholarship@Western. For more information, please contact wlsadmin@uwo.ca.

Abstract

The fundamental mechanism of aseptic glenoid component loosening, the rocking horse phenomenon, is a reaction to glenohumeral articular forces that are not centered on the component. While glenoid component loosening remains a problem, the underlying mechanisms that lead to fixation failure at the bone-component contact remain controversial. Several studies employing the ASTM F2028 technique have successfully recreated the rocking horse effect. However, no obvious strategy to decrease component loosening has been presented. This thesis investigates the behavior of forces that lead to component loosening on cyclically loaded components using three different protocols and testing apparatuses—a Stewart Platform, a cyclic loading experimental rig, and an ASTM F2028-17-compliant version of the experimental rig. The experimental assessment of response forces acting on the glenoid implant is a desired outcome since it can be used to compare implant designs and allows for controlled testing of alternative materials for prosthesis advancement to lessen the stresses that produce the rocking horse phenomena.

Keywords

Total Shoulder Arthroplasty, Glenoid Implant, Reaction Forces, Stewart Platform, Experimental Apparatus, Rocking Horse Phenomenon, Glenoid Loosening

Summary for Lay Audience

A variety of disorders can cause shoulder discomfort and impairment, prompting patients to seek partial or complete shoulder joint replacement surgery. The shoulder is classified as a nonconforming ball-and-socket joint. The ball, which is the spherical head of the upper arm bone, is inserted into the glenoid, a shallow socket in the shoulder. To restore the shoulder's function, total shoulder arthroplasty (TSA), the gold standard for surgical treatment of severe shoulder osteoarthritis, involves replacing both the ball and socket with artificial components that closely resemble the natural shape of the bones. TSA results in decreased pain and greater mobility; nevertheless, glenoid loosening, a serious side effect that can develop years after surgery and cause postoperative discomfort, function limitations, and occasionally the need for revision surgery, is still a major concern. The mechanism behind glenoid loosening is called the rocking horse phenomenon, or edge loading. It develops from the ball prosthesis' repetitive motion on the glenoid implant's surface. During edge loading, the glenoid component is compressed against its bone fixation on one side, while experiencing lift on the opposite side. Ultimately, this repetitive movement causes the implant to become detached from its bone fixation. An indispensable factor in determining the incidence of wear and loosening as well as the recommended activity levels for patients following TSA is the amount of load that the prosthetic glenoid component is subjected to during edge loading. This thesis focuses on the design and implementation of a testing apparatus designed to simulate edge loading to evaluate the behavior of the forces acting on aseptic glenoid implants. The testing device's performance was evaluated, and its capacity to reproduce the rocking horse phenomena was validated. Further testing of the device compares various implant types and assesses their response to cyclic stresses. The findings in this body of work support the theory that glenoid prosthetic design has an impact on response forces under cyclic loading, with increased stress loading being detected when the humeral head travels further from the component's center.

Co-Authorship Statement

Chapter 1:	Cintya Tavares - sole author
Chapter 2:	Cintya Tavares - study design, data collection, wrote manuscript Louis Ferreira - study design
Chapter 3:	Cintya Tavares - study design, data collection, wrote manuscript Louis Ferreira - study design
Chapter 4:	Cintya Tavares - study design, data collection, wrote manuscript Louis Ferreira - study design
Chapter 5:	Cintya Tavares - sole author

Dedication

Although it is implausible that my beloved mother, Lucia Dos Anjos De Almeida Tavares, will ever read these words as she passed away in 2018, I would like to dedicate this body of work to her because her love and support have given me strength and determination my entire life. I am tremendously grateful for everything my mother has taught me, and I feel very blessed to have witnessed what it means to be a strong woman. In honor of the sacrifices she made for her family, as well as the love, dedication, and wisdom she provided, I dedicate not only this body of work but everything I do right in my lifetime, to her.

"When I lost you, I believed I had lost everything since you were my everything, yet your love remained in me, and because of that, I am still breathing."

Acknowledgments

To my friends and family for being there for me during this emotional rollercoaster and for keeping me grounded while my mind was whirling. I want to express my gratitude to my father, Joaquim Tavares, and my siblings, Herminia and Braulio Tavares. This has been a very challenging period for all of us, I want to acknowledge it and, to some extent, forever keep a recollection of this. Thanks to your love, support, and compassion, I am able to conclude this chapter of my life.

I want to express my gratitude to the entire HULC team, in particular, Jonathan, Jakub, and Corey. Working with and learning from you has been a worthwhile experience. I wish you success in whatever endeavor you decide to pursue next. I have had the gratifying and special opportunity to get both engineering and clinical views while working at the HULC lab. Finally, I want to thank Dr. Louis Ferreira, my supervisor, for providing me with this opportunity. I will always remember the valuable lessons you taught me.

Table of Contents

Abstract	ii
Summary for Lay Audience	iii
Co-Authorship Statement	iv
Dedication	v
Acknowledgments	vi
Table of Contents	vii
List of Tables	x
List of Figures	xi
List of Abbreviations	xiv
Chapter 1	1
1 Introduction	1
1.1 Glenohumeral Joint	2
1.1.1 Glenoid Morphology	3
1.2 Glenohumeral Forces on the Glenoid	10
1.3 Force Measurement Methodologies	11
1.4 Total Shoulder Arthroplasty	13
1.4.1 Glenoid Implant	14
1.4.2 Walch Classification	17
1.5 The Rocking Horse Phenomenon	20
1.5.1 Standard Test Methods for Dynamic Evaluation of Glenoid Loosening or Disassociation	21
1.6 Rationale	23
1.7 Objectives and Hypothesis	24
1.8 Thesis Overview	26
Chapter 2	27

2	Development of Reaction Force Test protocol using a 6-DOF loading apparatus	27
2.1	Introduction.....	28
2.2	Materials and Methods.....	30
2.2.1	Data Acquisition	30
2.2.2	Specimen Design	31
2.2.3	Experimental Protocol	35
2.3	Results and Discussion	36
2.3.1	6-DOF Loading Protocol	36
2.4	Chapter Summary	43
	Chapter 3	45
3	Preliminary Development of a Cyclic Loading Simulator for Stress Analysis	45
3.1	Introduction.....	46
3.2	Experimental Setup.....	46
3.2.1	Cyclic Loading Simulating System	46
3.2.2	Experimental Protocol	49
3.3	Results and Discussion	49
3.4	Chapter Summary	57
	Chapter 4.....	60
4	Development and Application of a Testing Protocol for Glenoid Cyclic Loading Simulation	60
4.1	Introduction.....	61
4.2	Materials and Methods.....	62
4.2.1	Specimen Selection.....	62
4.2.2	Specimen Preparation	65
4.2.3	Cyclic Loading Testing Frame.....	69
4.3	Loading Protocol.....	72

4.3.1	Results.....	73
4.3.2	Analysis.....	84
4.4	Chapter Summary	88
Chapter 5	90
5	Conclusion	90
5.1	Summary	91
5.2	Strengths and Limitations	94
5.3	Future Work and Conclusion	95
References	97
Appendix A:	Developed Experimental Apparatus Component Drawings	115
Appendix A1:	Vacuum-system Attachment Components and Splash Component Parts Drawings	122
Appendix B:	Supplementary Tables of the Test Results Presented in Chapters 3 and 4.....	126
Appendix C:	Experimental Apparatus Pilot Test Results Plots and Tables	129
Curriculum Vitae	134

List of Tables

Table 1.1: Summary of Glenoid Height Test Results [11]–[13].....	5
Table 1.2: Summary of Glenoid Width Test Results [12]–[15].....	6
Table 1.3: Walch Glenoid Morphological Classification [95]–[98].	19
Table 2.1: Average Loads – Stewart Platform.....	36
Table 3.1: Average loads – Cyclic Loading Device.	50
Table 4.1: Summary of Test Results using the Keeled Inlay Implant Group.	74
Table 4.2: Summary of Test Results using the Pegged Inlay Implant Group.....	75
Table 4.3: Summary of Test Results Using the Keeled Onlay Implant Group.....	76
Table 4.4: Summary of Test Results Using the Pegged Onlay Implant Group.	77
Table 4.5: Summary of ANOVA Results – Keeled Inlay Group.	80
Table 4.6: Summary of ANOVA Results – Pegged Inlay Group.	80
Table 4.7: Summary of ANOVA Results – Keeled Onlay Group.....	81
Table 4.8: Summary of ANOVA Results – Pegged Onlay Group.	81
Table 4.9: Summary of F_z Mean of all samples.	82
Table 4.10: Summary of t-test Results - Keeled Implant.....	82
Table 4.11: Summary of t-test Results - Pegged Implant.	82
Table 4.12: Summary of ANOVA results - KI, KO, PI, PO.....	83
Table 4.13: Welch's t-test results – KI, KO, PI, PO	83

List of Figures

Figure 1.1: Clinical CT imagery of a Skeleton's Right Glenohumeral Joint [2].	2
Figure 1.2: Anterior and Lateral Views of the Left Scapula [5].	3
Figure 1.3: Parameters of glenoid anatomy include (A) glenoid height, (B) width, and (C) version [10].	4
Figure 1.4: Glenoid Height (red) and Glenoid Width (green) [14].	5
Figure 1.5: Illustration of the Glenoid Vault Cross-section [35].	8
Figure 1.6: Illustration of the Glenoid Center Line.	9
Figure 1.7: Components of Total Shoulder Arthroplasty [62].	13
Figure 1.8: Illustrations of Pear-shaped (A) and Oval-shaped (B) Glenoid Components [71].	15
Figure 1.9: Walch Glenoid Morphology Classification [35].	18
Figure 1.10: Illustration Demonstrating the Rocking Horse Phenomenon [99].	20
Figure 2.1: The Stewart Platform developed at the HULC lab. Critical components are labeled.	29
Figure 2.2: Load Cell Axis Indicating the Positive Axis Directions.	31
Figure 2.3: Design of the Rectangular Design Test Component.	32
Figure 2.4: Design of the Triangular Design Test Component.	33
Figure 2.5: Design of the Concave Test Part.	34
Figure 2.6: Design of the Attachment Base Component.	35
Figure 2.7: Rectangular Design Test Results Plot using 300N Applied Load.	37

Figure 2.8: Rectangular Design Test Results Plot using 500N Applied Load.....	37
Figure 2.9: Rectangular Design Test Results Plot using 700N Applied Load.....	38
Figure 2.10: Triangular Design Test Results Plot using 300N Applied Load.	39
Figure 2.11: Triangular Design Test Results Plot using 500N Applied Load.	39
Figure 2.12: Triangular Design Test Results Plot using 700N Applied Load.	40
Figure 2.13: Concave Design Test Results Plot using 300N Applied Load.	41
Figure 2.14: Concave Design Test Results Plot using 500N Applied Load.	41
Figure 2.15: Concave Design Test Results Plot using 700N Applied Load.	42
Figure 3.1: Custom-made Hexapod configuration described in Chapter 2.	47
Figure 3.2: Custom-made Cyclic Loading Test Apparatus Configuration. Critical components are labeled.	48
Figure 3.3: Rectangular Design Test Results Plot using 300N Applied Load.....	51
Figure 3.4: Rectangular Design Test Results Plot using 500N Applied Load.....	51
Figure 3.5: Rectangular Design Test Results Plot using 700N Applied Load.....	52
Figure 3.6: Triangular Design Test Results Plot using 300N Applied Load.	53
Figure 3.7: Triangular Design Test Results Plot using 500N Applied Load.	54
Figure 3.8: Triangular Design Test Results Plot using 700N Applied Load.	54
Figure 3.9: Concave Design Test Results Plot using 300N Applied Load.	55
Figure 3.10: Concave Design Test Results Plot using 500N Applied Load.	56
Figure 3.11: Concave Design Test Results Plot using 700N Applied Load.	56
Figure 4.1: Models of the Normal (left) and B2 (right) Sawbone Scapulae [129].	63

Figure 4.2: Small-Keeled Glenoid Implant (left) and Medium-Pegged Glenoid Implant (right) [129].	64
Figure 4.3: Normal Keeled Implant Placement (top) B2 Pegged Implant Placement (bottom) [129].	65
Figure 4.4: Isolated B2 (top) and Normal (bottom) Specimens.	66
Figure 4.5: Cementing Method including the Liquid Container and Vacuum System.	67
Figure 4.6: Vacuum-based holding System attachment Components.	68
Figure 4.7: Vacuum-based holding System attachment Components for the Small (left) and Medium (right) Specimens.	68
Figure 4.8: Splash Protection Components mounted onto a Test Specimen.	69
Figure 4.9: Affinis® CoCr Humeral Head Component.	70
Figure 4.10: Component SI Alignment Process using the Apparatus' Optical Laser Feature.	71
Figure 4.11: Cyclic Testing Frame including the Photoelectric Sensor and Digital Counter for Cycle counting.	72
Figure 4.12: F _z versus Time graph for the Keeled Inlay Implant Group.	78
Figure 4.13: F _z versus Time graph for the Pegged Inlay Implant Group.	78
Figure 4.14: F _z versus Time graph for the Keeled Onlay Implant Group.	79
Figure 4.15: F _z versus Time graph for the Pegged Onlay Implant Group.	79
Figure 4.16: Average F _z Mean for all groups.	84
Figure 4.17: Glenoid Quadrants.	85

List of Abbreviations

ASTM	American society for testing and materials
AP	Anteroposterior
BW%	Bodyweight percentage
CT	Computed tomography
DOF	Degree of freedom
FEA	Finite element analysis
GC	Glenoid cavity
GCL	Glenoid center line
GHJ	Glenohumeral joint
N	Newtons
TSA	Total shoulder arthroplasty
SI	Superoinferior

Chapter 1

1 Introduction

OVERVIEW: Total shoulder arthroplasty (TSA) is an increasingly popular surgical procedure to restore shoulder function. During surgery, the damaged joint in the shoulder is replaced with a prosthesis to restore its function. One of the most common failure modes of TSA is glenoid loosening, which can lead to postoperative pain, functional limitations, and in some cases revision surgery. This chapter focuses on concepts related to the anatomy of glenoid implants and the mechanisms behind the rocking horse phenomenon, a major cause of implant loosening. An overview of shoulder joint composition is explained and insights into TSA are presented, with a particular interest in the rocking horse phenomenon. The chapter concludes with the rationale, goals, and assumptions relevant to the current work.

1.1 Glenohumeral Joint

The glenohumeral joint, or shoulder joint, is a nonconforming ball and socket joint that connects the scapula to the humerus (Figure 1.1). It is the main connection between the upper limb and the trunk. The scapula is the primary bone structure of the shoulder, where all the muscles connect. Abduction, adduction, flexion, extension, and internal and external rotation are only a few of the modes of body motion of the shoulder muscles [1].

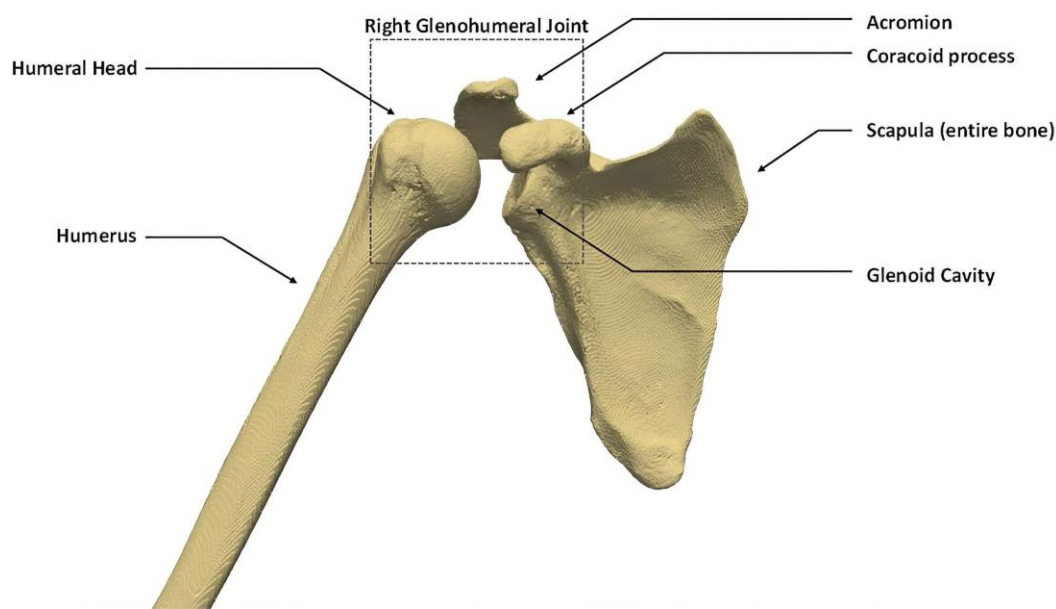


Figure 1.1: Clinical CT imagery of a Skeleton's Right Glenohumeral Joint [2].

The major components of the glenohumeral joint are shown, and the scapula and humerus are also shown.

The glenoid fossa, commonly referred to as the glenoid, is a shallow cup-like structure located on the lateral portion of the scapula (Figure 1.2). Hyaline cartilage covers the glenoid and it is characterized by having a thinner central circular part known as a "bare area." The cartilage is thickest near the edges and thinnest in the center [3]. A region of subchondral bone thickening known as the "Asskay tubercle" lies beneath this thin layer of cartilage [4].

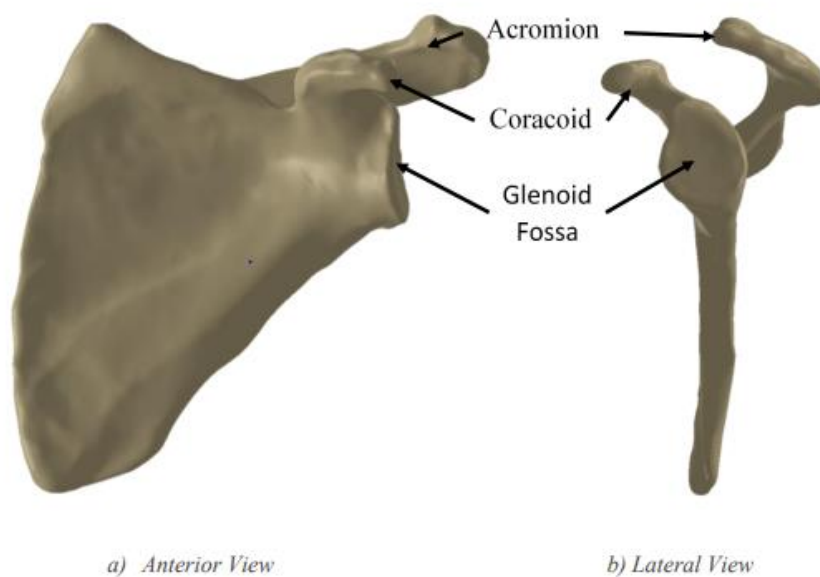


Figure 1.2: Anterior and Lateral Views of the Left Scapula [5].

The glenoid fossa, coracoid, and acromion are shown for the left scapula of the shoulder.

While the nature of the glenoid allows a wide range of movement for the glenohumeral joint, it provides a low degree of stability. It is one of the most movable joints in the human body due to the free joint capsule and the general size of the humeral head compared to the shallow glenoid fossa (4:1 proportion in surface region). Because of its higher mobility, it is usually the most dislocated joint [6], [7].

The current work will focus on the glenoid portion of the glenohumeral joint, discussing the anatomy of this component and addressing key factors that influence the efficiency of TSA procedures.

1.1.1 Glenoid Morphology

The glenoid cavity (GC), or glenoid fossa, is located laterally and superiorly at the end of the scapula. This articular surface varies greatly when it comes to its morphology. In the upper anterior part of the edge of the glenoid, there is a notch that affects the shape of the glenoid cavity. The shape of the glenoid cavity can be classified as one of three distinct morphological types: pear, oval, and comma-shaped [3].

The glenoid fossa plays an important role in the motion of the humeral head during abduction, as it provides its vertical axis; during the elevation of the arm to the height of the shoulder, the humeral head moves into the smaller upper portion of the GC, which is extended by the labrum. By limiting the humerus' anterior and posterior excursion, the glenoid labrum, a wedge-shaped structure that surrounds the glenoid cavity, appears to provide natural stability to the glenohumeral joint [8]. This structure consists of hyaline cartilage, fibrocartilage, and fibrous tissue [9].

The size and structure of the GC as well as its connection with the labrum, are crucial for the usual activity of this immensely adaptable joint of the human body. These factors are also important in the preparation for total shoulder arthroplasty prosthesis measurement, location, and design.

Glenoid height, width, articular surface area, inclination, vault size and shape, and version are anatomic features of the glenoid that are relevant to prosthetic design (Figure 1.3). These characteristics have shown significant regular variation in several cadaveric tests; this fluctuation has an impact on prosthetic design, equipment, and intraoperative implantation procedures.

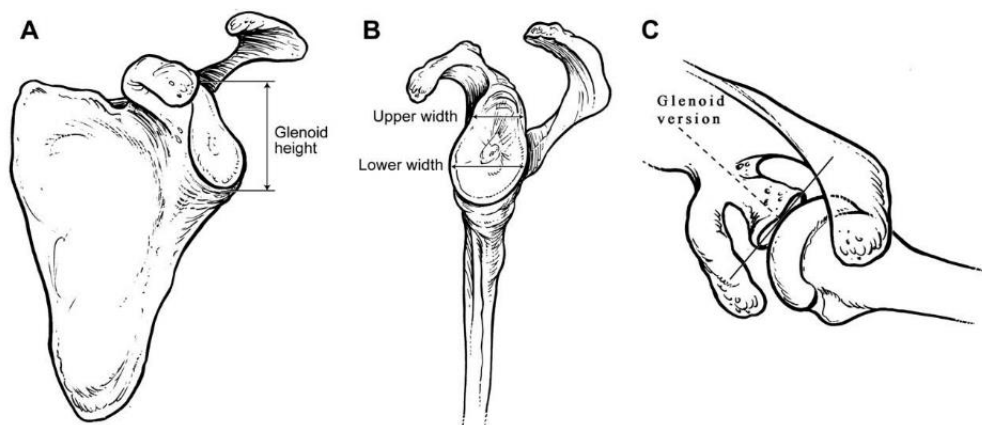


Figure 1.3: Parameters of glenoid anatomy include (A) glenoid height, (B) width, and (C) version [10].

Glenoid Height

Glenoid height constitutes the distance between the most superior point and the most inferior point of the glenoid (Figure 1.3). This measurement describes the shape of the shoulder joint. Several studies have reported mean glenoid heights averaging between 35.1 mm to 38 mm, with women having smaller sizes compared to men [11]–[13]. Table 1.1 shows a summary of the studies regarding glenoid height. It is crucial to note that each test uses unique processes with a different level of precision and accuracy.

Table 1.1: Summary of Glenoid Height Test Results [11]–[13].

<i>Authors</i>	<i>Sample Size</i>	<i>Glenoid Height (mm)</i>	<i>Range (mm)</i>
<i>Checroun et al.</i>	412	37.9	31.2 - 50.1
<i>Iannotti et al.</i>	140	39	30 - 48
<i>Sharkey et al.</i>	5	35.1	29.9 - 38.8
<i>Kwon et al.</i>	12	37.8	30 - 47
<i>Churchill et al.</i>	344	37.5 (male)	30.4 - 42.6 (male)
		32.6 (female)	29.4 - 37 (female)
<i>Mallon et al.</i>	28	38 (male)	33 - 45 (male)
		36.2 (female)	32 - 43 (female)

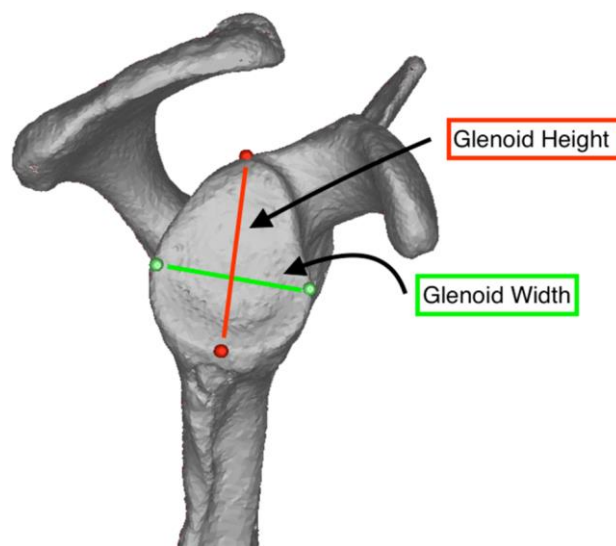


Figure 1.4: Glenoid Height (red) and Glenoid Width (green) [14].

Glenoid Width

Glenoid width refers to the distance between the glenoid's most anterior and most posterior points. It is determined by the glenoid's overall shape (Figure 1.4). In a study conducted by Checroun et al., 71% of the 412 glenoids sampled were pear-shaped, while the rest was elliptical [11]. They reported that the upper width of pear-shaped glenoids is smaller than the lower width. The glenoid width investigations indicate a mean average of 23 mm to 29 mm, with variances between upper and lower width as well as disparities between males and females [12]–[15]. Table 1.2 presents a summary of the tests involving glenoid width. No difference was observed in glenoid width between white and black patients' specimens [13].

Table 1.2: Summary of Glenoid Width Test Results [12]–[15].

<i>Authors</i>	<i>Sample Size</i>	<i>Glenoid Width (mm)</i>	<i>Range (mm)</i>
<i>Iannotti et al.</i>	140	23 (upper width)	18 - 30 (upper width)
		29 (lower width)	21 - 35 (lower width)
<i>Kwon et al.</i>	12	26.8	22 - 35
<i>Churchill et al.</i>	344	27.8 (male)	24.3 - 32.5 (male)
		23.6 (female)	19.7 - 26.3 (female)
<i>Mallon et al.</i>	28	28.3 (male)	24 - 32 (male)
		23.6 (female)	17 - 27 (female)

Glenoid Inclination

According to Hughes et al. [16], [17] and Maurer et al. [17], glenoid inclination is the angle formed by the bottom of the supraspinatus fossa and the glenoid fossa line: the β angle. In terms of surgery, the angle represents the global glenoid inclination and is useful for planning the implantation during total shoulder arthroplasty [17], [18].

Considerable variation in glenoid inclination was reported in the study of 344 cadaveric scapulae by Churchill et al [13]. The glenoid was superiorly inclined by 4 in male specimens (range, 7 inferior - 15.8 superior inclination), whereas in female specimens it

was superiorly inclined by 4.5 (range, 1.5 inferior - 15.3 superior inclination) [13]. The glenoid inclinations of white patients were marginally higher (mean, 4.6 superior inclination) than those of black individuals (mean, 3.9 superior inclination) [13].

Greater glenoid inclination has been linked to increased superior humeral translation in cadaveric studies, and imaging studies have shown increased glenoid inclination in shoulder specimens with rotator cuff injuries [19]–[22]. In contrast, Kandemir et al. [23] found no discernible difference in glenoid inclination between cadaveric specimens with healthy rotator cuffs and those with injuries.

Glenoid Version

The angular orientation of the glenoid articular surface axis relative to the long or transverse axis of the scapula is defined as glenoid version [10]. Glenoid retroversion is the term used to describe a posterior angle. In most studies, normal glenoid version was reported to be near 0°, with occasional moderate anteversion but more commonly with slight retroversion, with values typically less than 10° in either direction [12], [24]–[30]. In recent years, several studies have investigated glenoid version, with the majority citing a normal range of 2 anteversion to 9 retroversion, as well as alterations in version in the presence of glenohumeral disease [13], [24], [25], [31]. The average glenoid retroversion, according to Churchill et al., is 1.2 (range, 9.5 anteversion-10.5 retroversion). Men's glenoids were moderately more retroverted than women's (mean, 1.5 versus 0.9, respectively) in their examination of 344 cadaveric scapulae, while white patients' glenoids were significantly more retroverted than black patients' (mean, 2.7 against 0.2; P.00001)[13]. In a study of 28 cadaveric scapulae, Mallon et al. found a mean glenoid retroversion of 6 (range, 2 anteversion -13 retroversion)[12].

The mechanics of the glenohumeral joint are altered when it differs from the normal version, which can lead to instability and arthropathy. Deviation from the native version of the prosthetic shoulder has been demonstrated to increase glenoid component stress and wear [31]–[34]. As a result of these observations, it is now widely recommended that during shoulder arthroplasty, the glenoid version be normalized or neutralized.

Glenoid Vault

Glenoid vault is a structure that is present between the articular surface of the glenoid and the body of the scapula (Figure 1.5). It is mostly composed of cancellous bone delineated by a thin rim of cortical bone. The current generation of glenoid implants is designed to be fastened to the articular surface.

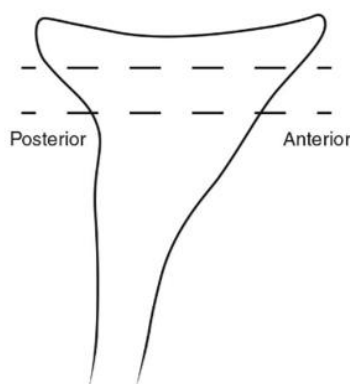


Figure 1.5: Illustration of the Glenoid Vault Cross-section [35].

The glenoid vault has a triangular shape, and it gets narrower from the lateral to the medial side. In TSA, this parameter is used as the bony support for a glenoid component.

When the articular surface is damaged, a glenoid component might be implanted if attached to the glenoid vault's endosteal surface. Codsi et al. [36] have described the shape and size of the glenoid vault. They used 3-dimensional (3D) computed tomography (CT) reconstructions of 61 cadaveric scapulae to assess variations in glenoid vault shape and size [36]. They were able to create a normalized glenoid vault model by normalizing the measured glenoid vault geometry to the SI glenoid height. In the SI dimension, the vault is approximately triangular throughout its whole length, according to this model [36]. In TSA, the fixation and stabilization of glenoid components depend upon the integrity of the subchondral bone of the glenoid fossa as well as the glenoid vault's cancellous bone.

Glenoid Centerline

Glenoid centerline (GCL) is the line perpendicular to an assumed articular surface when the joint has no deformities (Figure 1.5). The glenoid centerline is defined by Matsen et

al. as a line that begins at the glenoid's center, runs perpendicular to the articular surface, and exits on the anterior aspect of the scapular neck [37].

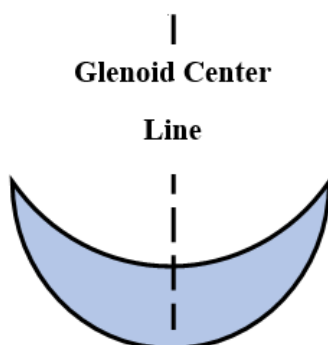


Figure 1.6: Illustration of the Glenoid Center Line.

Glenoid vault centerline is usually directed from lateral posterior to medial anterior.

This line crosses the glenoid face center.

The GCL is used as a reference point for locating the glenoid component of a shoulder prosthesis. For the GCL to be identified, the scapular spine must be included in the analysis.

The anatomy of the glenoid is still being studied. The glenoid has been demonstrated in studies to have various physical properties depending on ethnicity and gender [13], [38]–[40]. Aside from ethnic differences and gender, the results of these studies are influenced by a variety of factors such as imaging techniques, measurement methodologies, selection of comparison cases within identical groups, and inclusion of all characteristics that may have an impact on the study's outcomes. Despite the variation within the data of different studies, there is a consensus that the glenoid is usually somewhat retroverted and inclined superiorly. The height of a GC in a good condition is longer than its width, and male GCs are usually bigger than females GCs.

The study of the glenoid has revealed many important facts about the structure of the shoulder joint. As much as the glenoid is a key part of the shoulder joint, it also serves as an important reference point for measurements taken during surgery. This information is essential in the treatment of shoulder complications.

1.2 Glenohumeral Forces on the Glenoid

Shoulder biomechanics is dependent on a delicate balance of stability and mobility. Clinically, stabilization of the shoulder joint is accomplished by the compression of the humeral head into the glenoid cavity, also known as the concavity-compression mechanism. This process is reliant on the forces generated by the shoulder muscles as well as the design of the articular surfaces, particularly the glenoid. There are three types of muscle forces operating on the shoulder joint: compressive forces, superiorly-inferiorly directed forces, and anteriorly-posteriorly directed forces [41]. Compressive forces are responsible for the stabilization of the glenohumeral joint, whereas anterior, posterior, inferior, and superior forces, as well as translational forces, destabilize the shoulder joint [41]. Several factors, including the design of the prosthesis, the adequacy of the soft-tissue proportion, the cementing technique, the strength of the rotator cuff, and the stresses the patient applies to the prosthetic joint, influence the clinical stability of a glenoid component in total shoulder arthroplasty [42]. To comprehend the biomechanical effects of common shoulder pathologies and to create new therapeutic strategies aiming at regaining the healthy shoulder's articular mechanics, it is crucial to characterize the forces occurring at the glenohumeral joint. In the glenohumeral joint, reaction forces are mechanically equal in magnitude on the humeral and glenoid sides and operate to counterbalance the forces that the body's weight, applied stresses, or muscle contractions transfer through the articular surface. The possibility of glenoid component complications developing after shoulder arthroplasty, nonetheless, is significantly influenced by the force's direction. The rocking horse effect is one of these complications. During the rocking horse event, the humeral head is superiorly displaced as a consequence of contact forces that are imparted to the glenoid surface's perimeter, mainly as a result of rotator cuff tears.

Heretofore, the glenohumeral joint's contact forces were approximated using musculoskeletal models, quantified in vitro, or estimated in vivo via telemeterized shoulder implants [43]–[53]. In the literature, values have been expressed as a percentage of body weight (% BW) or as Newtons (N). According to published data, the glenohumeral contact forces (GHCFs) during abduction of the straight arm range from 43

to 90% BW, or 322 to 675 N for a person weighing 75 kg [43]–[53]. Additionally, studies have concentrated on GHCFs occurring during daily tasks, with peak glenohumeral contact forces ranging from 26 to 164 % of BW for numerous functional daily living activities [54]. The findings demonstrate that even during routine regular activities, the joint is subjected to significant stresses. The load delivered to the prosthetic glenoid component after total shoulder arthroplasty remains an important issue due to the potential for wear and loosening.

1.3 Force Measurement Methodologies

The quantification of force is assessed by a physical reaction to the application of force. When analyzing the bone's biomechanics, strain is a prominent outcome metric. Strain—a structural deformation—occurs when an outside force—stress—is applied to the bone. Because strain is determined by the ratio of the change in length to the initial length, it is conveyed as a nondimensional number. In vivo bone strain assessment was enabled through the advancement of adequate bonding and recording techniques. There are several experimental biomechanical bone strain measuring approaches available, with strain gauges, digital image correlation (DIC), and digital volume correlation (DVC) being particularly noteworthy.

Strain gauges, a form of a sensor whose resistance alters in direct proportion to the applied force, can be affixed to certain locations on the cortical shell of the bone to track the local strain. A measurable electrical signal is produced by strain gauges from the applied force, pressure, torque, etc. The resulting voltage change may be converted into a strain measurement approach by understanding the electrical and geometric properties of the gauge. While strain gauges are a significantly less invasive option that safeguards the native structure of the bone, they have limitations such as the inability to quantify internal strain, the requirement to record strains at distinct points to adequately categorize the distribution pattern of axial strain over a cross-section, and the possibility of strengthening the bone to which they are connected [55], [56]. The application of strain gauges is restricted to discrete cortical stresses since there has been little success in

establishing correlations between surface strains and internal bone strains [57]. Rather, internal bone behavior exhibits only a weak correlation with surface strains.

Digital image correlation is a non-contact method for computing the full-field surface stresses of loaded bone specimens. The essential premise of DIC is to capture images of the component both loaded and unloaded. Prior to mechanical testing, a heterogeneous pattern is painted on the surface of a bone specimen, and then, the images of the component before and after deformation are compared. The surface stresses on the bone may be calculated by comparing local displacements within the photographically depicted heterogeneous pattern [58]. As it can only measure the bone's surface and requires that the bone surface be exposed, digital image correlation is not a practical tool for evaluating the internal behavior of bone [58].

Digital volume correlation, which is the three-dimensional extension of digital image correlation, is a non-intrusive method for obtaining sub-surface material deformation and strain data. High-resolution images of the undeformed and deformed structures are used to capture the internal deformable registration in this approach. By calculating the full-field displacements between the images using digital volume correlation, full-field strains may subsequently be created from the full-field displacements. DVC, in combination with in-situ mechanical testing and one or more imaging modalities such as micro-computed tomography (micro-CT) imaging technologies, is currently the only approach capable of evaluating bone structure in 3D [59].

Micro-CT is a non-destructive, slice-by-slice 3D imaging method that uses X-rays to view the interior of objects and identify minute alterations in bone architecture. Micro-CT is a high-resolution imaging technique that generates images by measuring how much an x-ray beam of known intensity attenuates after passing through a region of interest. In this technique, multiple attenuated x-ray projections of the target volume are recorded using a revolving stage or rotating source. While capturing more projections improves picture quality, it also lengthens the acquisition process. The attenuated x-rays detected at the CT sensor are combined with the spatial information contained in each projection to create an image reconstruction algorithm that reconstructs the volume of interest [60].

1.4 Total Shoulder Arthroplasty

Total shoulder arthroplasty (TSA), or total shoulder replacement, is a common surgical procedure used to restore function to the shoulder joint. The surgery requires the replacement of a degraded natural glenoid of the shoulder joint with a new artificial glenoid component (Figure 1.6). This procedure is usually necessary for patients who experience pain caused by bone-on-bone contact. When shoulder pain is caused by osteoarthritis or a rotator cuff injury, shoulder replacement surgery is a possibility. Surgery is also used to treat avascular necrosis, rheumatoid arthritis, and significant fractures that occur as a result of trauma or a fall [61]. During the TSA procedure, the resected humeral head is exchanged by a circular, metal segment, and the glenoid is usually replaced by a polyethylene implant [8]. Pain relief, enhanced strength, increased range of motion, and improved mobility of the shoulder and arm are all common outcomes of the operation.



Figure 1.7: Components of Total Shoulder Arthroplasty [62].

In this medical procedure, the joint surfaces of the humerus and scapula are removed and replaced with artificial components. During the TSA procedure, the head of the humerus is exchanged by a ball-molded component. The socket portion of the joint is replaced with a small dish-like cup.

As with other total joint procedures including hip replacement, knee replacement, ankle replacement, wrist replacement, elbow replacement, carpal tunnel release, and spinal fusion, total shoulder arthroplasty is associated with a myriad of possible complications. The most common complication is glenoid implant loosening, which can lead to postoperative pain, limitation of function, and, in some cases, the need for revision surgery [63]–[65]. Other complications include periprosthetic failure, infection, instability of the glenohumeral joint, rotator cuff tears, neural injury, and dysfunction of the deltoid muscle [66]. The pathophysiology of glenoid component loosening is intricate, and it might be linked to patient features, surgical techniques, implant design, the integrity of the rotator cuff, infections, aseptic osteolysis, and soft tissue instability [67], [68]. These variables can cause impingements and/or excessive stress on the glenoid implant and/or its bone interface. As a result, implant loosening and repeated micromotion may occur.

1.4.1 Glenoid Implant

Currently, there is a variety of glenoid components in different shapes and sizes. Most glenoid implants are pear-shaped to resemble the anatomic shape of the glenoid; however, there are oval options available (Figure 1.8). The pear-shaped glenoid component may have the advantage of preventing nonarticular tissues from being impinged by overhanging polyethylene [69]. Nonetheless, a smaller top section of the component reduces the contact surface area as well as the wall height. The force required for dislocation or subluxation is theoretically reduced due to the lower wall height in the superior region of the component. The shape of the glenohumeral joint, as demonstrated by Jobe and Iannotti [70], influences the amount of articular surface area accessible for contact and consequently the range of motion.

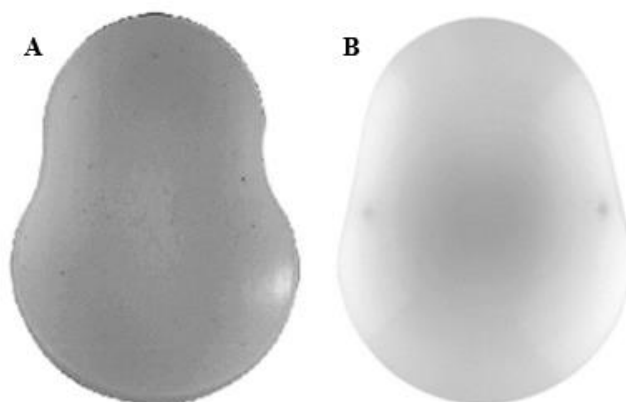


Figure 1.8: Illustrations of Pear-shaped (A) and Oval-shaped (B) Glenoid Components [71].

The anatomic glenoid is pear-shaped, with a smaller superior section; nonetheless, erosion and peripheral osteophyte proliferation flatten the surface of the glenoid surface in most arthritic shoulders, leading it to become more oval than comma-shaped. The utilization of oval implants with complete osseous support is possible because of this pathologic form. Additionally, these components have a wider and higher articulation surface area and superior wall height, which may require more effort to dislocate or subluxate [72], [73]. Regardless of the component chosen, the objective is to construct the glenoid appropriately to allow for minimal overhang. The glenoid components' backs can be flat, convex, or curved; irrespective of shape, biomechanical research in cadaveric glenoids has revealed that curved backing is more resistant to micromotion and has superior loosening properties than flat-backed components [72], [73].

Keeled or pegged components, which can be cemented or un-cemented, are the most frequent options for glenoid fixation in TSAs. The keeled component was initially introduced in 1973, and it has undergone several changes since then [74]. However, it still has a tapered end. The pegged component is newer, and it consists of a changing number of pegs of various lengths [75]. According to literature, superior loosening performance was observed in pegged versus keeled components [73], [76]–[78]. Pegged glenoid components provide more theoretical stability against shear stresses. Pegs in glenoid implants operate separately to prevent shear as long as they are spaced far enough

apart [78]. The effect of fixation peg design on implant stability has been studied using parametric methods. In the study by Williams and Abboud [79], the shear stability of five distinct peg geometries of differing shapes and sizes was examined. Among the considerations were the number of pegs, their size, and their aspect ratio. According to their findings, components with several small pegs distribute stress more uniformly throughout the material and offer superior sheer stability per unit volume when compared to components with larger but fewer pegs [79]. Furthermore, studies have shown that keeled designs are more likely than pegged models to generate higher radiolucency with time [76], [77], [80], [81]. Even though their presence suggests poor cementing, the importance of these radiolucencies has been contested. While research has shown a preference for pegged components because of their perceived decrease in radiolucency over time, there is no strong evidence that they improve clinical results over time [82].

Cemented, cementless, or hybrid procedures can all be used to adequately secure prosthetic glenoid components. Cemented glenoid implants are all-polyethylene components and come in a variety of component design variants. The attachment mechanism, which may be classified into two groups: keeled and pegged glenoid components, is the fundamental difference. Cemented implants rely on a quick-drying bone cement to help them adhere to the bone. Although this method allows prosthetic components to be connected to somewhat porous bones and antibiotic material to be added to the bone cement, the danger of cement debris remains a concern since it can induce inflammation and, as a result, glenoid component loosening [83], [84]. Biologic integration and mechanical interlock are required for uncemented glenoid components, also known as press-fit components [85]. While the initial attachment that encourages bone formation can be accomplished via screw fixation, also known as metal-backed components, or a combination of screws and press-fit pegs, the component's rough or porous surface stimulates natural bone regeneration.

Uncemented glenoid components provide the advantage of a decreased occurrence of radiolucency at the prosthesis-bone interface, as well as the ability to offer possible secure long-term fixation [85]. Nonetheless, excessive polyethylene wear, potential detachment of the polyethylene from the back of the metal, and failure to establish initial

secure attachment can lead to complications [85]–[90]. There are numerous cemented and uncemented options for attaching the glenoid component in TSA, including cemented all polyethylene components with keels or pegs, metal-backed components with screws and hybrid approaches. No fixation method has become the standard, indicating that there is still a need to develop a more lasting design with a longer implant lifetime.

Recently, a novel fixation technique has drawn interest because of its geometry and potential to exhibit less rocking-horse loosening than the standard glenoid onlay methods typically utilized in TSA. Instead of placing the implant on top of the intrinsically volatile surface of the compromised bone, as with the classic onlay approach, inset or inlay fixation entails tapping into the tough arthritic section of the bone to provide a sturdier implant support system [91]. To complement the local morphology and be level with the adjoining cartilage, the inlay design is inserted in the center of the glenoid. A prosthetic inset glenoid may have superior biomechanical properties in terms of mechanical loosening than a traditional onlay glenoid model since it is placed in the natural glenoid enclosed by bone. In a cadaveric study conducted by Gagliano et al., the onlay glenoids experienced considerably higher stresses and displayed substantial loosening during fatigue testing, in contrast to the inlay glenoid components, which did not undergo loosening [92]. Long-term performance may favor inlay glenoid components over onlay glenoid designs, nevertheless additional data is needed to draw this conclusion despite preliminary findings indicating this result [93], [94]. This novel approach to prosthetic inset glenoid fixation may represent a quantum leap forward from the standard strategy of glenoid implant fixation on the bone surface.

1.4.2 Walch Classification

A description of the morphology of arthritic glenoids was first presented by Walch et al. in 1999 [95]. In the context of shoulder replacement, it is by far the most frequent categorization used to classify glenoids. The original classification was based on axial computed tomography scans of the shoulder with slices that were 5 mm thick, which resulted in inconsistent findings for both inter- and intra-observer agreement [95]. It has since been modified with a revised classification approach based on 3D-CT

reconstructions, which currently include categories B3, C2, and D [96], [97]. The Walch classification, shown in Figure 1.9, offers advantages such as the stratification of shoulder arthroplasty outcomes for distinct pathologic glenoid types and, during preoperative planning, the detection of morphological features that may present surgical complications. A summary of the current Walch glenoid types can be found in Table 1.3. A standardized language simplifies data evaluation and comparisons across studies, thereby accurately and consistently defining glenoid types has substantial clinical and research ramifications.

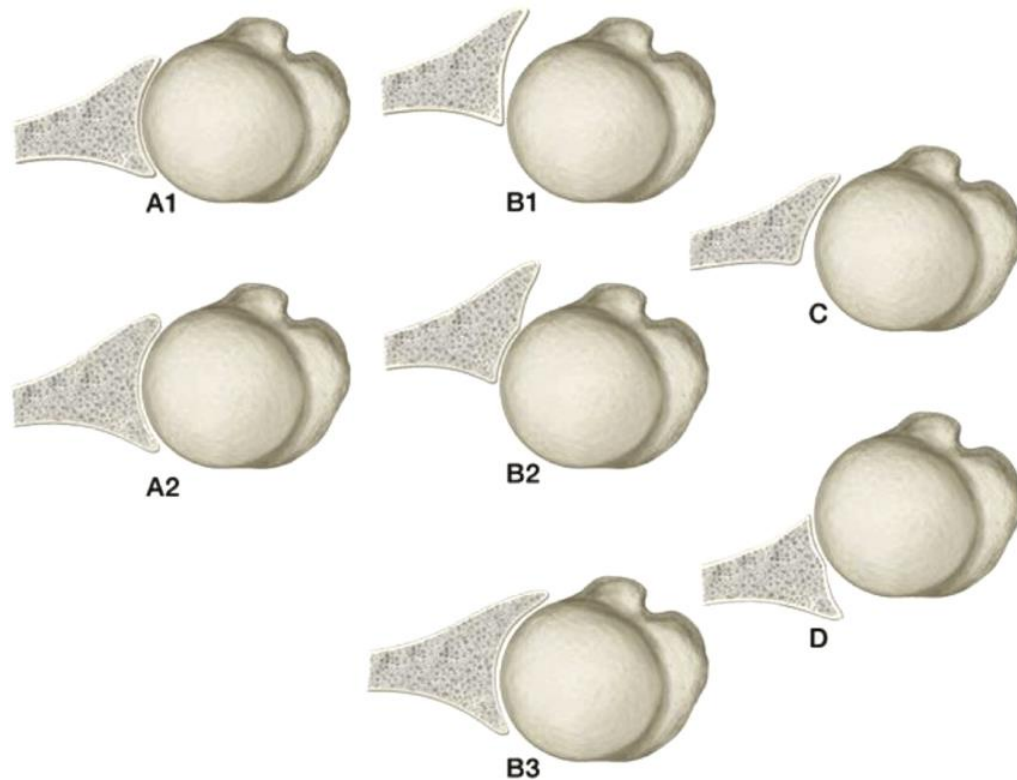


Figure 1.9: Walch Glenoid Morphology Classification [35].

In this classification, type C does not include subcategories. An agreement on the distinction between type C1 and C2 is still ambiguous.

Table 1.3: Walch Glenoid Morphological Classification [95]–[98].

<i>Category</i>	<i>Description</i>	<i>Subcategory</i>
<i>Type A</i>	Symmetrical or centralized humeral head without posterior subluxation, focal deterioration	A1: Minimal central deterioration or erosion A2: Extreme or significant central deterioration or erosion
<i>Type B</i>	Asymmetrical or decentralized humeral head with posterior subluxation, asymmetrical deterioration	B1: No overt glenoid erosion, despite posterior joint space constriction, subchondral sclerosis, and osteophytes B2: Biconcave glenoid appearance with visible or evident erosion at the posterior rim B3: Uni-concave articular region, posterior wear, and one or both of $>15^\circ$ retroversion or $>70\%$ posterior subluxation of the humeral head.
<i>Type C</i>		C1: Increasing retroversion of more than 25° with the development of posterior glenoid dysplasia C2: Glenoid biconcavity and acquired posterior bone loss
<i>Type D</i>	Characterized by $< 40^\circ$ anterior humeral head subluxation, whether present or absent, in the anteverted glenoid	

1.5 The Rocking Horse Phenomenon

The process through which glenoid prostheses become loose over time is frequently attributed to edge loading, sometimes referred to as the rocking horse effect. Repetitive eccentric loading of the humeral head on the glenoid component's surface is believed to be the cause of this phenomenon (Figure 1.10).

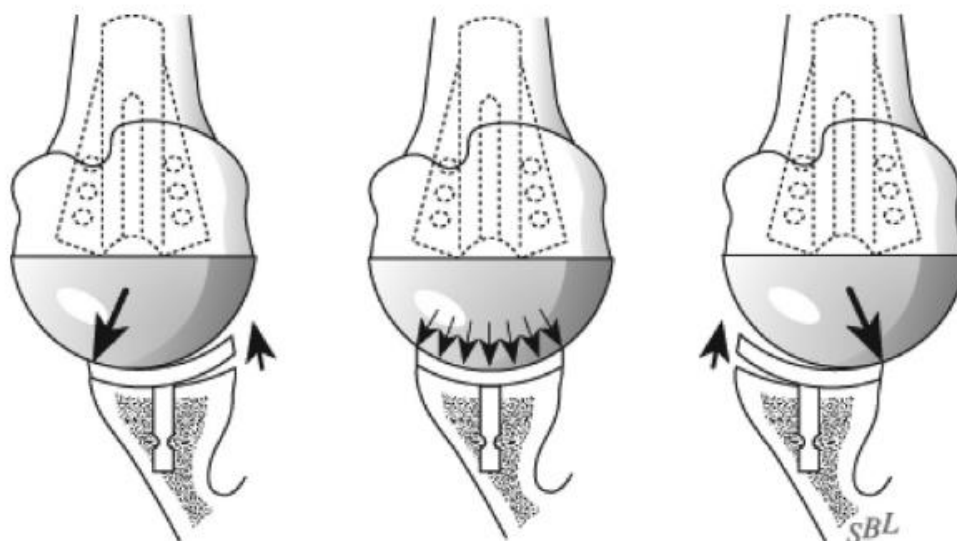


Figure 1.10: Illustration Demonstrating the Rocking Horse Phenomenon [99].

Edge loading is happening as the humeral head translates from one side to the other, which results in compression on the compressed side and extension at the contralateral side of the component.

During edge loading, one side of the glenoid is under compression while the other side is under tension. The torque created on the fixation surface causes tensile stress at the bone-component contact, which ultimately leads to failure.

The incidence of glenoid loosening varies greatly, ranging from 0% to 96 %, based on the notion that radiolucency is a marker of acute loosening [61], [63], [64], [100]–[103].

Prosthetic loosening is primarily impacted by time, according to literature, with radiolucency, component loosening, and revision procedures occurring at rates of 7.3 %, 1.2 %, and 0.8 % per year, respectively [104]. The rocking horse phenomenon can occur in any direction due to the glenohumeral joint's mobility, which allows the humeral head

to rotate and translate. However, due to rotator cuff weakening or tears, SI edge loading is the most frequent [105], [106]. Furthermore, wear posteriorly and anteriorly, as well as inferior migration have been linked to glenoid loosening. These have been observed to occasionally result in a pronounced tilting of the component [65], [105], [107]–[109].

According to literature, producing a small radial mismatch in the glenoid and humeral head radius of curvature minimizes the incidence of glenoid loosening [71], [110]–[117]. A smaller radial mismatch is favored as it can result in a more prominent contact area between the glenoid component and the head of the humerus, and diminished contact loads. Consequently, this can result in an overall decrease in stress that occurs at the interface between component and bone. In addition, designs with smaller radial mismatches are expected to provide better stability to the joint and decrease the translation of the head of the humerus during motion. Even though a smaller radial mismatch provides such benefits, it also increases the stress at the rim, which can result in component loosening. The risk of component loosening increases when the center of the humeral head moves away from the center of the component, intensifying bone-cement contact stresses [117].

1.5.1 Standard Test Methods for Dynamic Evaluation of Glenoid Loosening or Disassociation

ASTM F2028

Due to the growing interest in glenoid component loosening, the American Society for Testing and Materials (ASTM) developed the ASTM F2028 standard for evaluating implant failure based on the rocking horse phenomenon. The standard entails measuring the change in implant rim displacement over time in relation to the number of load cycles as a result of loosening. This standard involves the integration of glenoid components into a bone replacement prior to testing, unless cadaveric samples are used, with densities varying between 20-30 lbs/ft³ to approximate the typical strength of glenoid cancellous bone [118]. If bone cement is utilized in the preparation, it is critical to allow for curation in order to minimize the production of air bubbles, which can cause weak points. During

cycle testing, the component is immersed in water or another fluid test medium, and hydraulic or mechanical load frames are utilized to perform the cyclic protocol. Constant high-impact loading on the glenohumeral joint is typically minimal, however routine daily activities can place many times the body weight over this joint. It is advised to utilize an axial load between 200 and 750N, depending on the glenoid shape, since this might produce resultant loads ranging between 300 and 1000N; these load values would be similar to carrying or lifting 0.5 to 8 kg objects [118]. Higher loading rates can be utilized for strength testing, although they are unlikely to be representative of regular everyday activity. The compressive force is applied to the component perpendicular to the glenoid plane through the humeral head, which is subsequently translated parallel to the glenoid plane along the component's superoinferior (SI) or anteroposterior (AP) axes. The recommended number of cycles for the protocol is roughly 100,000 at a frequency of 1-2 Hz; nonetheless, activities that cause significant shoulder stress occur significantly less frequently than this estimate. For ten years, this number of cycles might reflect around 25 higher-load daily activities [118]. The test is also displacement constrained, with a distance of 90% of the SI and inferoposterior (IP) subluxation movement to simulate anatomic glenoid and humeral head contact. One of the method's limitations is that it has yet to be established if an increase in edge displacement correlates to an initial stage or development of loosening. As a result, it merely serves as an oblique indicator of fixation failure.

Anglin et al. [112] composed a laboratory experiment that replicated the rocking horse mechanism; it has since been sanctioned as the ASTM standard mode for assessing glenoid implant loosening. The technique accounts for the horizontal motion at the superior and inferior edges of the glenoid implant as an indicator of inception and propagation of fixation failure. Nonetheless, this method does not give direct or thorough data on fixation failure, highlighting the underlying problem with such investigations in that the fixation site is implanted inside the bone and not readily visible. Anglin et al. aimed to develop a research assessment approach centered on glenoid loosening and apply it to a variety of prosthesis designs [112]. To simulate the rocking horse effect, they used a biaxial mechanical assembly to provide SI edge stress to the component as it was cyclically loaded. This study was the first to define a physiologic standard for measuring

glenoid loosening while simulating typical edge loading forces. The authors determined that the most accurate sign of glenoid loosening was the assessment of tensile distraction in the SI rim of the glenoid. They also determined that nonconforming components with curved backs and roughened fixation exteriors had the least degree of distraction; they were deemed to have the least potential for loosening [112].

1.6 Rationale

By 2050, the number of initial and recurrent shoulder arthroplasties is predicted to rise by 322 %, demanding a thorough understanding of the glenohumeral joint biomechanical characteristics and glenoid implant loosening metrics to maximize long-term results [69].

Even though various research studies on total shoulder arthroplasty have been conducted to determine the most effective component design, no conclusive findings have been obtained. Performing a shoulder replacement surgery was originally intended to relieve discomfort after non-surgical options had been exhausted. With advancements in materials, design, and medical treatments, the objective expanded to include not only minimizing pain but also repairing shoulder function and enhancing range of motion in the joint. Glenoid loosening is the most prevalent known complication following TSA procedures, accounting for 20% to 60% of all unsuccessful total shoulder arthroplasties [119]. The loosening of the glenoid is thought to be a complex failure mode that is influenced by both patient and surgeon factors.

The current standard, ASTM F2028-17, uses a bench-top simulated rocking horse experimental technique to determine component loosening tendency. Performance metrics outlined within the current standard only consider displacement measurements taken at discrete positions. The rocking horse effect has been successfully reproduced in several investigations based on the ASTM F2028 procedure. However, no apparent solution has been proposed as the gold standard for glenoid loosening prevention. Even though design and fixation improvements have been made, research is still being performed to address this issue, indicating that a greater understanding of the mechanics behind the rocking horse phenomena is required.

A six-degree-of-freedom (6-DOF) Stewart platform was previously utilized to perform biomechanical testing on shoulder implants in the surgical mechatronics lab located at St. Joseph's Hospital's Hand and Upper Limb Clinic (HULC). Six prismatic actuators were placed in pairs on the base plate of the Stewart platform at three different positions. This arrangement provides six degrees of motion and assures that the actuators only undergo linear loads, allowing for significant load production. The intended purpose of this previous research was to explore a combination of digital volume correlation, micro-computed tomography imagery, and mechanical loading induced through a radiolucent Stewart platform. However, in addition to only being able to perform low cycle counts, the mechanical test findings incidentally also revealed spikes in force reactions during the cyclic loading test. These observations might indicate a possible influence of the component shape on the reaction forces observed. Since a high cycle count is required for compliance with the ASTM F2028-17 standard, a novel apparatus was designed for high cycle count performance and ASTM compliance.

The current body of work will demonstrate the creation of a unique experimental approach to improve the performance of cyclic load testing on glenoid implants. This dissertation first describes the evaluation and comparison of the performance and applicability of the innovative apparatus to the previously created Stewart Platform. After assessing the feasibility of the cyclic loading frame, the study will conclude with an examination of the distinctions between common glenoid types. Eventually, the apparatus developed is intended to be a component of a workflow to examine glenoid fixation, which will use DVC techniques to record deformation before and after the cyclic loading procedure. The creation and testing of the equipment will be the exclusive subject of this dissertation.

1.7 Objectives and Hypothesis

As part of this dissertation, three major objectives were investigated. These objectives focused on two main prospects: validation of the innovative cyclic loading device for glenoid component testing and exploration of a connection between component shape

and reaction forces in light of the stated observations from the previous study utilizing the Stewart platform. Each objective is followed by the associated hypothesis.

Objective 1: To explore the relationship between component geometry and reaction loads during cyclic loading protocol.

Hypothesis 1: It was hypothesized that geometries with drastic variations in surface height would result in higher reaction forces being observed. Based on literature and recognizing that the anatomy of the glenoid fossa changes around its circumference, higher stresses are expected to occur at the edges of the glenoid component. It was hypothesized that similar behavior would occur as the load applicator traveled from regions of lower depth to areas of less depth when using the selected test samples.

Objective 2: To design and test an experimental device capable of performing the ASTM F2028-compliant cyclic load testing process.

Hypothesis 2: It was hypothesized that the experimental technique would be capable of reproducing the rocking horse phenomena while conforming to the guidelines specified in the ASTM F2028. To be considered compliant, the apparatus must include a means for mounting and enclosing the test specimen, aligning, and positioning the glenoid component as well as the humeral head component, a motion and force control system, and a lubrication system.

Objective 3: To quantify and analyze the compressive reaction forces on keeled and pegged glenoid components using the developed testing apparatus.

Hypothesis 3: It was hypothesized that no statistically significant differences in load responses would be obtained by performing cyclic loading tests using pegged and keeled glenoid components. Although several findings have documented better loosening performance in pegged versus keeled designs, there is still no standard component attachment [73]. In addition, the findings to date indicate that neither component differs from the other in terms of functional outcomes.

1.8 Thesis Overview

In order to better understand the underlying mechanics of glenoid loosening, Chapter 2 presents an experimental testing technique for measuring reaction forces in three separate components while enduring cyclic loading conducted by a Stewart Platform. Chapter 3 expands on Chapter 2 by outlining the design and implementation of cyclic loading experimental equipment capable of achieving high cycle counts. The novel testing equipment is used to recreate the experiments that were conducted in the previous chapter. Chapter 3 also compares the two testing methods' performance and analyses each one's ability to capture data on component reaction forces under cyclically loaded conditions. Chapter 4 describes the improvement to the testing apparatus described in Chapter 3 for compliance with the ASTM F2028 standard. In Chapter 4, a force reaction test method using the improved ASTM-compliant test apparatus is presented, comparing four different groups of specimens. Chapter 5 contains a general overview and summary of the research, as well as concluding remarks and recommendations for future work.

Chapter 2

2 Development of Reaction Force Test protocol using a 6-DOF loading apparatus

OVERVIEW: This chapter describes the execution of a cyclic loading test procedure utilizing a 6-DOF Stewart Platform. This protocol's design comprises the Stewart Platform, a load cell, the software required to manage the mechanism, and the design of the various specimens to be evaluated. The main purpose of this chapter is to assess the load response as a function of component shape. The experimental measurement of the stresses occurring in the specimens contributes to a better understanding of the major TSA failure mechanism, edge loading.

2.1 Introduction

Due to their great rigidity, accuracy, and force potential, parallel robots are readily applicable to biomechanical testing [120]. The Stewart-Gough platform, commonly known as the hexapod robot, was initially shown in 1965 as a flight simulator mechanism; however, changes to the mechanism enabled this parallel manipulator system to perform biomechanical testing with 6-DOF controlled motion and position [121]. The hexapod robot is substantially stronger than industrial serial robots, has a higher load-bearing capacity, costs less for equal capability, and is smaller in size [122]. As a result, for biomechanical assessments requiring significant load-carrying capability, rapid dynamic agility, and accurate position control, a Stewart platform system may be favorable to an industrial serial robot. The hexapod robot has been used in several studies to assess spine components [123], [124]. Nonetheless, these early models had myriad challenges that required major upgrades at the mechanical and system control levels to achieve better performance for 6-DOF biomechanical testing.

Prior research at the surgical mechatronics lab in the Hand and Upper Limb Clinic, which led to the current thesis, entailed the building of a testing machine based on the design of a generic 6-DOF parallel or hexapod robot (Figure 2.1).

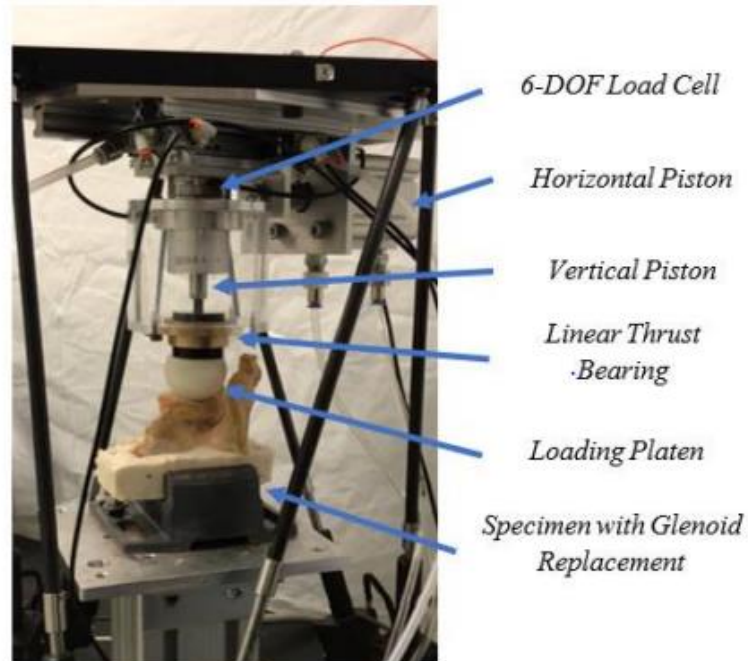


Figure 2.1: The Stewart Platform developed at the HULC lab. Critical components are labeled.

In this configuration, a base and top plate are connected by servomotors with each motor pivoting through ball-socket joints, providing linear operation of each leg. Due to its translations and rotations, the hexapod configuration has the ability to transform linear displacements into 6-DOF motions. The kinematics of the original loading test can be preserved while the motion route is replicated using position-controlled approaches. The hexapod robot design was chosen because it has a number of desirable features. These features include a higher power density, which translates to low mass and high strength, as well as high stiffness, a vast range of motion, and a simple kinematic structure with a lower center of gravity than alternative configurations, all of which make them safer. Hexapods are structurally strong due to their triangular trusses. In addition to the robot's force sensing capabilities, a calibrated six-degree-of-freedom load cell (Mini 45, ATI Industrial Automation, NC, USA) was incorporated into the hexapod's loading platform. Load cells are calibrated, commercially available instruments that measure loads and torques using internal strain gauges. A 6-DOF load cell measures forces and moments along three perpendicular axes. This enabled the measurement of loads applied to the component while the robot employed those forces at different sections of the component.

The goal of this previous study was to use the ASTM F2028-17 standard in conjunction with micro-Computed Tomography (micro-CT) imaging to replicate physiological joint stresses at the shoulder utilizing a 6-DOF loading mechanism. The study aimed at quantifying experimental stresses at the bone-cement contact. The amount of movement in a region of interest is measured using digital volume correlation, which compares two picture frames recorded before and after the movement and calculates a ratio of change. Using this approach, it was possible to properly detect motion produced by glenoid loosening while executing high-impact rotations. Although it was not of relevance to the research, peaks in reaction forces were detected during the test. Most notably, during the cyclic loading procedure with the previous prototype, a change in compressive force was observed; however, the compressive force should remain constant in order to successfully apply the glenoid loosening testing standard. In addition, the testing protocol was not capable of performing high cycle counts as outlined by the ASTM F2028-17 standard. These observations, which prompted the current body of work, were not addressed in that study. Thus, the initial phase of this study entailed running a series of experiments to evaluate the previous setup's performance. Pneumatic-driven displacements and software-controlled displacement forces were applied to the end-effector during the experiment, and the force responses at the specimens were recorded.

2.2 Materials and Methods

2.2.1 Data Acquisition

The hexapod robot features servomotors that operate in an open-loop control system to provide continuous data. All data collected by the load cell was sent into a USB-6211 data acquisition device (National Instruments Corporation, Austin, Texas), which was then gathered and processed using NI LabView software. Forces were measured in the X, Y, and Z directions, as well as torques. The in Figure 2.2 describes the load cell's axis.

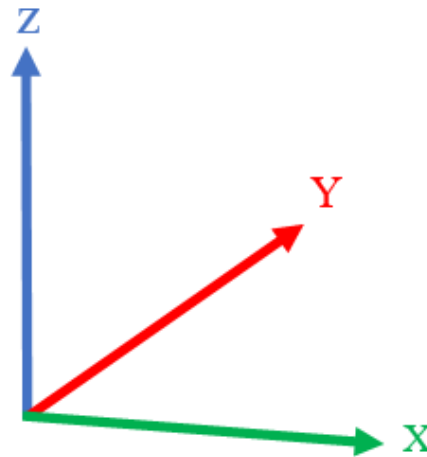


Figure 2.2: Load Cell Axis Indicating the Positive Axis Directions.

Z - direction: Parallel to the vertical piston; X - direction: Normal to the component's face; Y - direction: Orthogonal to both Z and X.

2.2.2 Specimen Design

Three distinct designs of components were developed using SolidWorks (Dassault Systèmes SOLIDWORKS Corp., Massachusetts, USA) and then fabricated using an SLA 3D printer (FormLabs, Somerville, Massachusetts), to examine the causes of the change in compressive force during cyclic loading observed in previous research. The premise of the described approach is that disparities in compressive force are caused by the shape of the glenoid component's rim; consequently, testing different component shapes should reveal a greater insight into this theory. The test designs were based on the geometry of a rectangle, a triangle, and a concave shape.

Rectangular Design

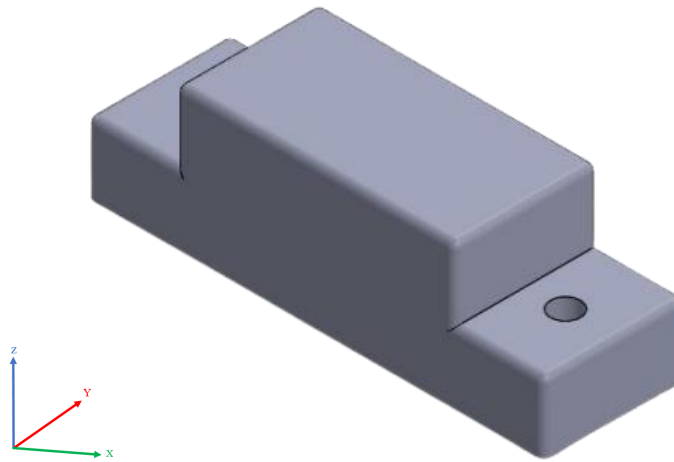


Figure 2.3: Design of the Rectangular Design Test Component.

The least amount of variation in reaction forces was predicted for the rectangular component. Additional lateral support and threaded holes were added to the test components to guarantee part fixation during testing.

The rectangular design was selected due to the uniformity of its surface (Figure 2.3). It was estimated that this part would demonstrate the most consistent results of recorded forces in the X, Y, and Z directions since its shape does not feature fluctuations in height along its surface. It was critical to create a neutral baseline for comparison across the three designs in order to determine how much a change in design might affect the peaks in compressive force observed.

Triangular Design

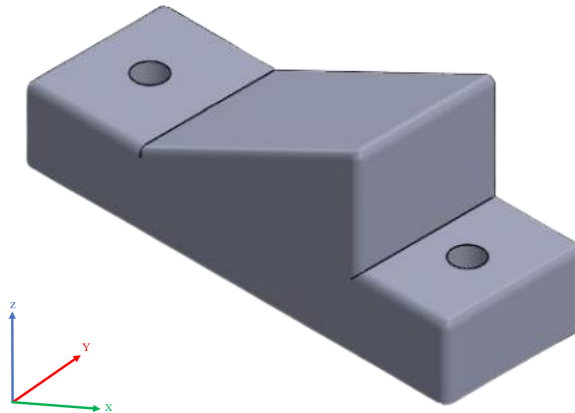


Figure 2.4: Design of the Triangular Design Test Component.

The highest amount of variation in reaction forces was predicted for the rectangular component. Additional lateral support and threaded holes were added to the test components to guarantee part fixation during testing.

The triangular shape was chosen since the slope between the bottom and top parts is quite severe (Figure 2.4). This large variation in surface height was desired because it was assumed that the high compressive force values in the glenoid component were caused by the rim being located at a higher point than the glenoid's face center. Because this design has a severe fluctuation in height throughout its surface, it was anticipated that this component would register the highest results of collected forces in the X, Y, and Z directions.

Concave Design

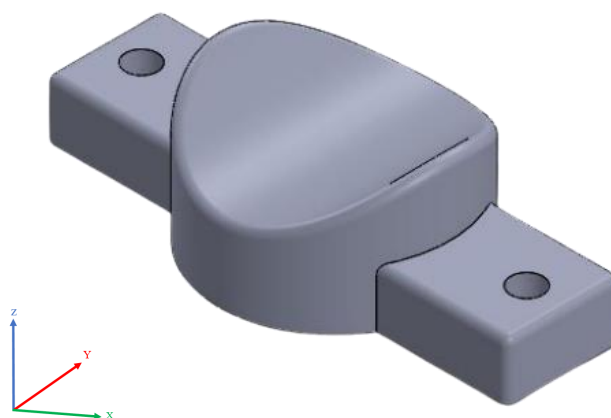


Figure 2.5: Design of the Concave Test Part.

The concave element was predicted to have a comparable level of variation in response forces as other glenoid components that had been evaluated previously. Additional lateral support and threaded holes were added to the test components to guarantee part fixation during testing.

The design shown in Figure 2.5 was created to resemble a commercial glenoid component curvature and offer a middle ground between the lower reaction force values expected in the rectangular component and the higher values expected in the triangular part. It was predicted that this element would produce outcomes comparable to those achieved while testing a typical glenoid implant component, albeit that they would be less severe than the triangular design's test results.

In contrast to earlier setups, in which the specimen to be examined was clamped to the apparatus' base, the three 3D-printed pieces were screwed into an extra element that was affixed to the device's base (Figure 2.6). The purpose of this setup was to reduce the chances of components breaking at the clamp-part connection.

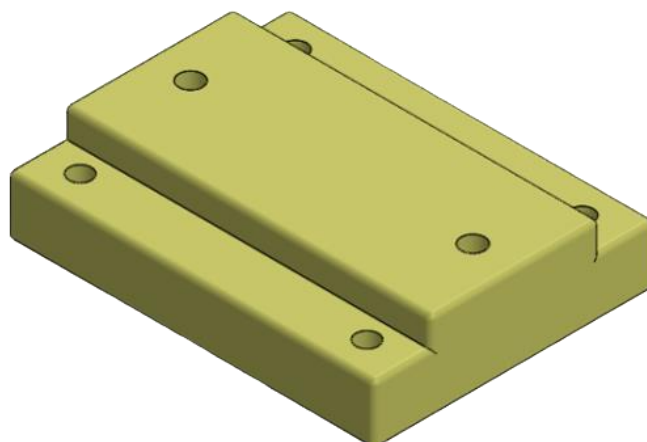


Figure 2.6: Design of the Attachment Base Component.

The four holes in the lower half of this design are meant to be screwed into the apparatus's base, while the two holes in the top are meant to secure each of the three designs to be assessed.

2.2.3 Experimental Protocol

The setup for this experimental test consisted of fastening the components to the apparatus' base, directly beneath the piston, and then using LabView to apply the required load to the test part and record the results. The experimental protocol was performed separately for each specimen as follows: after attaching the 3D-printed component to the hexapod's base, the 3D-printed design component was screwed to the face of the base component. Given the hexapod's legs have a restricted range of extension and contraction, it was critical that the components had the adequate height to make contact with the loading platen during the loading procedure. Three separate loads were applied to the components once they were attached to the device. Each sample was loaded at 300, 500, and 700N, resulting in three separate data sets for each component. A 6-axis load cell (mini-45, ATI Industrial Automation, Apex, NC, USA) instrumented within the hexapod was used to measure the loads. Each load was applied to the specimens for only five minutes since, in comparison to genuine glenoid implant components, the 3D-printed components were constructed of brittle material with a high risk of fracture occurring at the surface of the objects.

2.3 Results and Discussion

2.3.1 6-DOF Loading Protocol

Following the completion of the three tests for each sample, the values of the forces in the X, Y, and Z directions were collected and analyzed using NI LabView software. In Table 2.1, load responses were averaged and reported.

Table 2.1: Average Loads – Stewart Platform.

<i>Design</i>	<i>Average Load (300N)</i>	<i>Average Load (500N)</i>	<i>Average Load (700N)</i>
<i>Rectangular</i>	$F_X = 9.176\text{N}$	$F_X = 3.936\text{N}$	$F_X = 15.106\text{N}$
	$F_Y = 1.685\text{N}$	$F_Y = 5.018\text{N}$	$F_Y = 6.396\text{N}$
	$F_Z = -269.146\text{N}$	$F_Z = -108.234\text{N}$	$F_Z = -623.885\text{N}$
<i>Triangular</i>	$F_X = 3.154\text{N}$	$F_X = 8.969\text{N}$	$F_X = 5.105\text{N}$
	$F_Y = -4.946\text{N}$	$F_Y = 4.230\text{N}$	$F_Y = -0.696\text{N}$
	$F_Z = -166.758\text{N}$	$F_Z = -369.869\text{N}$	$F_Z = -517.017\text{N}$
<i>Concave</i>	$F_X = 28.382\text{N}$	$F_X = 34.095\text{N}$	$F_X = 43.894\text{N}$
	$F_Y = -48.468\text{N}$	$F_Y = -56.607\text{N}$	$F_Y = -69.205\text{N}$
	$F_Z = -239.580\text{N}$	$F_Z = -323.29\text{N}$	$F_Z = -534.48\text{N}$

((-) Denotes the negative position in the Z axis)

According to the examination of the sample data, under the tested conditions, the reaction forces contradict the previous hypothesis given in Section 2.2 of this thesis. It was initially assumed that the triangular design element would have the highest values of reaction forces in the X and Y directions during testing due to its substantial geometric slope. Nonetheless, the concave design showed the greatest F_X and F_Y variability, contradicting that idea. Prior to testing, it was anticipated that the rectangular component would have the least amount of reaction forces in the X and Y directions and the most consistent reaction force in the Z direction since the surface of this design is relatively constant. Figures 2.7 through 2.9 show the curve derived from the rectangle shape test results. Despite the slight cycle disturbance at the beginning of curves, the figures demonstrate that this part had a relatively consistent reaction force in the Z direction

throughout the three loading situations. The data reported in Table 2.1 support this observation even further. Note that the highest negative values in the Z direction correspond to the platen reaching the ends of the surface of the component and changing the direction of motion.

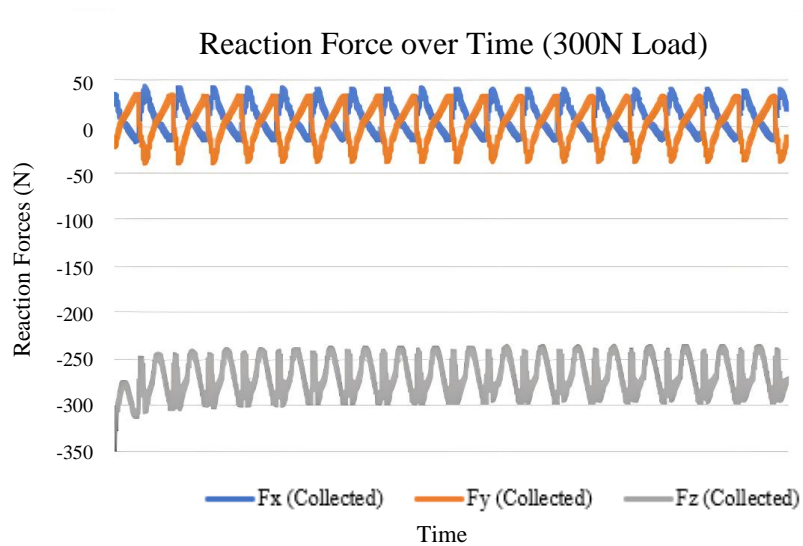


Figure 2.7: Rectangular Design Test Results Plot using 300N Applied Load.

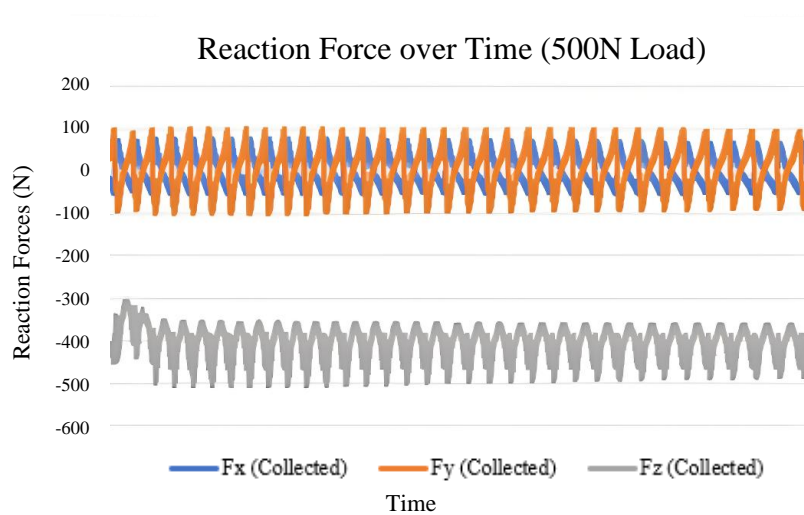


Figure 2.8: Rectangular Design Test Results Plot using 500N Applied Load.

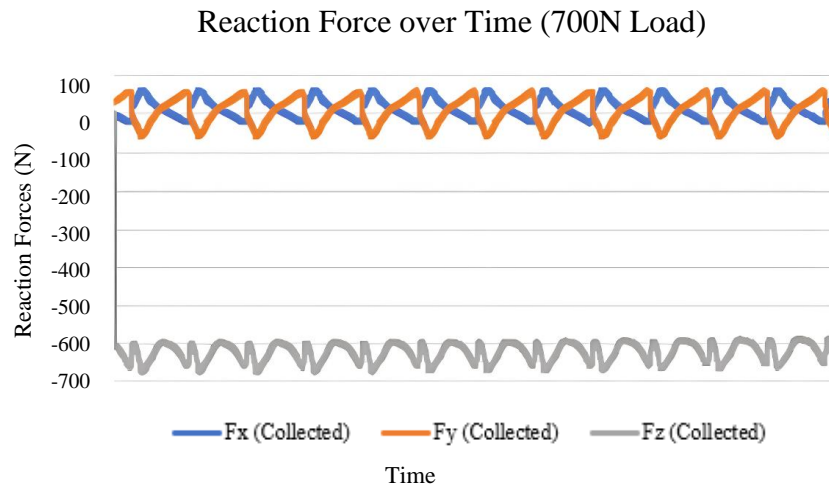


Figure 2.9: Rectangular Design Test Results Plot using 700N Applied Load.

Even though the triangular component had lower reaction forces in some instances (as indicated in Table 2.1), the rectangle design had the least amount of overall reaction forces across all trials. This assertion is valid since it was observed that during the triangular design test protocol, the contact between the load applicator and the surface of the part was not continuous. There were instances when the platen was not in direct contact with the part and was floating in mid-air rather than sliding across the component's surface. These factors account for the low F_X and F_Y values seen in Figures 2.10 to 2.12, which contradict the expectation that this component would have the greatest F_X and F_Y values throughout all studies due to the friction generated by its steep slope. In addition, the curves for this part present significant cycle disturbances, which is likely the results of the irregular contact between the platen and the surface of the part.

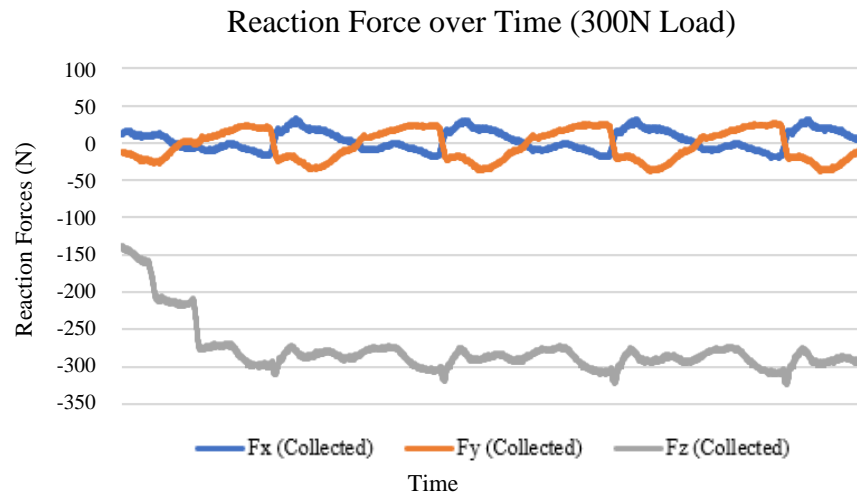


Figure 2.10: Triangular Design Test Results Plot using 300N Applied Load.

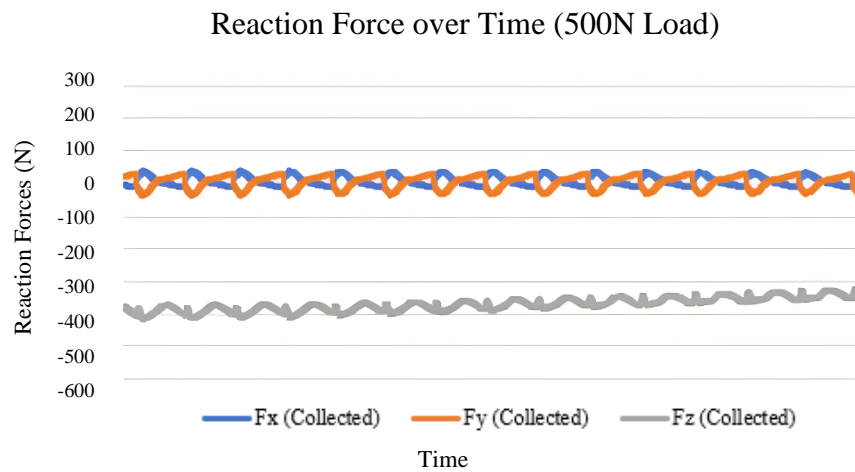


Figure 2.11: Triangular Design Test Results Plot using 500N Applied Load.

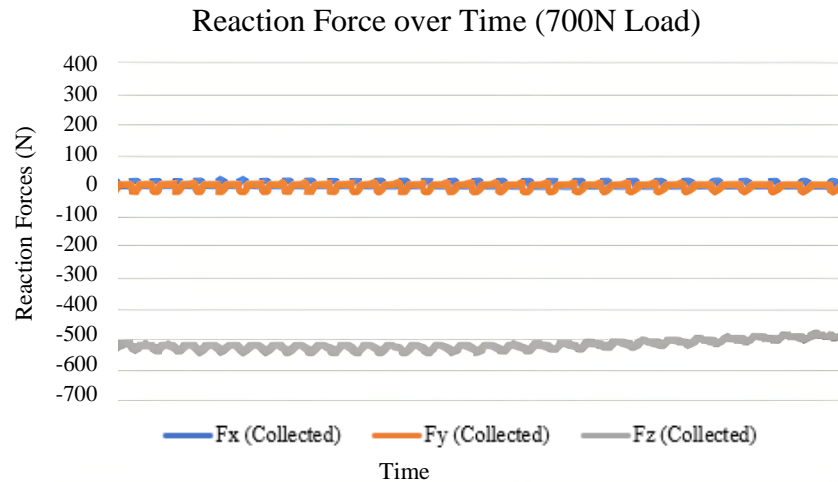


Figure 2.12: Triangular Design Test Results Plot using 700N Applied Load.

Furthermore, the triangle design testing results indicate that this component not only recorded the lowest F_z values, but also those that were farthest away from the applied loads. Inconsistencies in the contact between the load applicator's surface and the component's surface are once again at fault. When the platen dislocated in mid-air rather than sliding through the inclined surface, the load cell was unable to detect any stresses since no forces were applied directly to the component. The period of contact between the load applicator and the component's surface was insufficient for the load cell to collect the entire load applied to the part. Furthermore, while the reaction forces in the X and Y directions are minimal for this design, such values are also the result of inconsistent contact between the load applicator and component faces.

Table 2.1 shows that the testing protocol utilizing the concave component generated the highest F_x and F_y values. This shape was designed to resemble a glenoid implant and offer additional information about the reaction force inconsistencies seen in prior experiments. Several times throughout the testing procedure, the load applicator became trapped at the component's external sections, causing the entire structure to shift as the loaded applicator traveled across the part's face. Further, there were instances when the load applicator was not in direct contact with the part's surface, most notably the component's central area. The absence of contact between the load applicator's surfaces and the component under test is again caused by the applicator's mid-air translation. The

hexapod's extension and contraction limitations are presumed to be the source of this occurrence. Figures 2.13 through 2.15 exhibit considerable reaction forces in the X and Y directions, which are presumably the consequence of the load applicator becoming locked at specific regions and thereby moving the entire item.

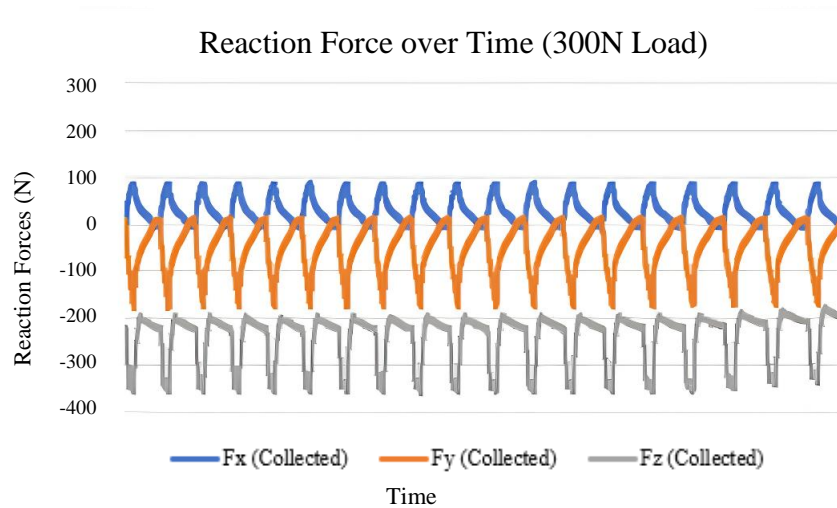


Figure 2.13: Concave Design Test Results Plot using 300N Applied Load.

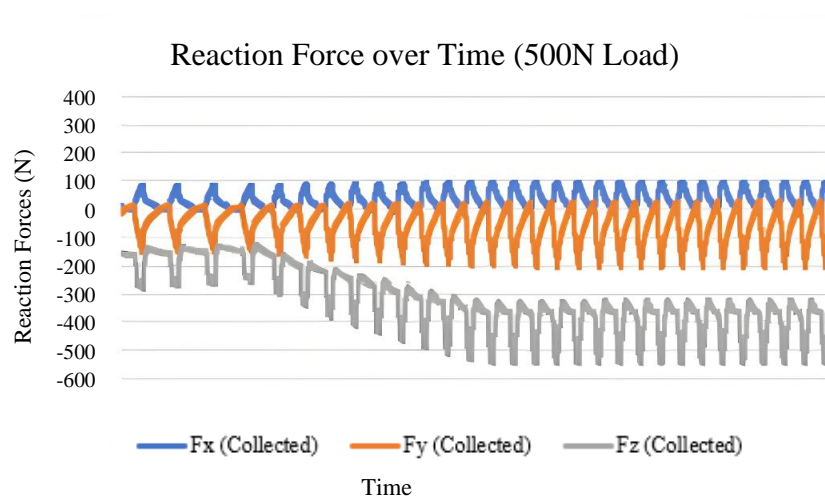


Figure 2.14: Concave Design Test Results Plot using 500N Applied Load.

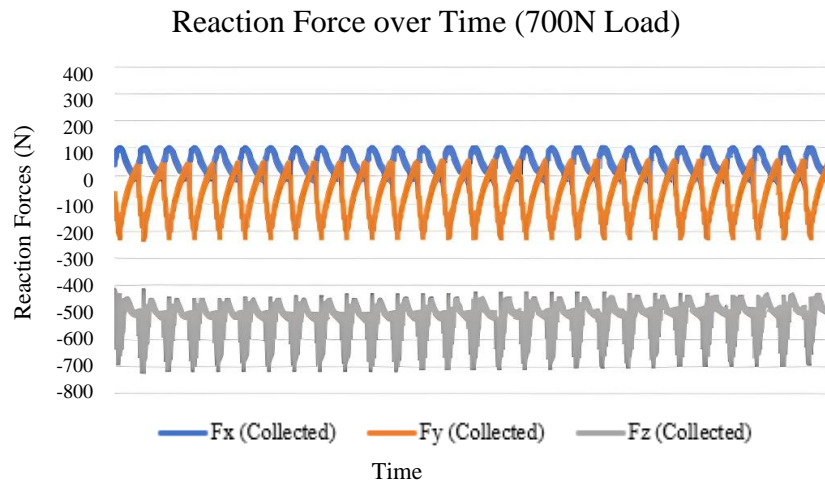


Figure 2.15: Concave Design Test Results Plot using 700N Applied Load.

Furthermore, the considerable difference between the applied and recorded loads in the Z direction is also attributable to the inconsistent contact between the part's surface and the platen. Overall, the results from all loading experiments revealed a variety of reaction force ranges in the X, Y, and Z directions. During the testing protocol, it was observed that excessive friction was being recorded for various components, particularly the concave and triangular components, as the load applicator would get snagged at certain locations on the surface of the items. The large reaction forces observed in the X and Y directions are presumed to result from this friction. Another note is that during all tests, when the platen applied the load and moved across the face of the component, the entire structure, including the testing part and the base, shifted as well. Although the specimen's material may have influenced this aspect, the occurrence of this incident demonstrates that a better testing setup is required to conduct the cyclic loading tests. Furthermore, it was not possible to employ a lubricant as required by ASTM F2028-17 in this setup, emphasizing the need to improve the testing process. Finally, it was revealed that the load applicator lacked adequate extension and contraction controls to travel through certain areas on the surface of the components where there was a height difference. The load applicator traveled in mid-air rather than on the surface of the components as a result of this situation. In an ideal scenario, the vertical piston would adjust to variations in height to maintain contact between the platen and the component's surfaces.

2.4 Chapter Summary

This chapter described an experimental testing approach for measuring reaction forces in various components while performing cyclic loading using a hexapod robot. This system utilizes a load cell in conjunction with NI LabView to measure the load applied to the testing components. While glenoid component loosening following TSA procedures is still a concern, the fundamental processes that contribute to fixation failure at the bone-component interface are largely unresolved.

Considering that reaction forces directly affect the rocking horse phenomenon, which leads to glenoid loosening, the purpose of this chapter was to investigate how these forces vary based on the geometry of the component. This was accomplished by conducting cyclic loading tests on three distinct designs with the hexapod robot to evaluate both the performance of the apparatus under restricted loading conditions and the force reactions that occurred in the components. The designs were subjected to loads of 300, 500, and 750N, as recommended by the ASTM F2028 standard. According to the literature, an axial load between 200 to 750N should be used depending on the glenoid shape, since this might generate resultant loads ranging from 300 to 1000N. Based on this guideline, it was predicted that in this testing technique, loads greater than those used would be observed [6]. It was predicted, in particular, that substantial forces in the Z direction would be detected primarily for components with a significant surface variation. Nevertheless, the results revealed that the apparatus was ineffective in imparting a full load to the component's surface, resulting in loads that differed from the applied forces. Furthermore, due to friction and inadequate testing circumstances, the majority of the components showed unexpectedly high reaction forces in the X and Y directions.

The aforementioned observations reinforce that an upgrade in the design of the testing device is necessary to adequately execute cyclic loading tests as per the ASTM F2028. The experimental equipment was appropriate for detecting variations in reaction forces during a cyclic loading protocol, indicating that the high force reactions found in prior tested components were, in fact, shape dependent. Nevertheless, since the interaction between the load applicator and the surface of some specimens was not

continuous due to extension and contraction constraints, it is uncertain whether the high values obtained are essentially caused by friction that originated from the load applicator's transition from mid-air translation to contact with the part. The current study's research lays the groundwork for the future development of more efficient testing methodologies to address stresses that arise on components during cyclic load testing. The next phase in this analysis involved the redesign of the testing apparatus and protocol in an attempt to improve outcomes while repeating the previously stated experiments.

Chapter 3

3 Preliminary Development of a Cyclic Loading Simulator for Stress Analysis

OVERVIEW: The purpose of this chapter is to discuss the design and implementation of a pneumatic cyclic loading simulation system. This apparatus consists of a rig capable of performing high cycle counts for glenoid component testing. A pneumatic system, a load cell, a vertical load applicator, and the software necessary to operate the device are included in the model. This chapter examines the reaction force response as a function of component shape and correlates the findings to those in Chapter 2. The comparison of the two experimental test methods provides a foundation for performing cyclic loading testing on glenoid components per the ASTM F2028-17.

3.1 Introduction

The previous chapter investigated the analysis of reaction forces on components under a cyclic loading protocol using a hexapod robot. In this approach, loads were applied to the specimens while software controlled the movement of the load applicator as well as the contraction and extension of the robot's legs. Although this configuration was successful in providing further information on the quantification of the resultant forces in the components, the extent to which component shape variation influences these forces remained unclear. A novel configuration was created to address the aforementioned concerns and enhance the effectiveness of the cyclic loading testing protocol as per the ASTM F2028 standard.

3.2 Experimental Setup

3.2.1 Cyclic Loading Simulating System

The new design was devised with the intention of obtaining improved outcomes while redoing the prior testing protocol. To consider this configuration an improvement, it was required to ensure that the load applicator remained in continuous contact with the surface of the components while conducting the cyclic motion. The load cell, horizontal piston, vertical piston, linear thrust bearing, and loading platen were among the components of the prior testing apparatus that were revised (Figure 3.1).

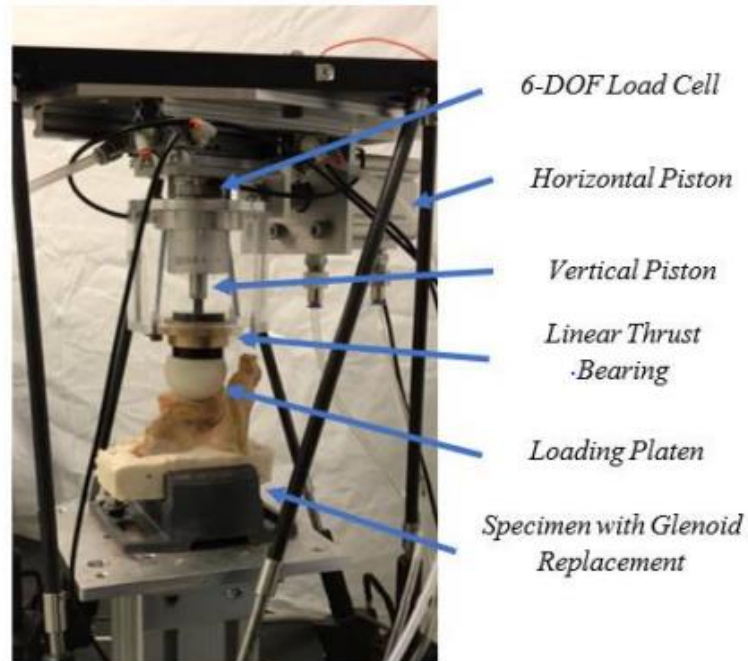


Figure 3.1: Custom-made Hexapod configuration described in Chapter 2.

The linear thrust bearing from the old configuration, which was originally designed to provide stability to the loading platen, was replaced with an improved linear bearing in the new arrangement to potentially reduce the friction forces reported in the previous protocol. The load cell was positioned beneath the specimen clamping element in the new apparatus to reduce the number of attachment points for the carriage assembly (Figure 3.2). Furthermore, bending of the vertical piston was detected in the preceding arrangement. In an attempt to circumvent this occurrence, the vertical piston arrangement was improved, and a more compact actuator housing was fabricated.

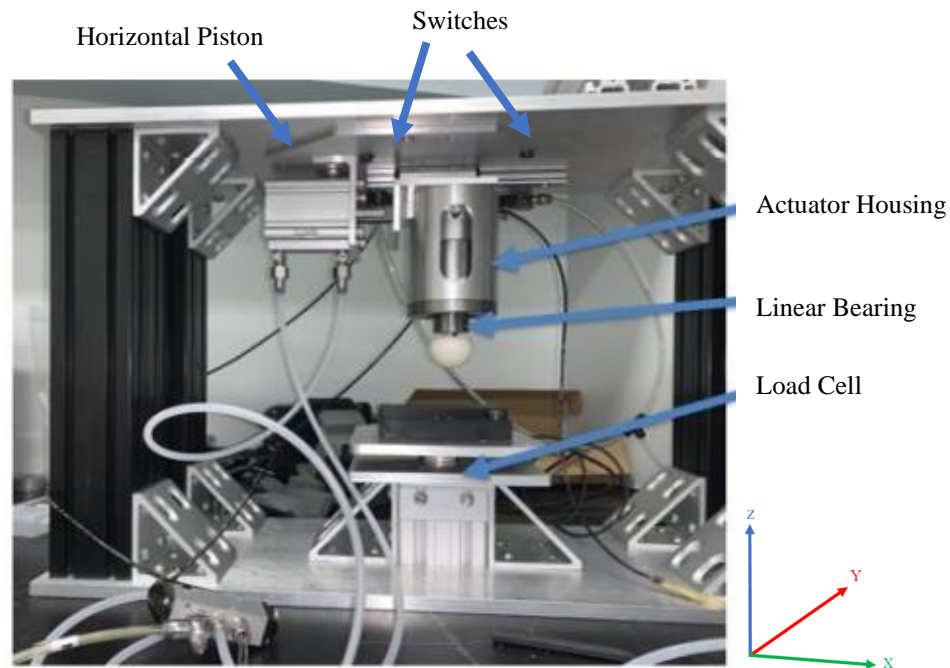


Figure 3.2: Custom-made Cyclic Loading Test Apparatus Configuration. Critical components are labeled.

These modifications were made to reduce friction between the loading platen and the components' surfaces, ensure continuous contact between surfaces, and possibly prevent the entire testing structure from migrating during the cyclic motion. The testing frame is composed of four extruded aluminum profiles located between the bottom and top vise plates of the apparatus. This system is pneumatic, with the horizontal movement controlled by an air cylinder and the vertical load controlled by the NI LabView software coupled to a power supply and the USB-6211 data acquisition device (National Instruments Corporation, Austin, Texas). Switches on the rail attached to the horizontal piston regulate its alternating movement, guaranteeing appropriate cyclic protocol execution. In terms of overall proportions, the new model is equivalent to the previous proof-of-concept design. However, the new design is more suitable for high cycle counts.

Moreover, the components exhibited deformation from compression and cyclic motion following the previous experiments. The incidence with which these deformations occur is affected by the fragility of the material used to create the items. For this set of examinations, new components were 3D-printed with the same material to provide a

more accurate comparison with the previous testing conditions. Future testing processes will employ more durable materials to fabricate the components if 3D-printed components are used.

3.2.2 Experimental Protocol

As with the prior apparatus, the components were fastened to the device's base, and then NI LabView software was used to apply the appropriate load to the sample and record the findings. The new configuration, on the other hand, necessitates manually positioning the vertical piston in the starting position before conducting each experiment. The starting position refers to the piston's closest proximity to the crankshaft. Once the components were attached to the apparatus, three different loads were applied to them. Each sample was loaded at 300, 500, and 700N, yielding three datasets for each component. The forces were measured using a 6-axis load cell (mini-45, ATI Industrial Automation, Apex, NC, USA), which was instrumented beneath the testing base in this design. Since, unlike actual glenoid implant components, the 3D-printed components were made of fragile material with significant surface fracture risk, each trial lasted no more than 5 minutes. The components were identical to the prior arrangement, and it was determined that they had sufficient height to make contact with the loading platen during the loading operation. To validate the design improvement, continuous contact was crucial in this examination.

3.3 Results and Discussion

The values of the forces in the X, Y, and Z directions were collected and evaluated using NI LabView software after the three tests for each sample were completed. The load responses were averaged and given in Table 3.1.

Table 3.1: Average loads – Cyclic Loading Device.

<i>Design</i>	<i>Average Load (300N)</i>	<i>Average Load (500N)</i>	<i>Average Load (700N)</i>
<i>Rectangular</i>	$F_X = -5.371\text{N}$	$F_X = -7.820\text{N}$	$F_X = -14.638\text{N}$
	$F_Y = -9.745\text{N}$	$F_Y = -7.5563\text{N}$	$F_Y = -14.0368\text{N}$
	$F_Z = -289.759\text{N}$	$F_Z = -426.422\text{N}$	$F_Z = -684.453\text{N}$
<i>Triangular</i>	$F_X = 27.471\text{N}$	$F_X = 47.705\text{N}$	$F_X = 55.539\text{N}$
	$F_Y = 44.490\text{N}$	$F_Y = 53.815\text{N}$	$F_Y = 57.629\text{N}$
	$F_Z = -239.673\text{N}$	$F_Z = -406.012\text{N}$	$F_Z = -631.214\text{N}$
<i>Concave</i>	$F_X = 53.259\text{N}$	$F_X = 62.866\text{N}$	$F_X = 53.112\text{N}$
	$F_Y = 53.548\text{N}$	$F_Y = -59.366\text{N}$	$F_Y = 54.361\text{N}$
	$F_Z = -273.010\text{N}$	$F_Z = -483.29\text{N}$	$F_Z = -686.939\text{N}$

((-) Denotes the negative position in the Z axis)

Prior to the protocol, it was assumed that the rectangular design would have the lowest F_X and F_Y values, as well as the most consistent response force in the Z direction since the shape of this component does not vary significantly. This idea was confirmed since the new testing approach indicated remarkably stable F_Z values across all loading tests. Furthermore, the rectangular design tests yielded reaction force results that were very similar to the specified loads, supporting the protocol's efficiency. The findings of the experiment utilizing the new model were consistent with those obtained using the former design described in Chapter 2, as shown in Figures 3.3 through 3.5.

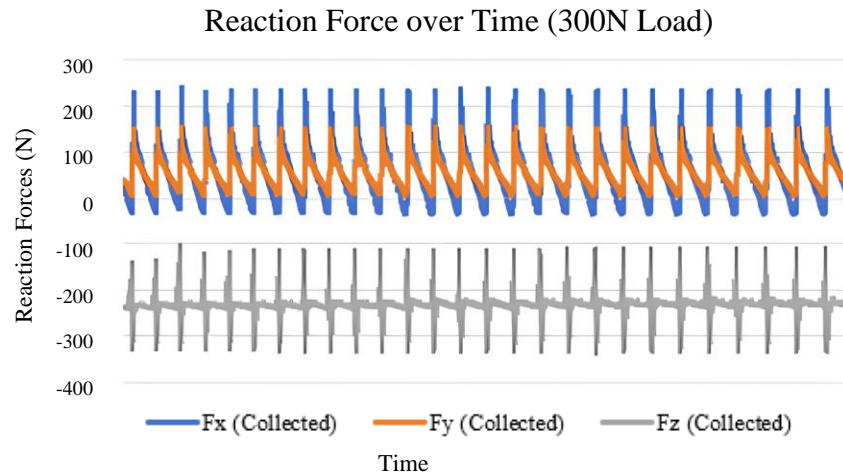


Figure 3.3: Rectangular Design Test Results Plot using 300N Applied Load.

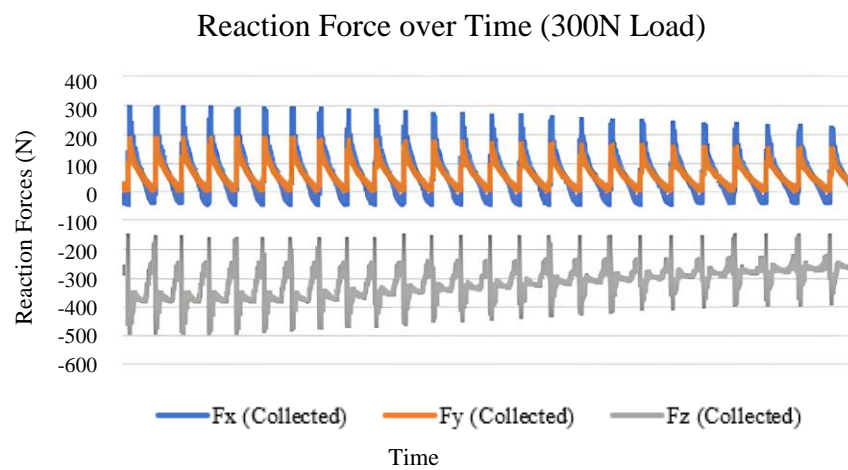


Figure 3.4: Rectangular Design Test Results Plot using 500N Applied Load.

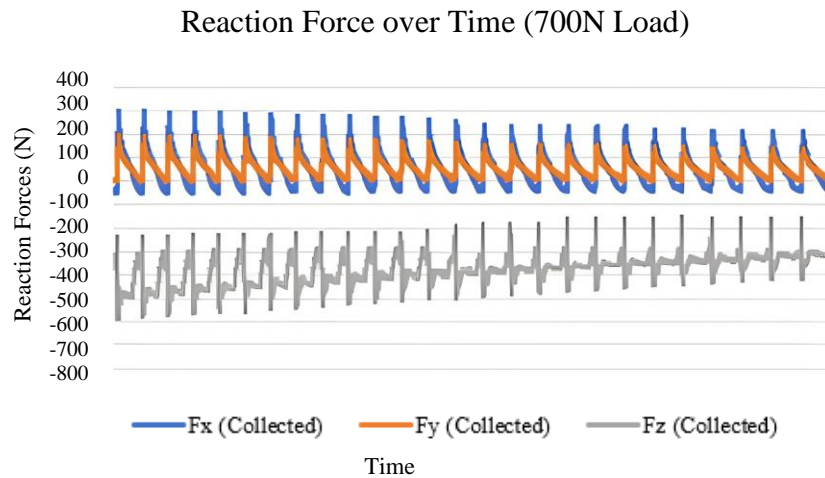


Figure 3.5: Rectangular Design Test Results Plot using 700N Applied Load.

Not only did the results demonstrate a minor reduction of reaction forces in the X and Y directions compared to the prior model, but the magnitudes of these forces were also similar. Furthermore, compared to the prior protocol using the rectangular design, the registered F_z values were not significantly closer to the load delivered to the system. However, the values were more constant and did not fluctuate considerably during the trial. A better translation of the platen on the component's surface was observed. Additionally, no bending or component displacement was detected throughout the experiment. Finally, there was less deformation on the rectangular component's surface once the tests were completed.

The triangular design produced the least amount of reaction forces in the X and Y directions in the previous testing configuration. During the performance of the tests utilizing this component, it was found that the contact between the platen and the components' surface was not continuous. There were occasions when the platen traveled in mid-air rather than on the part's surface. The low reaction forces obtained in the X and Y directions resulted from those circumstances, which conflict with the notion that this design would have the largest reaction forces in all directions due to its surface height variability. Although the improved testing circumstances demonstrated longer contact between the surfaces, the load applicator was still occasionally traveling in mid-air during

the experiments using the triangle design. Even though the load applicator was able to travel across the majority of the surface of the triangle component, it was unable to reach its lowest regions. This is not a constraint of the machine because typical glenoid components do not have such extreme variations in their height surfaces. The triangular design was intended solely to simulate a severe circumstance and investigate its effects on reaction forces. If desired, the loading applicator's extension could be expanded in future designs; nonetheless, it is not required for glenoid cyclic loading testing. Furthermore, as shown in Table 3.1, the average results of the experiments using the triangular design revealed that, as with the previous design, this component reported the values furthest from the applied loads. Inconsistencies in the contact between the platen's surface and the component's surface are responsible for this condition once again. It can be seen in Figures 3.6 through 3.8 that the reaction forces for the tests utilizing the triangular design have increased significantly.

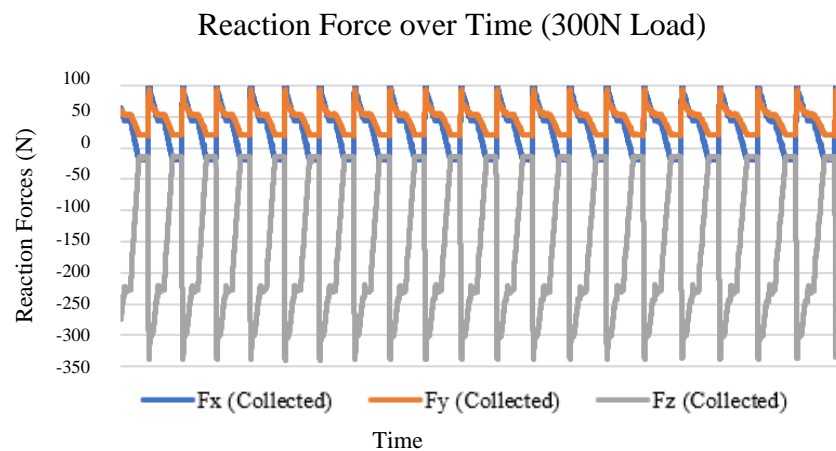


Figure 3.6: Triangular Design Test Results Plot using 300N Applied Load.

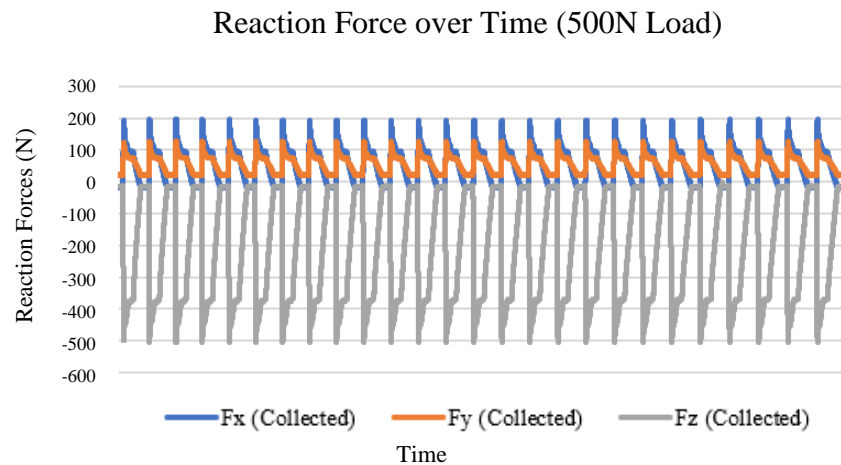


Figure 3.7: Triangular Design Test Results Plot using 500N Applied Load.

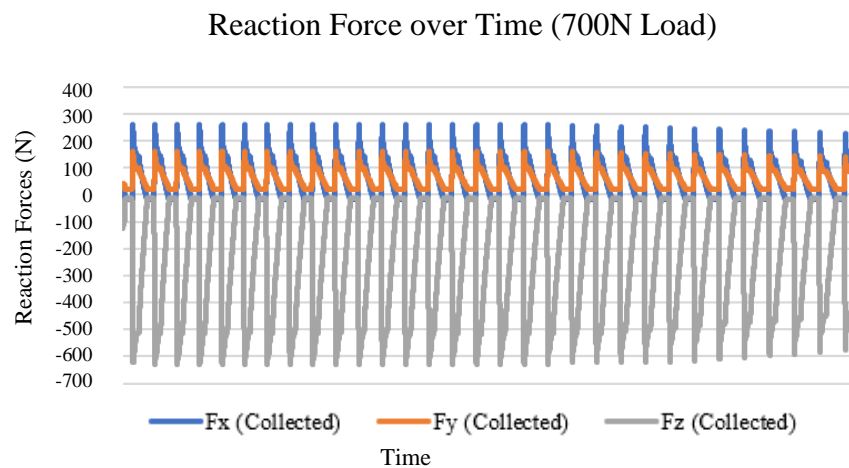


Figure 3.8: Triangular Design Test Results Plot using 700N Applied Load.

While the larger F_z values are attributable to the prolonged contact between the component's surfaces and the load applicator, the increased forces in the X and Y directions are due to the rapid change in motion once the horizontal piston reaches its position farthest from or closest to the crankshaft. Finally, while testing the triangular design with the new configuration, no bending or component movement was detected.

In the previous experimental conditions, the concave design testing results revealed the greatest deviations in F_x and F_y , contrary to the anticipation that the triangular design would yield such results. This design was created to simulate a regular glenoid implant to

offer further insight into the previously reported disparity in reaction forces. The load applicator would become snagged at the outside regions of the component in the hexapod robot experiment, and the entire structure would shift as the platen traveled across the surface of the component. With the modified arrangement, the platen would no longer get locked at specific points during the cyclic experiment. Additionally, as the platen traveled across the surface of the component, the overall movement of the structure was reduced. The remaining minor structure movement was due to the component not being securely fastened enough at the base to withstand the loads and movement of the load applicator. Improving the mechanism that connects the component to the device's base can alleviate this condition. A stiffer material should be used instead of a component composed of the same material as the testing element. Furthermore, there were occasions in the previous testing settings where the load applicator was not in constant contact with the surface of the component, most notably in the middle section. The modified design resulted in improved and consistent contact as seen by the reaction forces curves shown in Figures 3.9 through 3.11.

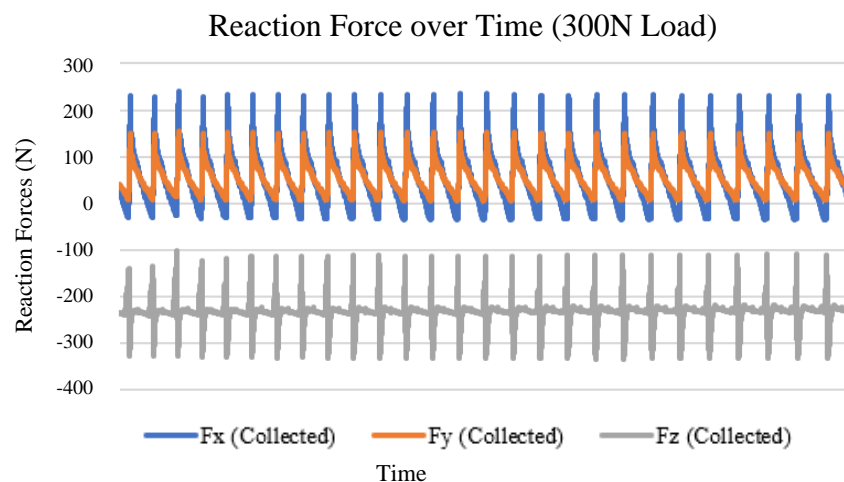


Figure 3.9: Concave Design Test Results Plot using 300N Applied Load.

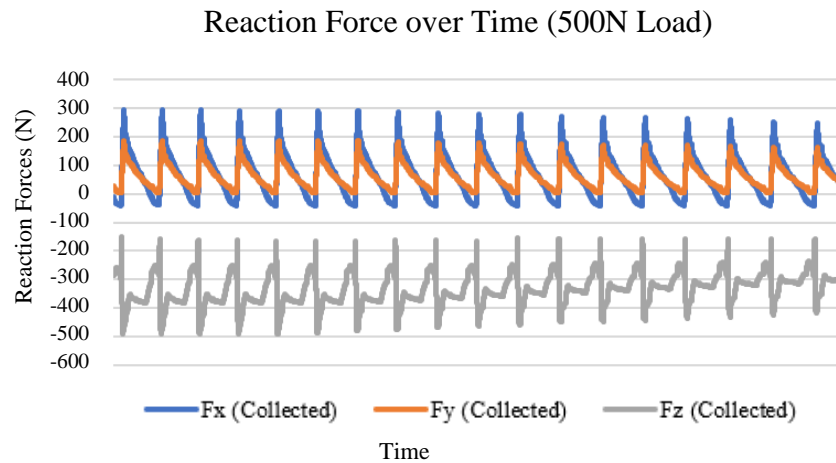


Figure 3.10: Concave Design Test Results Plot using 500N Applied Load.

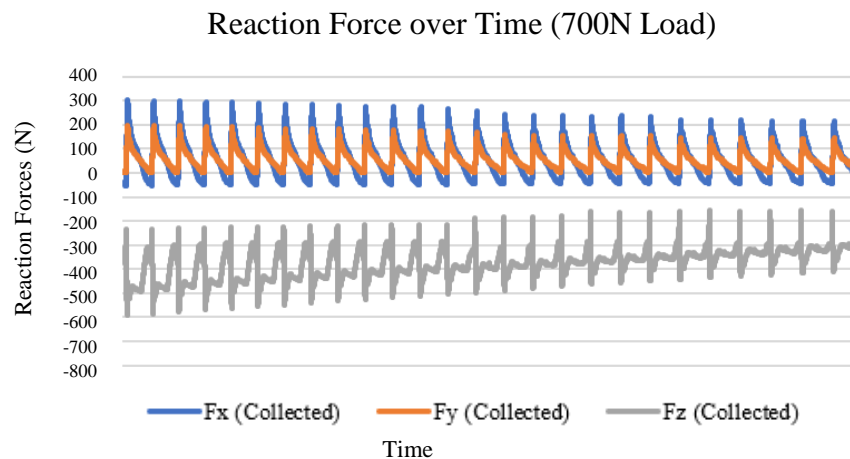


Figure 3.11: Concave Design Test Results Plot using 700N Applied Load.

While the contact time was prolonged, there was also increased friction since no fluid was administered, despite the ASTM standard's recommendation. Similar to the previous testing procedure, the new experimental protocol was designed primarily to explore the reaction forces on the specimen while it was cyclically loaded; subsequent design iterations will satisfy the ASTM F2028 standard. Furthermore, an increase in response forces in the X and Y directions was found. Once again, this is a consequence of the excessive forces generated by the platen's shift in motion when the horizontal piston reaches the locations closest to and furthest away from the crankshaft. Finally, no vertical

piston bending was recorded during the concave design cyclic loading experiment utilizing the modified testing arrangement.

Tables 1-5 in Appendix B indicate the percent errors, as well as the highest and lowest reaction forces values, obtained when the components were subjected to 300, 500, and 700N loads utilizing both testing devices. When employing the hexapod apparatus, large percent errors were detected, with values ranging from 10.285 % to 78.353 %. This further suggests that the apparatus required revisions to successfully conduct the protocol. When the modified configuration was used, there was a significant improvement in percent error, with values ranging from 1.866 % to 20.109 %. It's worth noting that the 20.109 % score was recorded for the triangle, which, as previously stated, exhibited various concerns with continuous contact. Furthermore, this result indicates a 24.304 % enhancement over the 44.414 % reported when the hexapod robot was used under identical testing conditions. Ultimately, the largest reduction in percent error was 63.637 % for the rectangular model under 500N applied load. The triangular and concave designs reported the highest error percentage reductions of 24.305 % at 300 N and 31.944% at 500N, respectively. These findings support the benefits of the new testing arrangement. All percentage values achieved with the new setup are within reasonable limits and hence deemed acceptable under the testing conditions. In addition, the results in Table 3.1 show that when the new testing model was used instead of the previous setup, the intended values were obtained more frequently. This indicates that, with very few adjustments, the new model has the potential to successfully perform the ASTM F2028-17 cyclic loading technique.

3.4 Chapter Summary

This chapter addressed the development of a novel testing apparatus based on the experimental testing technique outlined in Chapter 2 for monitoring reaction forces in various cyclically loaded components. The new protocol consists of a testing system that measures the force applied to the implant components using a load cell and NI LabView. This chapter compares the efficacy of two testing instruments in providing insight into the reaction forces that occur on cyclically loaded components. The revised configuration

entailed moving the load cell beneath the testing base to reduce the number of connecting points in the assembly and improve data recording. Additionally, the vertical piston assembly was improved to prevent binding and friction. Lastly, this system is pneumatic, with an air supply controlling horizontal movement and the NI LabView software controlling vertical load through a power supply and the USB-6211 data collecting device (National Instruments Corporation, Austin, Texas). Following the sequence of design revisions, the cyclic loading tests were repeated utilizing the three prior design components. The components were tested to loads of 300, 500, and 750N, as prescribed by the ASTM F2028 standard. A comparison of the findings acquired from testing conducted before and after the equipment's design revisions demonstrated that the cyclic protocol's performance significantly improved.

Previously, utilizing the hexapod robot, which was designed to do cyclic stress testing on a scapula, high values of F_X and F_Y were recorded. The compressive force, F_Z , which was supposed to remain constant, demonstrated a high level of variance in that design. When the tests were repeated after the testing apparatus was revised, the results revealed a more consistent range of F_Z values. In addition, values closer to the actual loads were recorded, with the maximum recorded values exceeding the applied loads, as expected based on the literature. Periphery loading places higher stress on glenoid components than center and transition zone loading, hence loads greater than those applied should be expected on the components' outer areas. The modified configuration resulted in an increase in forces in both the X and Y directions. The increased friction is due to the longer contact between the load applicator's face and the component's surface. Friction was expected due to the materials utilized to build the components and the load applicator's composition. In addition, despite the ASTM F2028 standard's recommendation, no testing fluid was employed in these trials since the protocol was only designed as a preliminary examination of the reaction force component's dependence on component shape. It was also discovered that as the horizontal piston moved from closest to farthest away from the crankshaft, the friction rose as a result of the abrupt shift in the load applicator's motion. It is logical to assume that there will always exist some friction while completing these tests, just as there is friction in the human shoulder joint. The emphasis should be on adjusting the testing techniques such that the friction forces are as low as feasible. The

current study's analysis lays the groundwork for the future development of more efficient testing methodologies for cyclic load testing of glenoid components.

Overall, the testing results were far superior to the old arrangement. The cyclic technique was successfully applied by the new frame since the compressive force, F_z , remained constant throughout the experiment. Additionally, vertical piston binding was drastically reduced, and contact between the load applicator's surfaces and the component under load increased substantially. The discrepancies between the applied load and the reported F_z loads are most likely attributable to the manufacturing material and attachment method utilized to secure the components to the apparatus' base. This testing procedure was effective in establishing a relationship between component shape and the loads that occur in the component during cyclic loading. Further research based on the findings presented can be applied to cyclic testing of glenoid components in order to reduce the rates of glenoid loosening.

Chapter 4

4 Development and Application of a Testing Protocol for Glenoid Cyclic Loading Simulation

OVERVIEW: This chapter highlights the improvements implemented to the testing device that was initially introduced in Chapter 3. The chapter's goal is to assess the equipment's suitability for ASTM standard-compliant testing protocol of glenoid component loosening. Following the design iterations, a force study using four different sets of glenoid specimens was performed to further investigate the reaction loads that develop on the specimens being cyclically loaded. Investigating component loads or stresses can be essential for evaluating the implications of joint loading. By correlating this information to known material characteristics, it is possible to assess the potential for material failure as well as the directions and cyclical pattern of loading.

4.1 Introduction

The incidence of joint problems is expanding as the ageing populations increase, which raises the need of discussing joint replacement. Glenoid loosening remains a prevalent cause of failure despite several attempts to strengthen the fixation of total shoulder arthroplasty glenoid components. The rocking horse phenomenon, according to current consensus, is the main process that leads to glenoid loosening. The humeral head is eccentrically and cyclically loaded on the glenoid, causing this condition. It has been reported that increasing bone-cement reactions loads as the head's center translates further from the glenoid's center might increase the chance of component loosening [126]. When compared to the forces at the knee and hip joints, the forces at the glenohumeral joint are commonly discounted as being negligible [127]. When the shoulder travels, reaction forces at the glenohumeral joint counteract the mass moment of the upper extremity [128]. These forces are inversely correlated with the behavior of the muscles that cross the joint. Reaction forces are a crucial component of shoulder biomechanics since the humeral head's compression into the glenoid maintains the glenohumeral joint stable. To improve the design and fixation of joint implants, as well as optimize TSA outcomes, it is necessary to understand glenohumeral joint contact forces (GHCF). Additionally, this knowledge enables doctors to counsel patients regarding preventing the implant or joint from becoming overloaded.

Several cyclic loading studies were carried out in Chapters 2 and 3 in an effort to investigate the underlying processes and stressors surrounding the issue of glenoid loosening. The investigations were performed utilizing three different component geometries to assess the shape dependence of the load responses. The cyclic loading study in Chapter 2 was conducted using a hexapod robot. The findings showed significant friction and inadequate contact between the load applicator and the specimen surfaces. The outcomes of the cyclic loading protocol were improved by creating a new testing system in Chapter 3. Improved contact and friction between the surfaces of the load applicator and the testing component were obtained when the new machine was used. The findings of the experiments performed with the new equipment contributed to the understanding of the response forces experienced by the components during cyclic

loading. The outcomes demonstrated that load reactions are, in fact, shape-dependent, with larger stress loading being observed as the humeral head moves farther from the component's center. This finding could further aid in glenoid component design modification to prevent loosening. One drawback of the apparatus developed in Chapter 3 was that it did not entirely adhere to the ASTM standard as it did not include a way of introducing a testing medium and a method of counting the protocol's cycles. In accordance with the ASTM F2028-17 standard, the present chapter provides additional development of the testing apparatus. This chapter also examines the reaction forces that exist between four significantly different sets of glenoid components. In addition to having distinct shapes, the distinct model groups also had different component replacement scenarios, which expanded the study's scope and offered variety to the load measurements. The ligaments, muscles, and intra-articular pressure were also excluded from this model's potential analysis. The experiment was designed in this manner for simplicity and to precisely identify the effects of component shape under cyclically loaded motion.

4.2 Materials and Methods

4.2.1 Specimen Selection

The test specimens for this experiment were obtained from a previous investigation of Force-Space Navigation for Surgical Robotics [129]. Sawbones® (Vashon Island, Washington, USA) was used to create two different scapula models. Both models were of a left shoulder with trabecular bone represented by the softer foam core and cortical and subchondral bone represented by the harder outside surface. Normal bone geometry was used in the first model. The second model exhibited Walch B2 type erosion, which is the erosion of the glenoid's posterior edge. In Figure 4.1, the two models are displayed.



Figure 4.1: Models of the Normal (left) and B2 (right) Sawbone Scapulae [129].

There were two primary groups of specimens used for these experiments, each containing 12 samples. The primary distinction between the groups was the glenoid replacement technique. The glenoid replacement approach was carried out by a surgeon in one group and by a surgical robot in the other. The surgeon used the onlay fixation technique while the surgical robot utilized the inlay method. An inlay fixation is where the component is inserted in the center of the glenoid. In this technique, the peripheral bone is preserved creating more support for the component. An onlay fixation, the classic approach, is where the bone is cut and the glenoid sits on top of the bone. This technique does not preserve surrounding bone and the construct is less stiff. The components were installed according to standard clinical practice. The two groups were subdivided into normal models and Walch B2-type models. The surgeon selected the appropriate implants for each of the 3D-created shoulder models in a manner similar to that found in an operating room. A small Wright Medical Aequalis™ Perform™ keeled glenoid implant with a 60-mm diameter was used for the normal shoulder type. A medium Aequalis™ Perform Plus™ pegged glenoid prosthesis with a 25° wedge from Wright Medical was selected for the B2 shoulder version. The 3D-printed versions of the two implant models can be seen in Figure 4.2.

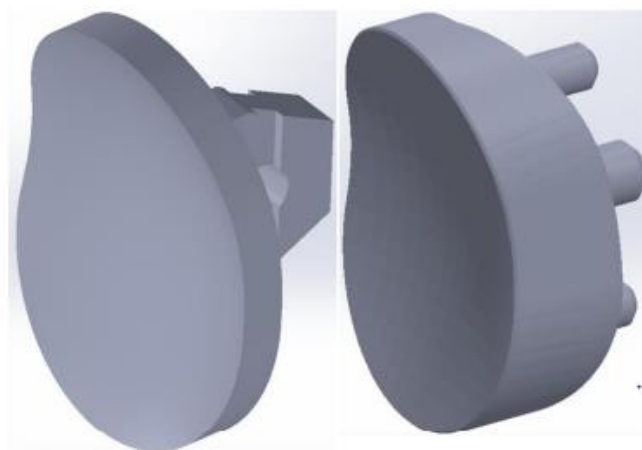


Figure 4.2: Small-Keeled Glenoid Implant (left) and Medium-Pegged Glenoid Implant (right) [129].

The outcomes of this experimental regimen were expected to be unaffected by discrepancies in the glenoid replacement technique. Although their material qualities are not comparable to those of medical-grade glenoid implants, 3D-printed glenoid implants were chosen for this protocol due to their affordability and ease of fabrication. The implant placements for both scapula models are displayed in Figure 4.3.

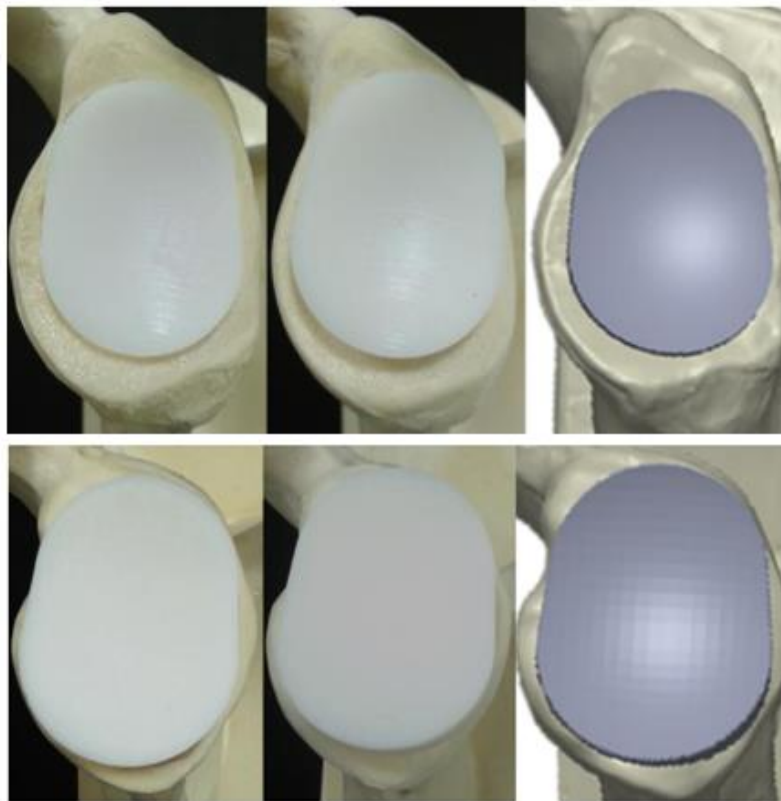


Figure 4.3: Normal Keeled Implant Placement (top) B2 Pegged Implant Placement (bottom) [129].

Inlay placement (left), Onlay placement (center), Pre-op planned placement (right)

4.2.2 Specimen Preparation

In this study, four groups—two sets of inlay components and two sets of onlay components—were assessed. Both the inlay and onlay sets contained six normal type glenoids and six B2-type glenoids. As the specimens were being prepared for testing, the scapula models were sliced to isolate the glenoid component region since it was the area that interested the analysis (Figure 4.4).



Figure 4.4: Isolated B2 (top) and Normal (bottom) Specimens.

Each specimen was sliced at around the same height to preserve consistency. Both the inlay and the onlay groups received this treatment.

The specimens were cemented in place using a mold with suitable measures for compliance with the clamping mechanism and the humeral head to ensure that they remained firmly fastened during testing. Instant Tray Mix Acrylic Resin Powder and Liquid (Lang Dental Manufacturing Company, Wheeling, United States) were combined equally and poured into the mold containing the specimen. In the previous testing configuration, there was no method to confine liquid covering the specimen, making it impossible to introduce a fluid testing medium. This experiment must feature a mechanism that can maintain the contact surfaces submerged in the fluid test medium to comply with the ASTM F2028-17 standard. In an effort to address this challenge, a container was fabricated and cemented around the specimen, enabling water to be applied as the testing medium. This container was precisely sized and manufactured to ensure that there would be enough liquid to completely cover the component while preserving the cyclic motion of the load applicator. The arrangement utilized to cement the specimens is shown in Figure 4.5.

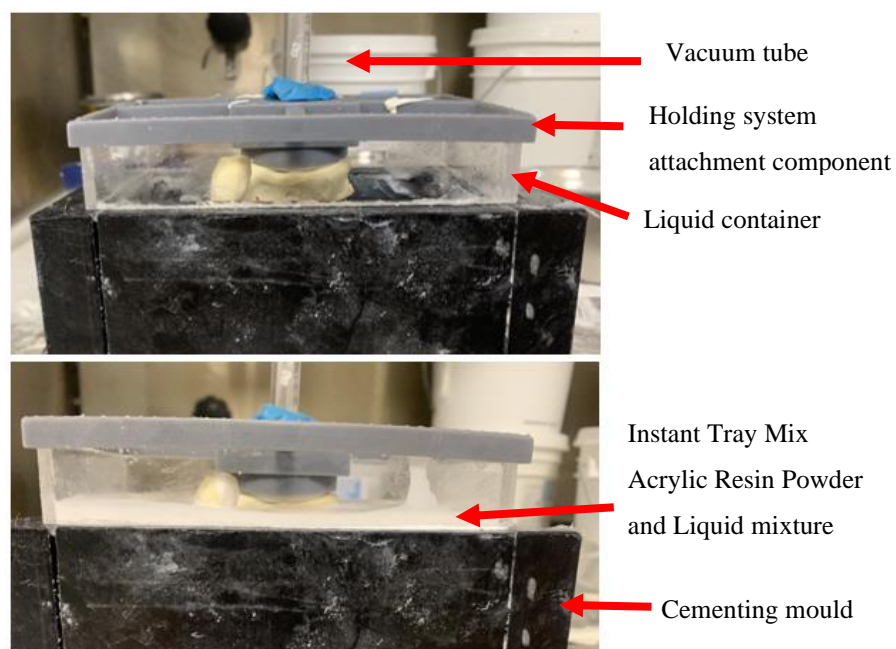


Figure 4.5: Cementing Method including the Liquid Container and Vacuum System.

The framework for the cementing technique is shown before (top) and after cementing the sample (bottom).

A vacuum-based retaining system was developed to ensure that the component would have sufficient height for constant contact with the load applicator. During the curing process of the cementing mixture, this mechanism maintained the specimens suspended in situ. Two unique types of holding attachment parts were 3D printed, one for the small implant and the other for the medium implant. They were created by reverse engineering the 3D-printed glenoid implant components to ensure surface compliance. The crankshaft extension and contraction lengths were taken into consideration throughout the cementing procedure to guarantee that the center of the implant component and the load applicator would coincide mid-cycle. The models created to aid in the cementation of the specimens are shown in Figures 4.6 and 6.7. The specimens were meticulously cemented to minimize the formation of air bubbles as these would represent weak areas.

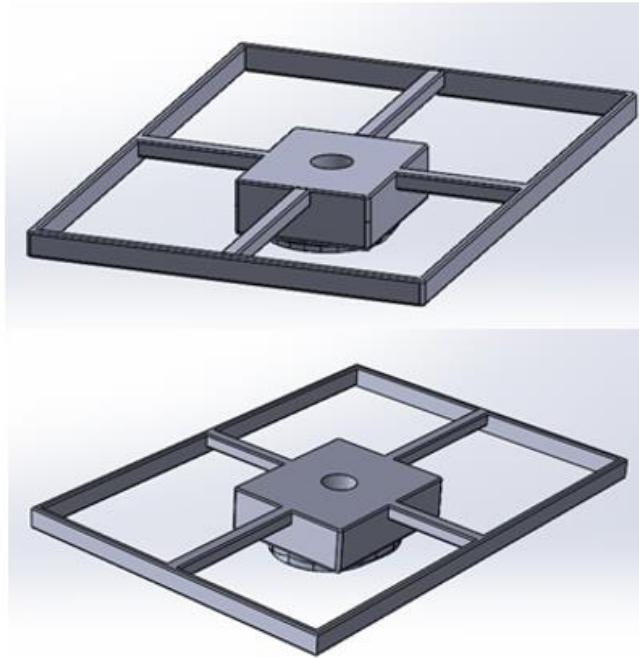


Figure 4.6: Vacuum-based holding System attachment Components.

The exterior measurements of the holding attachment parts are in agreement with those of the liquid container. Both the holding component and the liquid container ensure that the specimens are positioned at the ideal height for constant contact between the components and the load applicator.

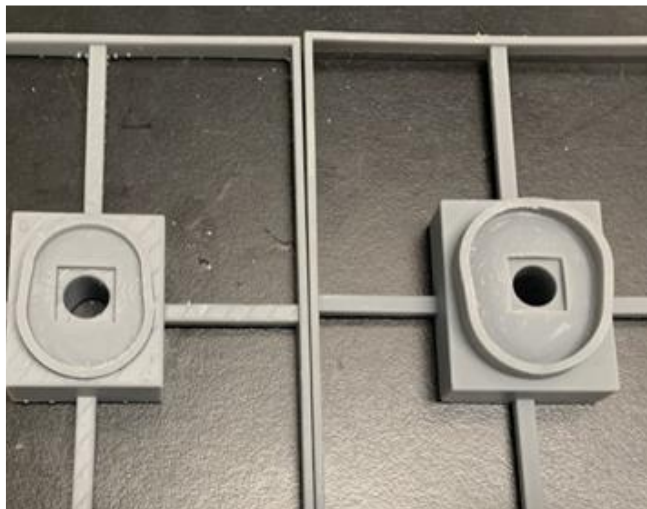


Figure 4.7: Vacuum-based holding System attachment Components for the Small (left) and Medium (right) Specimens.

Splash protection components were also created to prevent potential liquid splashes during testing since these could compromise the testing equipment. To maintain clear visibility during the experiment, these guards were 3D-printed using clear filament (Figure 4.8).

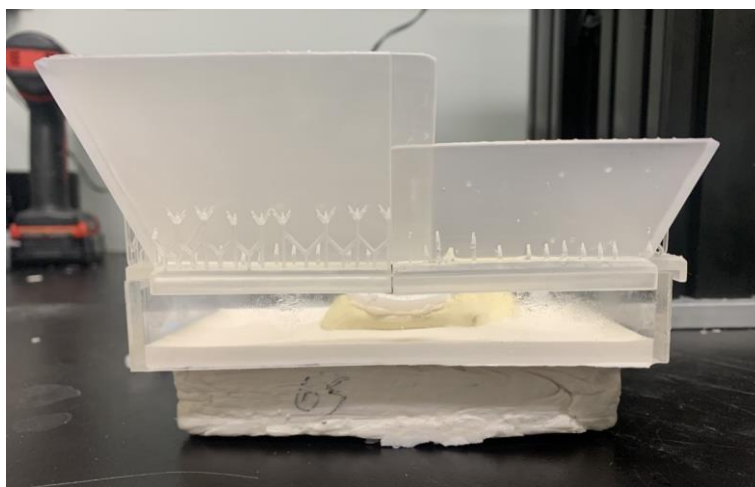


Figure 4.8: Splash Protection Components mounted onto a Test Specimen.

4.2.3 Cyclic Loading Testing Frame

The test frame created in Chapter 3 was capable of replicating the appropriate cyclic motion to simulate the rocking horse phenomena that occurs on glenoid components following TSA. However, adjustments were necessary to conform to the ASTM standard. A Cobalt-Chromium humeral head component (Affinis Group, Overland Park, United States) was used in place of the load applicator from the previous setup to better adhere to the ASTM standard and provide findings that are comparable to those seen in the literature. As discussed in Chapter 1, a small radial mismatch in the glenoid and humeral head radius of curvature reduces the risk of glenoid loosening. By choosing a suitable humeral head prosthesis, conformity (fraction of humeral head radius over glenoid radial distance) with the 3D-printed glenoid implants was ensured. Both glenoid component models have the same material characteristics and a similar radius of curvature. Figure 4.9 displays the humeral head implant.



Figure 4.9: Affinis® CoCr Humeral Head Component.

Due to the glenohumeral joint's mobility, as described in Chapter 1, the rocking horse phenomenon can happen in any direction. However, SI edge loading occurs most frequently as a result of rotator cuff weakness or tears. The SI direction is frequently used for cyclic loading assessments due to this aspect. The highly diverse forms of the testing components in the prior configuration made it unnecessary for the load applicator to be precisely positioned along the SI axis of the components. The configuration described in the present chapter includes a method for aligning the superior-inferior axis of the glenoid component on the test frame, allowing for the replication of the same position and orientation after disassembly for cleaning or measuring. This outcome was acquired by laterally mounting an optical laser on the test frame and manually positioning the specimen so that an axial downward force was applied perpendicular to the glenoid plane along the SI axis of the glenoid. A specimen's alignment using the optical laser is shown in Figure 4.10. This feature would also help in the analysis of the test findings since wear posteriorly, anteriorly, as well as in inferior migration have been connected to glenoid loosening, which occasionally results in a noticeable tilting of the component.

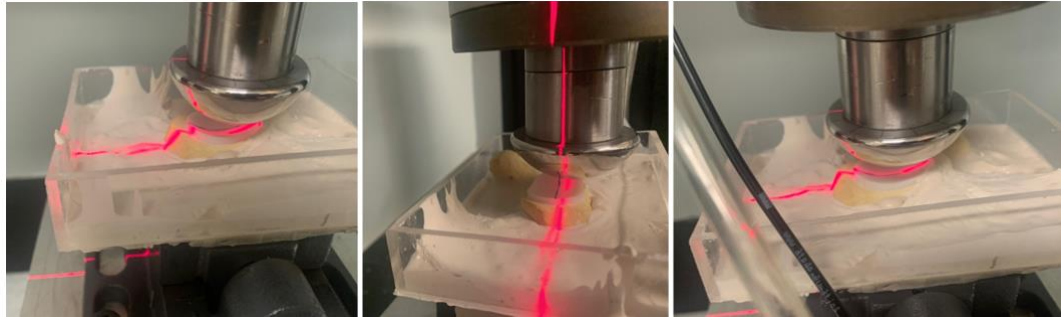


Figure 4.10: Component SI Alignment Process using the Apparatus' Optical Laser Feature.

The recommended number of cycles for the cyclic loading process is 100,000 per sample at a frequency of 1-2 Hz, as stated in the ASTM standard. However, only 10,000 cycles were suitable for this approach since it made use of 3D-printed specimens, which are substantially less durable than commercially available glenoid component implants. In the previous testing scenario, the experiment was conducted according to time rather than considering the number of cycles. The test frame configuration described in this study includes an Infrared Photoelectric Switch Sensor (Digiten Ltd., Shenzhen City, China) to record the number of cycles the load applicator completes throughout the cyclic motion. The configuration of the counting mechanism installed on the test frame is shown in Figure 4.11.

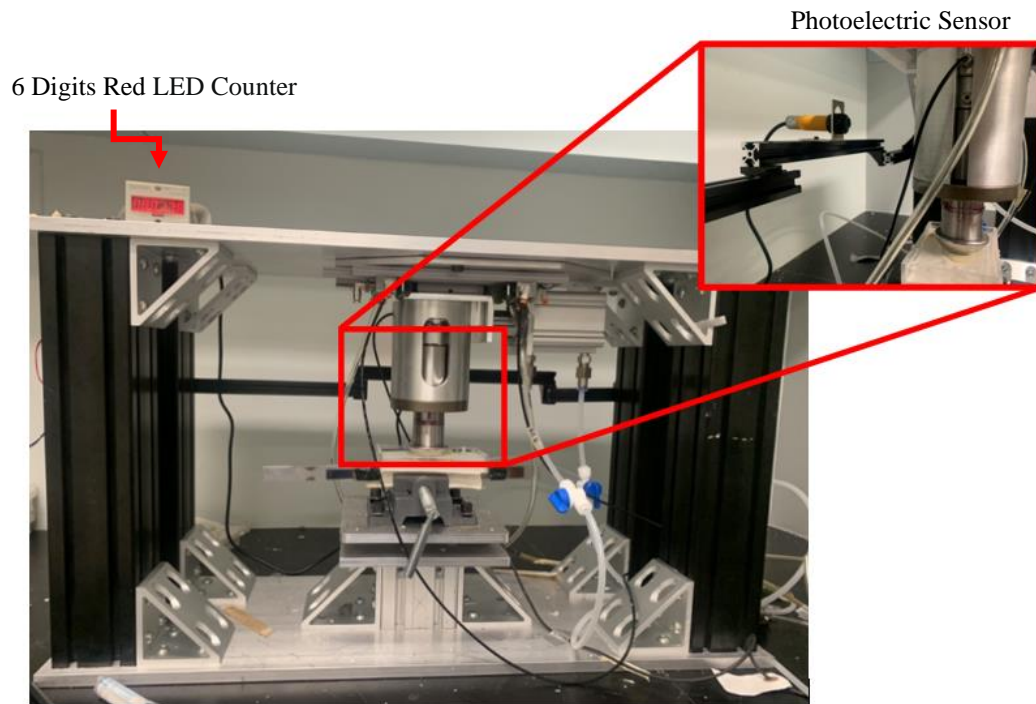


Figure 4.11: Cyclic Testing Frame including the Photoelectric Sensor and Digital Counter for Cycle counting.

4.3 Loading Protocol

Each specimen underwent subluxation translation testing in the superior and inferior directions prior to cyclic loading. The humeral head component was moved at a speed of 50 mm per minute while being subjected to a continuous axial force of 200N until a peak in shear load was noticed. The displacement at peak shear stress was characterized as the subluxation translation distance, which was measured separately for each specimen. To confirm the reliability of the proposed equipment and the feasibility of the testing technique, pre-testing verification of the experimental protocol was conducted. As required by the ASTM standard, all subluxation, pilot, and cyclic testing were performed with the specimens submerged in a water bath for lubrication. The findings of the pilot testing, which followed the same process as in this section, are in Appendix C. After subluxation and pilot testing, the cyclic tests were performed in a water bath at room temperature for 10,000 cycles at 1.3 Hz. The specimens were cyclically loaded using 90% predetermined subluxation translations while under a constant axial load of 200N.

Using the laser function to ensure SI alignment, each specimen was appropriately positioned in the testing frame. The vertical piston was manually placed at the beginning of the cyclic cycle, and the testing medium was then introduced into the specimen, which covered the surface of the component. The cycle counter was set to zero once the splash protection component had been attached. The air-supplier system was turned on and 200N load was applied through the humeral head using NI LabView software. Cyclic loading in the superoinferior direction was conducted in compliance with the ASTM Standard to replicate the rocking horse mechanism of failure in total shoulder arthroplasty. Microsoft Office Excel (2016) was used to analyze data obtained for 10,000 cycles for each specimen. In the remaining sections of this thesis, the four sets of samples that underwent individual testing will be referred to as Keeled Inlay implant (KI), Pegged Inlay implant (PI), Keeled Onlay implant (KO), and Pegged Onlay implant (PO).

4.3.1 Results

The purpose of the study in this chapter was to compare the fixation between inlay versus onlay components. Tables 4.1, 4.2, 4.3, and 4.4 provide the means and standard deviations of the components. To give further context to the numerical data, sample loosening was also factored in. The detachment of the component from the artificial bone in this scenario serves as an indicator for loosening.

Table 4.1: Summary of Test Results using the Keeled Inlay Implant Group.

<i>Sample</i>	<i>Mean (F_z)</i>	<i>Standard Deviation</i>	<i>CV</i>	<i>Loosening</i>
<i>KI 1</i>	-224.94	27.48	0.12	Yes
<i>KI 2</i>	-219.87	23.60	0.11	No
<i>KI 3</i>	-202.16	25.94	0.13	No
<i>KI 4</i>	-198.65	24.13	0.12	Yes
<i>KI 5</i>	-202.45	24.66	0.12	No
<i>KI 6</i>	-207.76	27.76	0.13	No
<i>KI Group</i>	-209.30	9.75	0.05	

Table 4.2: Summary of Test Results using the Pegged Inlay Implant Group.

<i>Sample</i>	<i>Mean (F_z)</i>	<i>Standard Deviation</i>	<i>CV</i>	<i>Loosening</i>
<i>PI 1</i>	-121.56	81.29	0.7	Yes -Failure
<i>PI 2</i>	-225.50	21.54	0.09	No
<i>PI 3</i>	-225.02	22.80	0.10	Yes
<i>PI 4</i>	-223.54	17.87	0.08	No
<i>PI 5</i>	-224.26	22.47	0.10	Yes
<i>PI 6</i>	-225.58	19.51	0.09	No
<i>PI Group</i>	-207.57	38.47	0.18	

Table 4.3: Summary of Test Results Using the Keeled Onlay Implant Group.

<i>Sample</i>	<i>Mean (F_z)</i>	<i>Standard Deviation</i>	<i>CV</i>	<i>Loosening</i>
<i>KO 1</i>	-198.95	23.02	0.12	No
<i>KO 2</i>	-203.82	21.34	0.10	No
<i>KO 3</i>	-199.85	18.51	0.09	No
<i>KO 4</i>	-203.30	20.78	0.10	No
<i>KO 5</i>	-203.26	26.62	0.13	No
<i>KO 6</i>	-200.43	21.98	0.11	No
<i>KO Group</i>	-201.60	1.92	0.009	

Table 4.4: Summary of Test Results Using the Pegged Onlay Implant Group.

<i>Sample</i>	<i>Mean (Fz)</i>	<i>Standard Deviation</i>	<i>CV</i>	<i>Loosening</i>
<i>PO 1</i>	-201.05	19.65	0.10	No
<i>PO 2</i>	-188.65	23.54	0.12	No
<i>PO 3</i>	-190.38	26.86	0.14	No
<i>PO 4</i>	-196.37	25.48	0.13	No
<i>PO 5</i>	-205.15	21.38	0.10	No
<i>PO 6</i>	-204.16	26.47	0.13	No
<i>PO Group</i>	-197.63	6.40	0.03	

Plots were generated using time as the independent parameter and the reaction force in the Z direction as the dependent variable. This was performed to examine the protocol's repeatability and the variations in the loads experienced by the implants over time.

Figures 4.12 through 4.15 provide instances of the data.

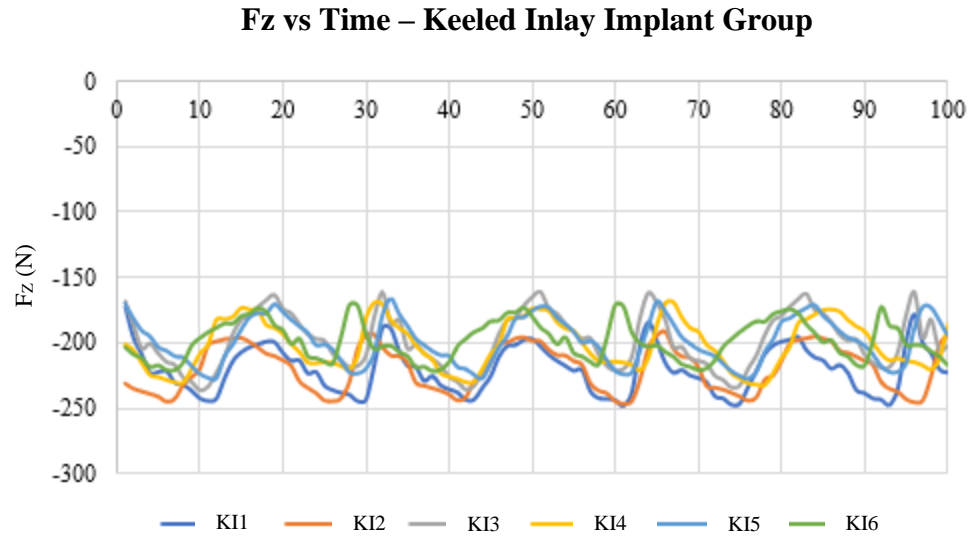


Figure 4.12: Fz versus Time graph for the Keeled Inlay Implant Group.

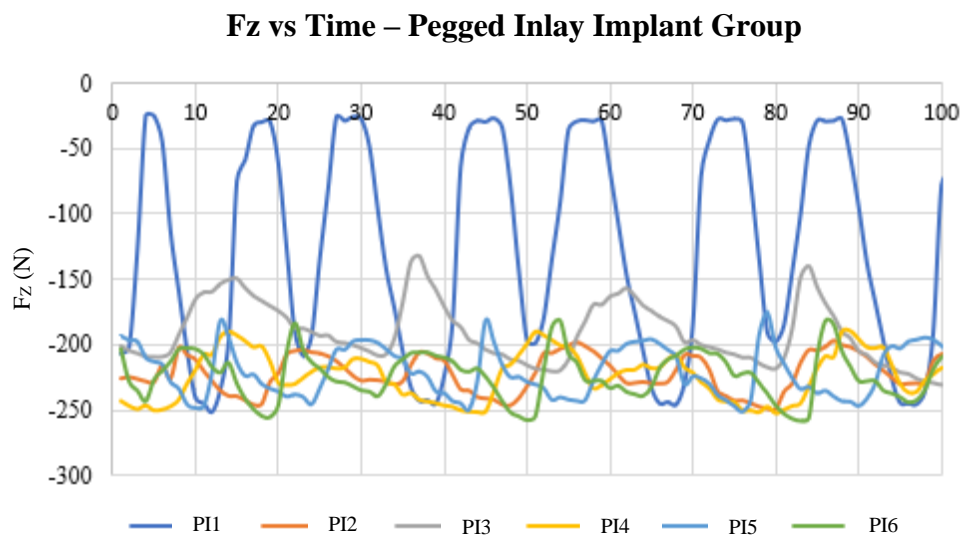


Figure 4.13: Fz versus Time graph for the Pegged Inlay Implant Group.

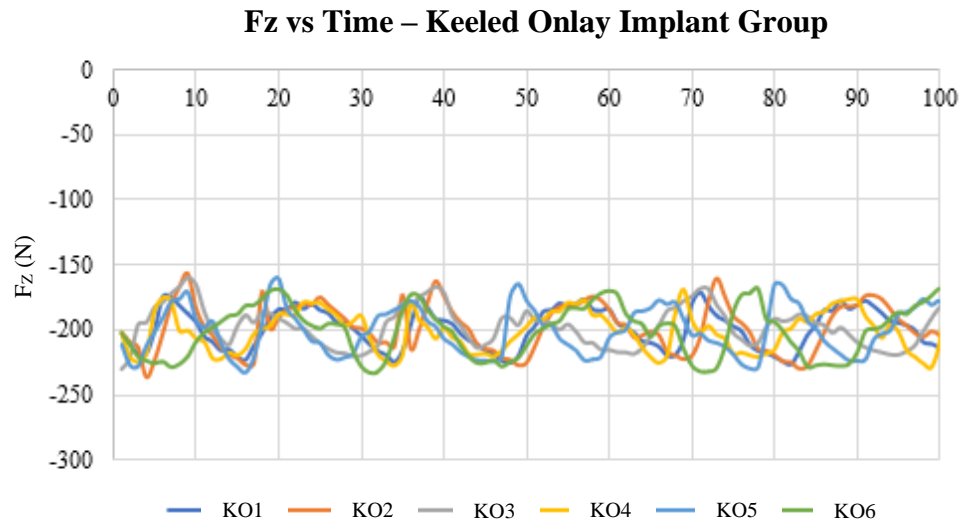


Figure 4.14: Fz versus Time graph for the Keeled Onlay Implant Group.

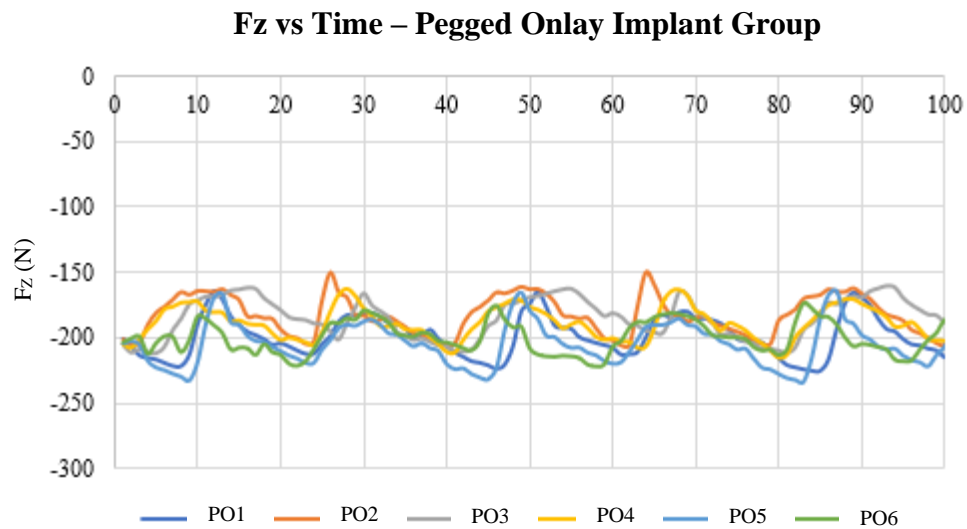


Figure 4.15: Fz versus Time graph for the Pegged Onlay Implant Group.

Since there was a slight discrepancy in the geometry of each sample within both groups of keeled and pegged components, there was speculation on how the difference would affect the loads experienced by the samples. ANOVA tests were used to assess the differences between the samples in each group. The tests employed a significance level of $p < 0.05$.

Table 4.5: Summary of ANOVA Results – Keeled Inlay Group.

<i>ANOVA - Keeled Inlay Implant Group</i>						
<i>Source of Variation</i>	<i>SS</i>	<i>df</i>	<i>MS</i>	<i>F</i>	<i>P-val.</i>	<i>F crit</i>
<i>Between Groups</i>	1987071331	5	39741426.62	62169.58525	0	2.21410381
<i>Within Groups</i>	1337085151	2091672	639.242267			
<i>Total</i>	1535792284	2091677				

Table 4.6: Summary of ANOVA Results – Pegged Inlay Group.

<i>ANOVA - Pegged Inlay Implant Group</i>						
<i>Source of Variation</i>	<i>SS</i>	<i>df</i>	<i>MS</i>	<i>F</i>	<i>P-val.</i>	<i>F crit</i>
<i>Between Groups</i>	880726419.6	5	176145283.9	120145.3042	0	2.21411455
<i>Within Groups</i>	872377670.2	595032	1466.102109			
<i>Total</i>	1753104090	595037				

Table 4.7: Summary of ANOVA Results – Keeled Onlay Group.

<i>ANOVA – Keeled Onlay Implant Group</i>						
<i>Source of Variation</i>	<i>SS</i>	<i>df</i>	<i>MS</i>	<i>F</i>	<i>P-val.</i>	<i>F crit</i>
<i>Between Groups</i>	7543863.738	5	1508772.748	3066.882303	0	2.21410389
<i>Within Groups</i>	1010085129	2053200	491.9565209			
<i>Total</i>	1017628992	2053205				

Table 4.8: Summary of ANOVA Results – Pegged Onlay Group.

<i>ANOVA - Pegged Onlay Implant Group</i>						
<i>Source of Variation</i>	<i>SS</i>	<i>df</i>	<i>MS</i>	<i>F</i>	<i>P-val.</i>	<i>F crit</i>
<i>Between Groups</i>	95667398.09	5	19133479.62	33093.02924	0	2.21410336
<i>Within Groups</i>	1350120682	2335152	578.1725052			
<i>Total</i>	1445788080	2335157				

A further point of interest was whether there would be substantial differences in reaction forces between the components from the inlay and onlay groups. Tables 4.9 through 4.13 present the results of the comparison of the two groups of pegged and keeled components using t-tests and two-way ANOVA tests with a significance level of 0.05. Figure 4.15 displays the mean F_Z values for each group along with their respective standard deviations.

Table 4.9: Summary of Fz Mean of all samples.

	<i>KI</i>	<i>KO</i>	<i>PI</i>	<i>PO</i>
<i>Sample 1</i>	-224.94	-198.95	-121.56	-201.05
<i>Sample 2</i>	-219.87	-203.82	-225.50	-188.65
<i>Sample 3</i>	-202.16	-199.85	-225.02	-190.38
<i>Sample 4</i>	-198.65	-203.30	-223.54	-196.37
<i>Sample 5</i>	-202.45	-203.26	-224.26	-205.15
<i>Sample 6</i>	-207.76	-200.43	-225.58	-204.16
<i>Group Mean</i>	-209.30	-201.60	-207.57	-197.63
<i>Std Deviation</i>	9.75	1.92	38.47	6.40

Table 4.10: Summary of t-test Results - Keeled Implant.

	<i>Variance</i>	<i>df</i>	<i>Significance</i> (2-tailed) ($p < 0.05$) *	<i>Conclusion</i>
<i>KI</i>	113.99	5	0.11	No significant difference between groups
<i>KO</i>	4.40			

Table 4.11: Summary of t-test Results - Pegged Implant.

	<i>Variance</i>	<i>df</i>	<i>Significance</i> (2-tailed) ($p < 0.05$) *	<i>Conclusion</i>
<i>PI</i>	1776.14	5	0.58	No significant difference between groups
<i>PO</i>	49.16			

Table 4.12: Summary of ANOVA results - KI, KO, PI, PO.

<i>ANOVA – Two Factor</i>							
<i>Source of Variation</i>	<i>SS</i>	<i>df</i>	<i>MS</i>	<i>F Value</i>	<i>P-value</i>	<i>F crit</i>	<i>Conclusion</i>
<i>Sample</i>	48.90	1	48.90	0.10	0.75	4.35	F < F crit
<i>Columns</i>	467.18	1	467.18	0.96	0.34	4.35	P > 0.05
<i>Interaction</i>	7.59	1	7.59	0.016	0.90	4.35	Accept null hypothesis
<i>Within</i>	9718.56	20	485.93				
<i>Total</i>	10242.22	23					

Table 4.13: Welch's t-test results – KI, KO, PI, PO

	<i>Inlay</i>	<i>Onlay</i>	<i>Conclusion</i>
<i>Mean</i>	-208.44	-199.62	p > 0.05
<i>df</i>		12	t Stat < t Crit
<i>t Stat</i>		-1.02	Means are
<i>t critical two-tail</i>		2.18	equal
<i>p (T=t) two-tail</i>		0.32	

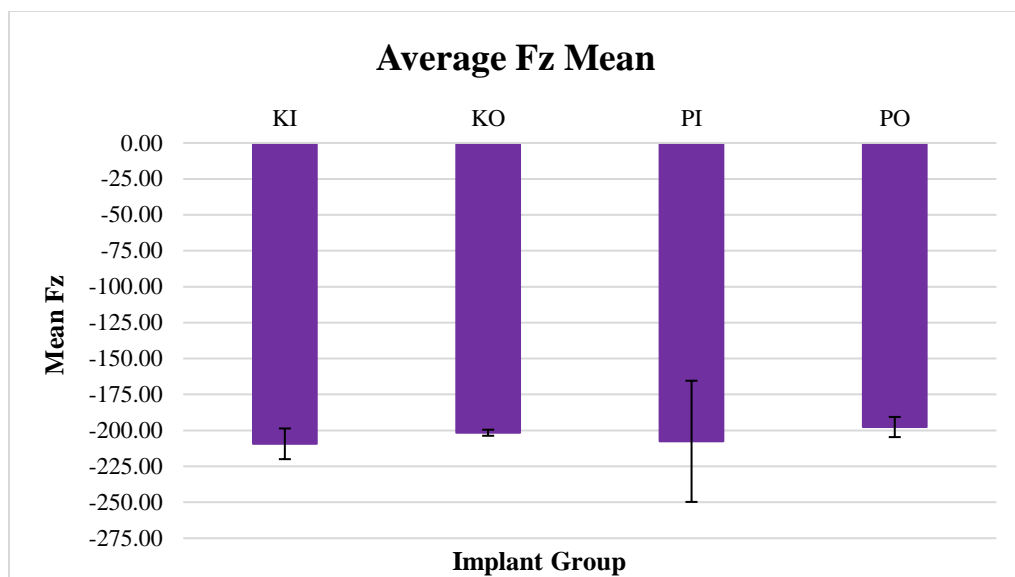


Figure 4.16: Average Fz Mean for all groups.

4.3.2 Analysis

Numerous factors are identified in the literature as contributing to glenoid loosening, including high tension at the cement layer [130], [131], component mismatch [132], implant malposition [133], bone-cement interface micromotion [134], [135], and component fixation failure [136]–[138]. The current investigation comprised two predominant glenoid component fixation methods, peg and keel components. According to multiple studies, glenoid implants with peg fixation outperformed glenoid implants with keel fixation in terms of the experimental technique [139], radiolucencies, and FE analysis [138]. In addition to the two modes of fixation, this study was interested in the ramifications of having inlay and onlay components.

All specimens exhibited complete stability during the cyclic loading trials. The 24 glenoid components evaluated showed surface deformation, with significant edge fractures being visible in 23 specimens. Deformation occurred in the superior and inferior quadrants with varying degrees of severity in 100% of components with deformed edges (Figure 4.17).

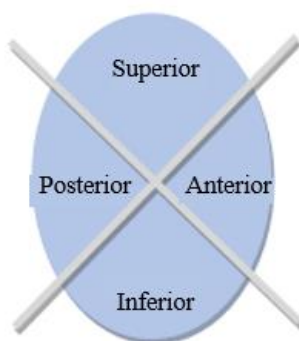


Figure 4.17: Glenoid Quadrants.

The rocking horse phenomenon has been described as the mechanism by which edge loading leads to component loosening. Eccentric forces are generated on the glenoid rim as the prosthetic humeral head moves inferiorly and superiorly. These forces eventually lead to edge deformation. Since a decreased force was applied to the specimens due to their material characteristics, component loosening was only seen in 8.3% of the specimens, even though edge deformation was present in all specimens, indicating an incidence of edge loading. Additionally, component loosening only occurred on specimens from the inlay group, indicating that it was a fixture vulnerability resulting from the inlay technique. The slight asymmetry in the degree of deformation between the superior and inferior quadrants could have been caused by several factors, including an uneven cemented position, component misalignment, and discrepancies during the TSA operation (since it was previously mentioned that all specimens differ slightly from one another), or more friction in the vertical bearing when moving inferiorly or superiorly under load.

For a few specimens across all groups, lower reaction load values were detected. Reduced edge loads act as a secondary, indirect indicator of glenoid loosening. When the implant loosens, a force applied eccentrically from the center of the glenoid component produces rotation of the glenoid component, resulting in a loss in the glenoid's restriction against superoinferior forces. Although there were no discernible changes in edge loads between the groups, samples from the medium inlay component group revealed decreasing edge loads during the cyclic testing. Tables 4.1 to 4.4 show the computed mean F_z values and standard deviations for each sample group. Essentially, the overall

reaction forces in the Z direction were consistent during the experiment. Outcomes were affected by fracture and component loosening in addition to motion direction and load application area. The standard deviation of the data is relatively low, notably when examining the average group means and related standard deviations alone, as all samples had coefficients of variation that were far below 1. Essentially, the inconsistencies in reaction forces mirror the variations in the functioning mechanisms and components of shoulder biomechanics. The ensuing contact forces in the shoulder may be inversely correlated with the direction of motion. Depending on the applied forces, different loads are generated across the shoulder joint throughout its motion.

In Figures 4.12 through 4.15, a portion of the force in the Z direction for the six individual specimens from each group can be seen. The plots were assessed to evaluate the correlation between the reaction force values and the occurrence of glenoid component loosening, as well as the correlation between the mean F_z values, cycle time, and pattern of load dispersion over the surface of the component during the initial and final testing protocol stages. The patterns and modes of load propagation over the surface of the glenoid component are depicted in each graph, including steady or hesitant, ascending or descending, linear, and irregular. The force reactions at the extremities of the components are reflected by the largest peaks in the negative direction (approaching -250N), whilst those at the center of the components are characterized by lower values (slightly closer to -150N or less). In line with expectations, the results for the specimen's center were lower than the extremities' values. Periphery loading causes more stress than center and transition zone loading as reported in the literature. Peak loads in the core zone of the components on the samples that experienced loosening were reported to be significantly lower than on the samples where loosening did not occur. Fluctuation throughout the center zone of the glenoid is visible in the plots as a result of friction and damage to the specimen due to the component's low toughness.

The graphs displayed in Figures 4.12 to 4.15 exhibit consistency between cycles, which is required for this procedure. Additionally, the average reaction force in the Z direction is close to -200N, which is in alignment with the system's applied load. This demonstrates that the testing procedure satisfies the cycle's and load's repeatability requirements. The

graphs further demonstrate that the components of the inlay group had larger reaction loads than those of the onlay groups. This is due to the inlay structures' greater stiffness, which resist applied loads and movements better than the onlay components, which are less stiff since they do not contain peripheral bone. The loosening of two samples from the pegged inlay group resulted in the reduced loads observed in the plot (Figure 4.13). All specimens were loaded at 200N for 10,000 cycles, albeit the duration of each test varied. The tests using the small-keeled specimen model were completed relatively faster than those using the medium-pegged specimen model because it had a shorter distance between the inferior and superior ends—roughly 30 mm as opposed to 34 mm for the latter. The models' times differed by approximately 13%.

Through the use of ANOVA analysis, differences in the means of the implants were identified. The findings displayed in Tables 4.5 through 4.8 demonstrate a substantial difference between the means of each sample within their respective groups. This is probably the outcome of the different implant seating positions, as noted previously, as well as size variations. Studies have revealed that improper implant placement during bone implantation might lead to unwanted high stress [140]. The coefficient of variation derived from the standard deviation for each sample was substantially low, indicating that the means were significantly equivalent to one another even though the ANOVA results did not establish the means of the samples as equal. The difference between the means of the pegged onlay and pegged inlay component groups was 3.59 %, with the former obtaining a value closer to the applied load. Furthermore, the two keeled implant groups' standard deviation values revealed that the component group that was installed using the onlay technique performed better as shown in Figure 4.16. A larger discrepancy of 9.97 % separated the means of the onlay and inlay groups for the pegged implant groups, with the onlay group once again recording a mean value that was closer to the applied load. In comparison to the inlay design, the onlay specimens recorded lower forces and standard deviations. Once more, this is due to the fact that the onlay design does not include the peripheral bone, which reduces the implant's stiffness and causes it to produce lower reaction loads. Tables 4.9 through 4.13 present the findings of further two-way ANOVA analyses and Welch's t-tests used to compare the components from the onlay and inlay groups. The premise for this investigation was that the Inlay approach would result in a

stiffer construct. The larger reaction loads observed support this hypothesis. Welch's t-test was used to determine whether the means of the inlay and onlay groups were equal. The results validated the null hypothesis that the means are equal. A two-way ANOVA was then used to evaluate the influence of inlay vs onlay procedures on keeled and pegged components. The findings of the two-way ANOVA analysis revealed that there was no significant interaction between the effects of the implant fixation technique and the implant type. Despite the fact that the inlay group had higher reaction loads, there was no significant difference in the means of the groups. This suggests that the outcomes obtained are not directly influenced by the fixation technique and the use of pegged or keeled implants. It is imperative to emphasize that no conclusions concerning the type of fixation should be drawn from these results since the components used in this protocol are inadequate for such inferences.

This investigation's goal was to develop a cyclic testing technique that could carry out glenoid fixation testing in accordance with ASTM standards. The study's results, while not directly comparable, are consistent with literature in terms of edge loading patterns and elevated stress regions. Some restrictions apply to this investigation. This study employed synthetic shoulder components and 3D-printed glenoid implant components to enable performance evaluations for this implementation. As a result, there are still numerous uncertainties regarding the potential effects of employing the testing methodology system with human bone samples and implants that are currently on the market.

4.4 Chapter Summary

This chapter discusses the improvements to the experimental equipment presented in Chapter 3. The upgraded testing apparatus consists of an ASTM F2028-compliant rig system that uses a load cell and NI LabView to monitor the force exerted on the testing components. The reaction forces between four distinct groups of glenoid components—two inlay component sets and two onlay component groups—are also examined in this chapter. Six normal shoulder models with small keeled glenoid implants and six B2 models with medium-pegged glenoid prostheses with a 25° wedge were included in each

set. Regardless of having inferior material properties to those of medical-grade glenoid implants, 3D-printed glenoid implants were chosen for this technique due to their low cost and ease of production. The test frame developed in Chapter 3 was capable of reproducing the necessary cyclic motion to model the rocking horse phenomenon that occurs on glenoid components after TSA. Nonetheless, modifications were required to meet the ASTM standard, including the addition of a mechanism for applying a liquid testing medium, a method for aligning the glenoid component's superoinferior axis on the testing frame, and a system for measuring the number of cycles performed for during each cyclic protocol.

Results of the protocol utilizing 24 glenoid components revealed surface deformation, with edge fractures apparent in 23 specimens. In line with expectations, deformation happened in the superior and inferior quadrants. Interestingly, component loosening was limited to specimens from the robot group, suggesting that the TSA treatment performed by the robot was responsible for the fixture vulnerability. In general, the reaction forces in the Z direction remained constant throughout the experiment. Although the ANOVA tests could not establish the means of the samples as equal, the coefficient of variation generated from the standard deviation for each sample was noticeably low, suggesting that the means within their groups were virtually equivalent to one another. Furthermore, there was a much smaller and less significant difference between the means of the keeled inlay and keeled onlay component groups than there was for the means of the pegged component groups. Despite the apparent superior functionality of the inlay components, student Welch's t-test and two-way ANOVA findings reveal no significant difference in the means of the four groups, indicating that they are essentially identical. The study's findings are in line with the theory in terms of edge loading patterns and high-stress areas, albeit not being directly comparable. The findings of the experiments performed with the upgraded testing apparatus show that the device is capable of executing the ASTM standard cyclic loading methodology and that the experiment could be replicated with actual specimens.

Chapter 5

5 Conclusion

OVERVIEW: In this concluding chapter, the goals of the thesis are evaluated in relation to the studies that were conducted, their findings and relevance are summarized, and the individual outcomes are restated in light of the overall importance of the thesis work.

Based on the thesis' findings, the thesis' strengths and weaknesses are examined, and the study's future course is described.

5.1 Summary

This study's major goal was to develop and evaluate the performance of an ASTM-compliant cyclic loading testing device. This was achieved by performing a series of protocols to examine the reaction forces that impact glenoid components during cyclic loading. Failure of the glenoid component is still the most common complication in total shoulder arthroplasty. The main mechanism of glenoid component loosening, known as the rocking horse phenomenon, occurs in reaction to glenohumeral forces that are not centered on the component. Reaction forces are seldom explicitly addressed in biomechanical assessments of glenoid components, despite the rising prevalence of total shoulder arthroplasty and the connection between glenoid design and failure rates. The provided body of work validates prior findings of high reaction loads in glenoid components.

Firstly, reaction forces were measured by performing experimental cyclic loading experiments on a variety of components using a Stewart platform. This system was designed to present a foundational understanding of response force behavior based on component geometry (Chapter 2). Further improvement of the testing protocol and the design of a cyclic testing frame was performed to examine the load reaction as a function of component shape. The effectiveness of the two testing procedures in replicating edge loading and providing insight into the reaction forces that arise on cyclically loaded components was compared (Chapter 3). An association between component shape and reactive loads under cyclic loading was successfully established by the enhanced testing technique. To develop a testing technique that complied with the ASTM F2028 however, additional alterations were required. As a result, the novel testing apparatus was enhanced further, and a new experimental protocol to explore the reaction forces of four different groups of cyclically loaded glenoid components was performed. Two of the groups had onlay fixation, while the other two had inlay fixation. Each set comprised six B2 models with medium-pegged glenoid prosthesis with a 25° wedge and six normal shoulder models with small-keeled glenoid implants (Chapter 4). Lastly, the relationship between component shape and reaction forces demonstrated in Chapters 2 and 3, as well as the results of the ASTM compliant procedure stated in Chapter 4, were consistent with theory

regarding edge loading and provide information that can be useful in developing new techniques to reduce the rates of glenoid loosening following TSA procedures.

Regarding objective 1, cyclic tests on three distinct component geometries were conducted utilizing the Stewart platform and a novel testing frame, as described in Chapters 2 and 3, respectively, to evaluate the shape dependence of the reaction forces. Three different component designs—rectangular, triangular, and concave—were assessed under loads of 300, 500, and 750 N. The Stewart platform's results showed that the device was unsuccessful at applying a complete load to the component's surface, resulting in loads that were different from the anticipated reaction forces. Nevertheless, the experimental apparatus was suitable for identifying differences in response forces during the cyclic loading protocols. The findings indicated that the high force responses observed in previously tested components were geometry reliant. The introduction of the innovative testing frame further clarified the results by revealing values that were closer to the actual applied compressive loads, with the maximum recorded values exceeding the applied loads, as would be anticipated based on prior research. Due to the difference in surface depth/height, peripheral loading causes more stress on glenoid components edges than center and transition zone loading. The higher surface areas of the three distinct designs were therefore anticipated to experience loads greater than those applied. Greater reaction loads do occur at higher surface areas, according to the results of the assessments performed with both testing mechanisms. In addition, the findings in Chapter 3 also demonstrated an increase in forces due to friction in both the X and Y axes. The lack of a fluid testing medium and the prolonged contact between the load applicator's face and the surface of the component were the two main causes of the increased friction. Overall, the testing outcomes acquired with the new testing rig were far superior to those obtained with the previous arrangement. The observations support the argument that the glenoid component's design influences reaction forces. This information can assist in the creation of innovative glenoid implants that reduce the stresses that generate the rocking horse phenomena.

Addressing objective 2, the testing device created in Chapter 3 underwent changes to comply with the ASTM F2028 standard. A motion and force control system, a lubrication

system, a method of mounting and enclosing the test specimen, alignment and positioning of the glenoid component, and the ability to reproduce the cyclic motion are all required for the testing protocol to comply with the standard. Firstly, the created testing apparatus is a pneumatic system with an air supply controlling the horizontal movement. The vertical load is controlled by NI LabView software connected to a power supply and a USB-6211 data acquisition device. Switches installed on the testing frame control its cyclic motion, ensuring proper cyclic protocol execution. As a means of mounting the test specimen, the apparatus was equipped with a vise to maintain the specimens in place during testing. Laterally installing an optical laser on the test frame and physically setting the specimen so that the cyclic motion would be executed along its SI axis allowed for the acquisition of alignment and positioning adherence. The SI axis was manually defined on the component faces before testing in pursuance of accomplishing alignment with the optical laser. In the interest of incorporating a lubricating system, the novel testing protocol included a container that was cemented around the test specimens, and water was used as the testing medium. Through the use of this feature, it was feasible to preserve the immersion of the load applicator and glenoid components' contact surfaces in the fluid test medium during the protocol. A sensor for counting the number of cycles the load applicator completes during the cyclic motion was also included in this testing frame. Due to all the adjustments implemented, the previously stated hypothesis was verified, and the testing apparatus was deemed ASTM-compliant. The tests conducted using this apparatus validated both the viability of the testing method and the dependability of the proposed equipment.

Using the developed testing equipment, objective 3 was focused on analyzing the compressive response forces on keeled and pegged glenoid components. According to biomechanical research, pegged fixation is more resistant to high shear stresses than keeled glenoid components and may result in a slower rate of loosening [141]–[143]. However, the wide range of fixation techniques seen on prosthetic implants suggests that there is ambiguity regarding the most effective fixation design for minimizing stress and relative motion at the bone-implant interface. The glenoid components tested showed surface deformation, with edge fracture visible in 95.8% of specimens. Expectedly, the superior and inferior quadrants experienced deformation in all components. The SI

quadrant reportedly has the highest articular contact at the glenohumeral joint following TSA and is not focused on the glenoid surface. Component loosening was peculiarly restricted to specimens from the inlay group, which raises the intriguing possibility that the fixture vulnerability was caused by the fixation technique. In addition, the components used in this protocol were 3D printed, which have much lower resistance than those available on the market. Due to the intrinsic disparities in the structural and material qualities between the prosthetic glenoid and native glenoid, it is challenging to optimize the mechanics of the prosthetic joint. Furthermore, compared to the means of the medium-pegged component groups, there was a significantly smaller and less significant difference between the small-keeled inlay and onlay component group means. The observations of the experimental study appear to favor the keeled onlay components, nonetheless, the t-test and ANOVA results showed no significant variations in the means of the four groups, demonstrating that they are essentially the same. These findings support the third hypothesis of the current body of work since no discernible difference was observed when the tests were conducted utilizing the different fixation specimens, confirming that reaction forces, while shape-dependent, might not specifically altered by the use of pegged or keeled implants. Wider, in-depth investigations contrasting pegged and keeled glenoid components are necessary to address the problem of glenoid loosening, especially in regard to functional outcomes and load reaction behavior.

5.2 Strengths and Limitations

This study's development of a cyclic loading testing frame for glenoid component evaluation was one of its main strengths. Despite the particular set of testing conditions that the experimental setup used in this body of work possesses, it is still possible to infer conclusions about the behavior of the reaction forces from the literature. This study proposed a unique approach for evaluating compressive response forces on glenoid components during cyclic loading simulation utilizing a novel testing frame. The device's simulation of loading conditions is comparable to the mechanics of active compressive glenohumeral forces that occur during humeral head compression into the glenoid component. Even though it is difficult to exactly establish a relation between experimental investigations that incorporate distinct methods and make different

assumptions, the similarity in force behavior among studies indicates that significantly larger forces are experienced at the edges of the component, which induces edge loading and ultimately leads to glenoid loosening.

Because there are intrinsic discrepancies between the 3D printing polymer and medical-grade implants and between foam polyurethane Sawbone and cancellous bone, employing Sawbone analogs and 3D-printed components to conduct the cyclic assessments might be considered a constraint. Nevertheless, there are variances in the organic bone's structural composition as well as the materials utilized for creating implants. Through the utilization of these economical and reliable test specimens in this protocol evaluation, it was possible to identify the factors for inconsistencies in the findings of the four cyclically loaded groups. Although the magnitudes of the load reactions are expected to differ between 3D-printed components and medical-grade implants, the force behavior observed throughout the cyclic trials is characteristic of the edge loading phenomena, which would thus be transferrable to implants currently on the market. Another limitation is that a relatively small number of specimens were used to evaluate the research hypotheses (24 specimens). The acquisition of more comprehensive data and the discovery of further observations may emerge from applying the explored hypothesis to broader research including a greater number of specimens.

Notwithstanding these potential downsides, this work presents a novel experimental technique that enables direct, contact measurement of the magnitude of the reaction forces at the glenoid during a cyclic protocol in accordance with the ASTM F2028 standard.

5.3 Future Work and Conclusion

Although the predictions of this body of work were compatible with the observed data, additional work is required for a complete evaluation of glenoid component loosening. The proposed protocol might be enhanced by including microfocus computed tomography (μ CT) to measure experimental stresses that exist throughout the bone-cement interface of glenoid implants. Using micro-CT, slice images and 3D volumes of

the internal microarchitecture of various materials can be obtained. To gain more knowledge about the variations in load transfer mechanisms across the examined groups, imaging would be captured before and after the cyclic trials were conducted. These experiments, however, would be performed with commercially available keeled and pegged components implanted on organic bone. Cone-beam micro-CT scanner compatibility was taken into account when designing the suggested testing frame. The materials currently used in the carriage assembly, specifically the vertical and horizontal pistons as well as the humeral head component, are micro-CT compatible. The procedure for integrating micro-CT would involve mounting the carriage onto the hexapod robot to take initial measurements of the specimens, followed by performing the loading routine using the cyclic rig to complete 10,000 cycles. Subsequent to the cyclic protocol, the carriage would be placed once again on the Stewart platform to obtain more measurements and this sequence would be repeated until completing 100,000 cycles or until failure occurs. Additionally, a post-processing procedure to prepare the volumetric images for digital volume correlation would also be incorporated into this combined protocol. Collectively, this approach would enable the calculation of internal deformations (displacements and strains) within the trabecular bone to be calculated under external loading. Another addition to the system would be the inclusion of a heated water bath method to use water at 37 degrees Celsius as stated in the ASTM standard. The long-term objective of this combined protocol is to contribute to the body of knowledge regarding edge loading-related glenoid component failure following total shoulder arthroplasty surgery.

References

- [1] C. McCausland, E. Sawyer, B. J. Eovaldi, and M. Varacallo, “Anatomy, Shoulder and Upper Limb, Shoulder Muscles,” *StatPearls*, Aug. 2021, Accessed: May 24, 2022. [Online]. Available: <https://www.ncbi.nlm.nih.gov/books/NBK534836/>
- [2] S. Scholarship@western and J. R. Targosinski, “The Application of Digital Volume Correlation Bone Strain The Application of Digital Volume Correlation Bone Strain Measurements in the Osteoarthritic Glenohumeral Joint Measurements in the Osteoarthritic Glenohumeral Joint.”
- [3] L. J. Soslowsky, E. L. Flatow, L. U. Bigliani, and V. C. Mow, “Articular geometry of the glenohumeral joint.,” *Clin Orthop Relat Res*, no. 285, pp. 181–90, Dec. 1992.
- [4] J. J. P. Warner, M. K. Bowen, X. Deng, J. A. Hannafin, S. P. Arnoczky, and R. F. Warren, “Articular contact patterns of the normal glenohumeral joint,” *J Shoulder Elbow Surg*, vol. 7, no. 4, pp. 381–388, Jul. 1998, doi: 10.1016/S1058-2746(98)90027-1.
- [5] W. Scholarship and C. Daniel Smith, “Development of a Force-Space Navigation for Surgical Robotics,” 2018. Accessed: Aug. 27, 2022. [Online]. Available: <https://ir.lib.uwo.ca/etdhttps://ir.lib.uwo.ca/etd/5177>
- [6] S. R. Pai and M. M. Pai, “Morphometry of Glenoid Cavity”.
- [7] P. T. Cowan, A. Mudreac, and M. Varacallo, “Anatomy, Back, Scapula,” *StatPearls*, Aug. 2021, Accessed: May 24, 2022. [Online]. Available: <https://www.ncbi.nlm.nih.gov/books/NBK531475/>
- [8] G. Milano and A. Grasso, “Shoulder arthroscopy: Principles and practice,” *Shoulder Arthroscopy: Principles and Practice*, pp. 1–622, Jan. 2014, doi: 10.1007/978-1-4471-5427-3.

- [9] A. Alashkham, A. Alraddadi, P. Felts, and R. Soames, "Histology, vascularity and innervation of the glenoid labrum," *Journal of Orthopaedic Surgery*, vol. 26, no. 2, p. 230949901877090, May 2018, doi: 10.1177/2309499018770900.
- [10] E. J. Strauss, C. Roche, P.-H. Flurin, T. Wright, and J. D. Zuckerman, "The glenoid in shoulder arthroplasty," *Journal of Shoulder and Elbow Surgery Board of Trustees*, 2009, doi: 10.1016/j.jse.2009.05.008.
- [11] A. J. Checroun, C. Hawkins, F. J. Kummer, and J. D. Zuckerman, "Fit of current glenoid component designs: An anatomic cadaver study," *J Shoulder Elbow Surg*, vol. 11, no. 6, pp. 614–617, Nov. 2002, doi: 10.1067/mse.2002.126099.
- [12] W. J. Mallon, H. R. Brown, J. B. Vogler, and S. Martinez, "Radiographic and geometric anatomy of the scapula.," *Clin Orthop Relat Res*, no. 277, pp. 142–54, Apr. 1992.
- [13] R. S. Churchill, J. J. Brems, and H. Kotschi, "Glenoid size, inclination, and version: An anatomic study," *J Shoulder Elbow Surg*, vol. 10, no. 4, pp. 327–332, Jul. 2001, doi: 10.1067/mse.2001.115269.
- [14] W. Scholarship, A. Gupta, L. M. Ferreira, J. Supervisor, and G. Athwal, "The Role of Scapular Morphology in Reverse Shoulder The Role of Scapular Morphology in Reverse Shoulder Arthroplasty Arthroplasty," 2016.
- [15] J. P. Iannotti, J. P. Gabriel, S. L. Schneck, B. G. Evans, and S. Misra, "The normal glenohumeral relationships. An anatomical study of one hundred and forty shoulders.," *J Bone Joint Surg Am*, vol. 74, no. 4, pp. 491–500, Apr. 1992.
- [16] R. E. Hughes *et al.*, "Glenoid Inclination is Associated With Full-Thickness Rotator Cuff Tears," *Clin Orthop Relat Res*, vol. 407, pp. 86–91, Feb. 2003, doi: 10.1097/00003086-200302000-00016.
- [17] A. Maurer *et al.*, "Assessment of glenoid inclination on routine clinical radiographs and computed tomography examinations of the shoulder," *J Shoulder*

- Elbow Surg*, vol. 21, no. 8, pp. 1096–1103, Aug. 2012, doi: 10.1016/j.jse.2011.07.010.
- [18] R. E. Hughes *et al.*, “Glenoid Inclination is Associated With Full-Thickness Rotator Cuff Tears,” *Clin Orthop Relat Res*, vol. 407, pp. 86–91, Feb. 2003, doi: 10.1097/00003086-200302000-00016.
 - [19] G. G. Konrad *et al.*, “Decreasing glenoid inclination improves function in shoulders with simulated massive rotator cuff tears,” *Clinical Biomechanics*, vol. 21, no. 9, pp. 942–949, Nov. 2006, doi: 10.1016/j.clinbiomech.2006.04.013.
 - [20] A. S. Wong, L. Gallo, J. E. Kuhn, J. E. Carpenter, and R. E. Hughes, “The effect of glenoid inclination on superior humeral head migration,” *J Shoulder Elbow Surg*, vol. 12, no. 4, pp. 360–364, Jul. 2003, doi: 10.1016/S1058-2746(03)00026-0.
 - [21] R. E. Hughes *et al.*, “Glenoid Inclination is Associated With Full-Thickness Rotator Cuff Tears,” *Clin Orthop Relat Res*, vol. 407, pp. 86–91, Feb. 2003, doi: 10.1097/00003086-200302000-00016.
 - [22] P. Tétreault, A. Krueger, D. Zurakowski, and C. Gerber, “Glenoid version and rotator cuff tears,” *Journal of Orthopaedic Research*, vol. 22, no. 1, pp. 202–207, Jan. 2004, doi: 10.1016/S0736-0266(03)00116-5.
 - [23] U. Kandemir, R. B. Allaire, J. T. Jolly, R. E. Debski, and P. J. McMahon, “The relationship between the orientation of the glenoid and tears of the rotator cuff,” *J Bone Joint Surg Br*, vol. 88-B, no. 8, pp. 1105–1109, Aug. 2006, doi: 10.1302/0301-620X.88B8.17732.
 - [24] R. J. Friedman, K. B. Hawthorne, and B. M. Genez, “The use of computerized tomography in the measurement of glenoid version.,” *J Bone Joint Surg Am*, vol. 74, no. 7, pp. 1032–7, Aug. 1992.
 - [25] M. Randelli and P. L. Gambrioli, “Glenohumeral osteometry by computed tomography in normal and unstable shoulders.,” *Clin Orthop Relat Res*, no. 208, pp. 151–6, Jul. 1986.

- [26] G. Welsch *et al.*, “CT-Based Preoperative Analysis of Scapula Morphology and Glenohumeral Joint Geometry,” *Computer Aided Surgery*, vol. 8, no. 5, pp. 264–268, Jan. 2003, doi: 10.3109/10929080309146062.
- [27] D. J. Bokor, M. D. O’Sullivan, and G. J. Hazan, “Variability of measurement of glenoid version on computed tomography scan,” *J Shoulder Elbow Surg*, vol. 8, no. 6, pp. 595–598, 1999, doi: 10.1016/S1058-2746(99)90096-4.
- [28] C. D. Bryce, A. C. Davison, G. S. Lewis, L. Wang, D. J. Flemming, and A. D. Armstrong, “Two-dimensional glenoid version measurements vary with coronal and sagittal scapular rotation,” *J Bone Joint Surg Am*, vol. 92, no. 3, pp. 692–699, Mar. 2010, doi: 10.2106/JBJS.I.00177.
- [29] Y. W. Kwon, K. A. Powell, J. K. Yum, J. J. Brems, and J. P. Iannotti, “Use of three-dimensional computed tomography for the analysis of the glenoid anatomy,” *J Shoulder Elbow Surg*, vol. 14, no. 1, pp. 85–90, Jan. 2005, doi: 10.1016/j.jse.2004.04.011.
- [30] J. J. Scalise, M. J. Codsì, J. Bryan, and J. P. Iannotti, “The three-dimensional glenoid vault model can estimate normal glenoid version in osteoarthritis,” *J Shoulder Elbow Surg*, vol. 17, no. 3, pp. 487–491, May 2008, doi: 10.1016/J.JSE.2007.09.006.
- [31] R. W. Nyffeler, B. Jost, C. W. A. Pfirrmann, and C. Gerber, “Measurement of glenoid version: conventional radiographs versus computed tomography scans,” *J Shoulder Elbow Surg*, vol. 12, no. 5, pp. 493–496, Sep. 2003, doi: 10.1016/S1058-2746(03)00181-2.
- [32] T. A. Shapiro, M. H. McGarry, R. Gupta, Y. S. Lee, and T. Q. Lee, “Biomechanical effects of glenoid retroversion in total shoulder arthroplasty,” *J Shoulder Elbow Surg*, vol. 16, no. 3 Suppl, May 2007, doi: 10.1016/J.JSE.2006.07.010.

- [33] A. Farron, A. Terrier, and P. Büchler, “Risks of loosening of a prosthetic glenoid implanted in retroversion,” *J Shoulder Elbow Surg*, vol. 15, no. 4, pp. 521–526, Jul. 2006, doi: 10.1016/J.JSE.2005.10.003.
- [34] P. Clavert, P. J. Millett, and J. J. P. Warner, “Glenoid resurfacing: what are the limits to asymmetric reaming for posterior erosion?,” *J Shoulder Elbow Surg*, vol. 16, no. 6, pp. 843–848, Nov. 2007, doi: 10.1016/J.JSE.2007.03.015.
- [35] D. Pinkas, B. Wiater, and J. Michael Wiater, “The glenoid component in anatomic shoulder arthroplasty,” *Journal of the American Academy of Orthopaedic Surgeons*, vol. 23, no. 5, pp. 317–326, May 2015, doi: 10.5435/JAAOS-D-13-00208.
- [36] M. J. Codsí *et al.*, “Normal glenoid vault anatomy and validation of a novel glenoid implant shape,” *J Shoulder Elbow Surg*, vol. 17, no. 3, pp. 471–478, May 2008, doi: 10.1016/j.jse.2007.08.010.
- [37] L. S. S. J. H. DT. Matsen FA, *Practical Evaluation and Management of the Shoulder*. Philadelphia, 1994.
- [38] H. I. Piponov *et al.*, “Glenoid version and size: does gender, ethnicity, or body size play a role?,” *Int Orthop*, vol. 40, no. 11, pp. 2347–2353, Nov. 2016, doi: 10.1007/S00264-016-3201-8.
- [39] Ü. Aygün, Y. Çalik, C. Işık, H. Şahin, R. Şahin, and D. Ö. Aygün, “The importance of glenoid version in patients with anterior dislocation of the shoulder,” *J Shoulder Elbow Surg*, vol. 25, no. 12, pp. 1930–1936, Dec. 2016, doi: 10.1016/J.JSE.2016.09.018.
- [40] L. Shi, J. F. Griffith, J. Huang, and D. Wang, “Excellent side-to-side symmetry in glenoid size and shape,” *Skeletal Radiol*, vol. 42, no. 12, pp. 1711–1715, Dec. 2013, doi: 10.1007/S00256-013-1728-Y.
- [41] S.-B. LEE, K.-J. KIM, S. W. O’DRISCOLL, B. F. MORREY, and K.-N. AN, “Dynamic Glenohumeral Stability Provided by the Rotator Cuff Muscles in the

- Mid-Range and End-Range of Motion,” *The Journal of Bone and Joint Surgery-American Volume*, vol. 82, no. 6, pp. 849–857, Jun. 2000, doi: 10.2106/00004623-200006000-00012.
- [42] D. C. Ackland *et al.*, “Muscle and Joint Function After Anatomic and Reverse Total Shoulder Arthroplasty Using a Modular Shoulder Prosthesis,” *Journal of Orthopaedic Research*, vol. 37, no. 9, pp. 1988–2003, Sep. 2019, doi: 10.1002/jor.24335.
- [43] V. T. Inman, J. B. dec M. Saunders, and L. C. Abbott, “Observations of the Function of the Shoulder Joint,” *Clin Orthop Relat Res*, vol. 330, pp. 3–12, Sep. 1996, doi: 10.1097/00003086-199609000-00002.
- [44] N. K. Poppen and P. S. Walker, “Forces at the glenohumeral joint in abduction,” *Clin Orthop Relat Res*, no. 135, pp. 165–70, Sep. 1978.
- [45] F. F. Buechel, M. J. Pappas, and A. F. DePalma, “Floating-socket? total shoulder replacement: Anatomical, biomechanical, and surgical rationale,” *J Biomed Mater Res*, vol. 12, no. 1, pp. 89–114, Jan. 1978, doi: 10.1002/jbm.820120109.
- [46] M. Post, M. Jablon, H. Miller, and M. Singh, “Constrained total shoulder joint replacement: a critical review,” *Clin Orthop Relat Res*, no. 144, pp. 135–50, Oct. 1979.
- [47] J. Dul, “A biomechanical model to quantify shoulder load at the work place,” *Clinical Biomechanics*, vol. 3, no. 3, pp. 124–128, Aug. 1988, doi: 10.1016/0268-0033(88)90057-5.
- [48] F. C. T. van der Helm, “Analysis of the kinematic and dynamic behavior of the shoulder mechanism,” *J Biomech*, vol. 27, no. 5, pp. 527–550, May 1994, doi: 10.1016/0021-9290(94)90064-7.
- [49] D. Karlsson and B. Peterson, “Towards a model for force predictions in the human shoulder,” *J Biomech*, vol. 25, no. 2, pp. 189–199, Feb. 1992, doi: 10.1016/0021-9290(92)90275-6.

- [50] F. C. T. van der Helm and H. E. J. Veeger, “Quasi-static analysis of muscle forces in the shoulder mechanism during wheelchair propulsion,” *J Biomech*, vol. 29, no. 1, pp. 39–52, Jan. 1996, doi: 10.1016/0021-9290(95)00026-7.
- [51] S. van Drongelen, L. H. van der Woude, T. W. Janssen, E. L. Angenot, E. K. Chadwick, and D. H. Veeger, “Glenohumeral Contact Forces and Muscle Forces Evaluated in Wheelchair-Related Activities of Daily Living in Able-Bodied Subjects Versus Subjects With Paraplegia and Tetraplegia,” *Arch Phys Med Rehabil*, vol. 86, no. 7, pp. 1434–1440, Jul. 2005, doi: 10.1016/j.apmr.2005.03.014.
- [52] D. Karlsson and B. Peterson, “Towards a model for force predictions in the human shoulder,” *J Biomech*, vol. 25, no. 2, pp. 189–199, Feb. 1992, doi: 10.1016/0021-9290(92)90275-6.
- [53] C. Anglin, U. P. Wyss, and D. R. Pichora, “Glenohumeral contact forces,” *Proc Inst Mech Eng H*, vol. 214, no. 6, pp. 637–644, Jun. 2000, doi: 10.1243/0954411001535660.
- [54] C. Klemm *et al.*, “Analysis of shoulder compressive and shear forces during functional activities of daily life,” *Clinical Biomechanics*, vol. 54, pp. 34–41, May 2018, doi: 10.1016/J.CLINBIOMECH.2018.03.006.
- [55] T. S. Gross, K. J. McLeod, and C. T. Rubin, “Characterizing bone strain distributions in vivo using three triple rosette strain gages,” *J Biomech*, vol. 25, no. 9, pp. 1081–1087, Sep. 1992, doi: 10.1016/0021-9290(92)90044-2.
- [56] E. F. Rybicki, E. J. Mills, A. S. Turner, and F. A. Simonen, “In vivo and analytical studies of forces and moments in equine long bones,” *J Biomech*, vol. 10, no. 11–12, pp. 701–705, Jan. 1977, doi: 10.1016/0021-9290(77)90085-9.
- [57] A. Marter *et al.*, “Measurement of Internal Implantation Strains in Analogue Bone Using DVC,” *Materials*, vol. 13, no. 18, p. 4050, Sep. 2020, doi: 10.3390/ma13184050.

- [58] R. Ghosh, S. Gupta, A. Dickinson, and M. Browne, “VERIFICATION OF THE DIGITAL IMAGE CORRELATION TECHNIQUE FOR BONE SURFACE STRAIN MEASUREMENTS,” *J Biomech*, vol. 45, p. S277, Jul. 2012, doi: 10.1016/S0021-9290(12)70278-6.
- [59] E. Dall’Ara, M. Peña-Fernández, M. Palanca, M. Giorgi, L. Cristofolini, and G. Tozzi, “Precision of Digital Volume Correlation Approaches for Strain Analysis in Bone Imaged with Micro-Computed Tomography at Different Dimensional Levels,” *Front Mater*, vol. 4, Nov. 2017, doi: 10.3389/fmats.2017.00031.
- [60] J. Hsieh, *Computed Tomography, Second Edition*. 1000 20th Street, Bellingham, WA 98227-0010 USA: SPIE, 2009. doi: 10.1117/3.817303.
- [61] W. P. Barrett, J. L. Franklin, S. E. Jackins, C. R. Wyss, and F. A. Matsen, “Total shoulder arthroplasty.,” *J Bone Joint Surg Am*, vol. 69, no. 6, pp. 865–72, Jul. 1987.
- [62] “What You Need To Know About Shoulder Replacement | Colten Luedke, DO, Sports Medicine & Orthopaedic Surgeon, Bryan, TX.”
<https://www.bcsorthopedics.com/blog/what-you-need-to-know-about-shoulder-replacement-24133.html> (accessed Aug. 10, 2022).
- [63] R. H. Cofield, “Total shoulder arthroplasty with the Neer prosthesis.,” *J Bone Joint Surg*, vol. 66, no. 6, pp. 899–906, Jul. 1984, doi: 10.2106/00004623-198466060-00010.
- [64] M. A. Wirth and C. A. Rockwood, “Complications of shoulder arthroplasty.,” *Clin Orthop Relat Res*, no. 307, pp. 47–69, Oct. 1994.
- [65] M. A. WIRTH and C. A. ROCKWOOD, “Current Concepts Review - Complications of Total Shoulder-Replacement Arthroplasty*,” *J Bone Joint Surg*, vol. 78, no. 4, pp. 603–16, Apr. 1996, doi: 10.2106/00004623-199604000-00018.

- [66] R. Barco, O. D. Savvidou, J. W. Sperling, J. Sanchez-Sotelo, and R. H. Cofield, "Complications in reverse shoulder arthroplasty," *EFORT Open Rev*, vol. 1, no. 3, p. 72, Mar. 2016, doi: 10.1302/2058-5241.1.160003.
- [67] J.-F. Gonzalez, G. B. Alami, F. Baque, G. Walch, and P. Boileau, "Complications of unconstrained shoulder prostheses," *J Shoulder Elbow Surg*, vol. 20, no. 4, pp. 666–682, Jun. 2011, doi: 10.1016/j.jse.2010.11.017.
- [68] P.-H. Flurin, M. Janout, C. P. Roche, T. W. Wright, and J. Zuckerman, "Revision of the loose glenoid component in anatomic total shoulder arthroplasty.," *Bull Hosp Jt Dis (2013)*, vol. 71 Suppl 2, pp. 68–76, 2013.
- [69] P. Goetti, P. J. Denard, P. Collin, M. Ibrahim, A. Mazzolari, and A. Läderrmann, "Biomechanics of anatomic and reverse shoulder arthroplasty," *EFORT Open Rev*, vol. 6, no. 10, pp. 918–931, Oct. 2021, doi: 10.1302/2058-5241.6.210014.
- [70] C. M. Jobe and J. P. Lannotti, "Limits imposed on glenohumeral motion by joint geometry," *J Shoulder Elbow Surg*, vol. 4, no. 4, pp. 281–285, Jul. 1995, doi: 10.1016/S1058-2746(05)80021-7.
- [71] A. R. KARDUNA, G. R. WILLIAMS, J. L. WILLIAMS, and J. P. IANNOTTI, "Glenohumeral Joint Translations before and after Total Shoulder Arthroplasty. A Study in Cadavera*," *J Bone Joint Surg*, vol. 79, no. 8, pp. 1166–74, Aug. 1997, doi: 10.2106/00004623-199708000-00008.
- [72] D. Collins, A. Tencer, J. Sidles, and F. Matsen, "Edge displacement and deformation of glenoid components in response to eccentric loading. The effect of preparation of the glenoid bone.," *J Bone Joint Surg Am*, vol. 74, no. 4, pp. 501–7, Apr. 1992.
- [73] C. Anglin, U. P. Wyss, R. W. Nyffeler, and C. Gerber, "Loosening performance of cemented glenoid prosthesis design pairs," *Clinical Biomechanics*, vol. 16, no. 2, pp. 144–150, Feb. 2001, doi: 10.1016/S0268-0033(00)00078-4.

- [74] A. Welsher *et al.*, “A comparison of pegged vs. keeled glenoid components regarding functional and radiographic outcomes in anatomic total shoulder arthroplasty: a systematic review and meta-analysis,” *JSES Open Access*, vol. 3, no. 3, pp. 136-144.e1, Oct. 2019, doi: 10.1016/J.JSES.2019.04.002.
- [75] D. Lacroix, L. A. Murphy, and P. J. Prendergast, “Three-Dimensional Finite Element Analysis of Glenoid Replacement Prostheses: A Comparison of Keeled and Pegged Anchorage Systems,” *J Biomech Eng*, vol. 122, no. 4, pp. 430–436, Aug. 2000, doi: 10.1115/1.1286318.
- [76] M. A. Wirth, D. L. Korvick, C. J. Basamania, F. Toro, T. B. Aufdemorte, and C. A. Rockwood, “Radiologic, mechanical, and histologic evaluation of 2 glenoid prosthesis designs in a canine model,” *J Shoulder Elbow Surg*, vol. 10, no. 2, pp. 140–148, Mar. 2001, doi: 10.1067/mse.2001.112021.
- [77] M. D. Lazarus, K. L. Jensen, C. Southworth, and F. A. Matsen, “The Radiographic Evaluation of Keeled and Pegged Glenoid Component Insertion,” *J Bone Joint Surg*, vol. 84, no. 7, pp. 1174–1182, Jul. 2002, doi: 10.2106/00004623-200207000-00013.
- [78] N. J. Giori, G. S. Beaupré, and D. R. Carter, “The influence of fixation peg design on the shear stability of prosthetic implants,” *Journal of Orthopaedic Research*, vol. 8, no. 6, pp. 892–898, Nov. 1990, doi: 10.1002/jor.1100080615.
- [79] G. R. Williams and J. A. Abboud, “Total shoulder arthroplasty: Glenoid component design,” *J Shoulder Elbow Surg*, vol. 14, no. 1, pp. S122–S128, Jan. 2005, doi: 10.1016/J.JSE.2004.09.028.
- [80] T. I. A. and N. D., “The results of shoulder arthroplasty in patients with rheumatoid arthritis,” <https://doi.org/10.1302/0301-620X.84B8.0841121>, vol. 84-B, no. 8, pp. 1121–1125, Nov. 2002, doi: 10.1302/0301-620X.84B8.0841121.
- [81] G. M. Gartsman, H. A. Elkousy, K. M. Warnock, T. B. Edwards, and D. P. O’Connor, “Radiographic comparison of pegged and keeled glenoid components,”

- J Shoulder Elbow Surg*, vol. 14, no. 3, pp. 252–257, May 2005, doi: 10.1016/J.JSE.2004.09.006.
- [82] T. C. Gascoyne *et al.*, “Radiostereometric analysis of keeled versus pegged glenoid components in total shoulder arthroplasty: a randomized feasibility study,” *Canadian Journal of Surgery*, vol. 60, no. 4, pp. 273–279, Aug. 2017, doi: 10.1503/cjs.001817.
- [83] M. P. Noyes, B. Meccia, and E. E. Spencer, “Five- to ten-year follow-up with a partially cemented all-polyethylene bone-ingrowth glenoid component,” *J Shoulder Elbow Surg*, vol. 24, no. 9, pp. 1458–1462, Sep. 2015, doi: 10.1016/j.jse.2015.02.018.
- [84] R. M. Arnold, R. R. High, K. T. Grosshans, C. W. Walker, and E. v. Fehring, “Bone presence between the central peg’s radial fins of a partially cemented pegged all poly glenoid component suggest few radiolucencies,” *J Shoulder Elbow Surg*, vol. 20, no. 2, pp. 315–321, Mar. 2011, doi: 10.1016/j.jse.2010.05.025.
- [85] R. H. Cofield, “Uncemented total shoulder arthroplasty. A review.,” *Clin Orthop Relat Res*, no. 307, pp. 86–93, Oct. 1994.
- [86] B. M. Crites and M. E. Berend, “Metal-backed patellar components: a brief report on 10-year survival.,” *Clin Orthop Relat Res*, no. 388, pp. 103–4, Jul. 2001.
- [87] J. W. Sperling, R. H. Cofield, S. W. O’Driscoll, M. E. Torchia, and C. M. Rowland, “Radiographic assessment of ingrowth total shoulder arthroplasty.,” *J Shoulder Elbow Surg*, vol. 9, no. 6, pp. 507–13, doi: 10.1067/mse.2000.109384.
- [88] L. A. Broström, R. Wallensten, E. Olsson, and D. Anderson, “The Kessel prosthesis in total shoulder arthroplasty. A five-year experience.,” *Clin Orthop Relat Res*, no. 277, pp. 155–60, Apr. 1992.
- [89] J. Brems, “The glenoid component in total shoulder arthroplasty,” *J Shoulder Elbow Surg*, vol. 2, no. 1, pp. 47–54, Jan. 1993, doi: 10.1016/S1058-2746(09)80138-9.

- [90] P. Boileau and G. Walch, “Normal and Pathological Anatomy of the Glenoid: Effects on the Design, Preparation, and Fixation of the Glenoid Component,” *Shoulder Arthroplasty*, pp. 127–140, 1999, doi: 10.1007/978-3-642-58365-0_13.
- [91] “Inset Glenoid Technology: A Paradigm Shift in Shoulder Replacement Surgery | Published in Journal of Orthopaedic Experience & Innovation.” <https://journaloei.scholasticahq.com/article/13447-inset-glenoid-technology-a-paradigm-shift-in-shoulder-replacement-surgery> (accessed Aug. 07, 2022).
- [92] J. R. Gagliano, S. M. Helms, G. P. Colbath, B. T. Przestrzelski, R. J. Hawkins, and J. D. DesJardins, “A comparison of onlay versus inlay glenoid component loosening in total shoulder arthroplasty,” *J Shoulder Elbow Surg*, vol. 26, no. 7, pp. 1113–1120, Jul. 2017, doi: 10.1016/J.JSE.2017.01.018.
- [93] J. Uribe, L. Vargas, and J. Zvijac, “Minimum 2 Years Outcomes of Powerlifters and Bodybuilders with advanced Glenohumeral arthritis, managed with Stemless aspherical humeral head resurfacing and inlay glenoid;,” <https://doi.org/10.1177/2325967120S00417>, vol. 8, no. 7_suppl6, p. 2325967120S0041, Jul. 2020, doi: 10.1177/2325967120S00417.
- [94] G. L. Cvetanovich, A. J. Naylor, M. C. O’Brien, B. R. Waterman, G. H. Garcia, and G. P. Nicholson, “Anatomic total shoulder arthroplasty with an inlay glenoid component: clinical outcomes and return to activity,” *J Shoulder Elbow Surg*, vol. 29, no. 6, pp. 1188–1196, Jun. 2020, doi: 10.1016/J.JSE.2019.10.003.
- [95] G. Walch, R. Badet, A. Boulahia, and A. Khoury, “Morphologic study of the Glenoid in primary glenohumeral osteoarthritis,” *J Arthroplasty*, vol. 14, no. 6, pp. 756–760, Sep. 1999, doi: 10.1016/S0883-5403(99)90232-2.
- [96] J. P. Iannotti, B.-J. Jun, T. E. Patterson, and E. T. Ricchetti, “Quantitative Measurement of Osseous Pathology in Advanced Glenohumeral Osteoarthritis,” *Journal of Bone and Joint Surgery*, vol. 99, no. 17, pp. 1460–1468, Sep. 2017, doi: 10.2106/JBJS.16.00869.

- [97] M. J. Bercik, K. Kruse, M. Yalozis, M.-O. Gauci, J. Chaoui, and G. Walch, “A modification to the Walch classification of the glenoid in primary glenohumeral osteoarthritis using three-dimensional imaging,” *J Shoulder Elbow Surg*, vol. 25, no. 10, pp. 1601–1606, Oct. 2016, doi: 10.1016/j.jse.2016.03.010.
- [98] S. Gates, B. Sager, and M. Khazzam, “Preoperative glenoid considerations for shoulder arthroplasty: a review,” *EFORT Open Rev*, vol. 5, no. 3, pp. 126–137, Mar. 2020, doi: 10.1302/2058-5241.5.190011.
- [99] F. A. Matsen, J. Clinton, J. Lynch, A. Bertelsen, and M. L. Richardson, “Glenoid Component Failure in Total Shoulder Arthroplasty,” *This is an enhanced PDF from The Journal of Bone and Joint Surgery*, vol. 90, pp. 885–896, 2008, doi: 10.2106/JBJS.G.01263.
- [100] M. W. Rodosky and L. U. Bigliani, “Indications for glenoid resurfacing in shoulder arthroplasty,” *J Shoulder Elbow Surg*, vol. 5, no. 3, pp. 231–248, May 1996, doi: 10.1016/S1058-2746(05)80013-8.
- [101] B. C. Brenner, D. C. Ferlic, M. L. Clayton, and D. A. Dennis, “Survivorship of unconstrained total shoulder arthroplasty,” *J Bone Joint Surg Am*, vol. 71, no. 9, pp. 1289–96, Oct. 1989.
- [102] R. J. Hawkins, R. H. Bell, and B. Jallay, “Total shoulder arthroplasty,” *Clin Orthop Relat Res*, no. 242, pp. 188–94, May 1989.
- [103] C. S. Neer, K. C. Watson, and F. J. Stanton, “Recent experience in total shoulder replacement,” *J Bone Joint Surg Am*, vol. 64, no. 3, pp. 319–37, Mar. 1982.
- [104] A. Papadonikolakis, M. B. Neralilek, and F. A. Matsen, “Failure of the Glenoid Component in Anatomic Total Shoulder Arthroplasty,” *J Bone Joint Surg*, vol. 95, no. 24, pp. 2205–2212, Dec. 2013, doi: 10.2106/JBJS.L.00552.
- [105] J. L. Franklin, W. P. Barrett, S. E. Jackins, and F. A. Matsen, “Glenoid loosening in total shoulder arthroplasty,” *J Arthroplasty*, vol. 3, no. 1, pp. 39–46, 1988, doi: 10.1016/S0883-5403(88)80051-2.

- [106] M. E. Torchia, R. H. Cofield, and C. R. Settergren, "Total shoulder arthroplasty with the neer prosthesis: Long-term results," *J Shoulder Elbow Surg*, vol. 6, no. 6, pp. 495–505, Nov. 1997, doi: 10.1016/S1058-2746(97)90081-1.
- [107] O. Sneppen, S. Fruensgaard, H. v. Johannsen, B. S. Olsen, J. O. Sjøbjerg, and N. H. Andersen, "Total shoulder replacement in rheumatoid arthritis: Proximal migration and loosening," *J Shoulder Elbow Surg*, vol. 5, no. 1, pp. 47–52, Jan. 1996, doi: 10.1016/S1058-2746(96)80030-9.
- [108] D. T. Harryman, J. A. Sidles, S. L. Harris, S. B. Lippitt, and F. A. Matsen, "The effect of articular conformity and the size of the humeral head component on laxity and motion after glenohumeral arthroplasty. A study in cadavera.," *J Bone Joint Surg*, vol. 77, no. 4, pp. 555–563, Apr. 1995, doi: 10.2106/00004623-199504000-00008.
- [109] M. A. Wirth, D. L. Korvick, C. J. Basamania, F. Toro, T. B. Aufdemorte, and C. A. Rockwood, "Radiologic, mechanical, and histologic evaluation of 2 glenoid prosthesis designs in a canine model," *J Shoulder Elbow Surg*, vol. 10, no. 2, pp. 140–148, Mar. 2001, doi: 10.1067/mse.2001.112021.
- [110] C. Anglin, U. P. Wyss, R. W. Nyffeler, and C. Gerber, "Loosening performance of cemented glenoid prosthesis design pairs," *Clinical Biomechanics*, vol. 16, no. 2, pp. 144–150, Feb. 2001, doi: 10.1016/S0268-0033(00)00078-4.
- [111] G. WALCH, T. B. EDWARDS, A. BOULAHIA, P. BOILEAU, D. MOLÉ, and P. ADELEINE, "THE INFLUENCE OF GLENOHUMERAL PROSTHETIC MISMATCH ON GLENOID RADIOLUCENT LINES," *The Journal of Bone and Joint Surgery-American Volume*, vol. 84, no. 12, pp. 2186–2191, Dec. 2002, doi: 10.2106/00004623-200212000-00010.
- [112] C. Anglin, U. P. Wyss, and D. R. Pichora, "Mechanical testing of shoulder prostheses and recommendations for glenoid design," *J Shoulder Elbow Surg*, vol. 9, no. 4, pp. 323–331, Jul. 2000, doi: 10.1067/mse.2000.105451.

- [113] B. Couteau, P. Mansat, É. Estivalèzes, R. Darmana, M. Mansat, and J. Egan, “Finite element analysis of the mechanical behavior of a scapula implanted with a glenoid prosthesis,” *Clinical Biomechanics*, vol. 16, no. 7, pp. 566–575, Aug. 2001, doi: 10.1016/S0268-0033(01)00029-8.
- [114] A. R. Karduna, G. R. Williams, J. P. Iannotti, and J. L. Williams, “Total Shoulder Arthroplasty Biomechanics: A Study of the Forces and Strains at the Glenoid Component,” *J Biomech Eng*, vol. 120, no. 1, pp. 92–99, Feb. 1998, doi: 10.1115/1.2834312.
- [115] R. Severt, B. J. Thomas, M. J. Tsenter, H. C. Amstutz, and J. M. Kabo, “The influence of conformity and constraint on translational forces and frictional torque in total shoulder arthroplasty,” *Clin Orthop Relat Res*, no. 292, pp. 151–8, Jul. 1993.
- [116] A. Terrier, P. Büchler, and A. Farron, “Influence of glenohumeral conformity on glenoid stresses after total shoulder arthroplasty,” *J Shoulder Elbow Surg*, vol. 15, no. 4, pp. 515–520, Jul. 2006, doi: 10.1016/j.jse.2005.09.021.
- [117] S. J. Nho *et al.*, “Comparison of conforming and nonconforming retrieved glenoid components,” *J Shoulder Elbow Surg*, vol. 17, no. 6, pp. 914–920, Nov. 2008, doi: 10.1016/j.jse.2008.04.010.
- [118] “Standard Test Methods for Dynamic Evaluation of Glenoid Loosening or Disassociation.” <https://www.astm.org/f2028-17.html> (accessed Jun. 08, 2022).
- [119] N. Rosenberg, M. Haddad, and D. Norm, “Glenoid Loosening in Total Shoulder Arthroplasty,” in *Arthroplasty - Update*, InTech, 2013. doi: 10.5772/53438.
- [120] Boyin Ding, R. M. Stanley, B. S. Cazzolato, and J. J. Costi, “Real-time FPGA control of a hexapod robot for 6-DOF biomechanical testing,” in *IECON 2011 - 37th Annual Conference of the IEEE Industrial Electronics Society*, Nov. 2011, pp. 252–257. doi: 10.1109/IECON.2011.6119320.

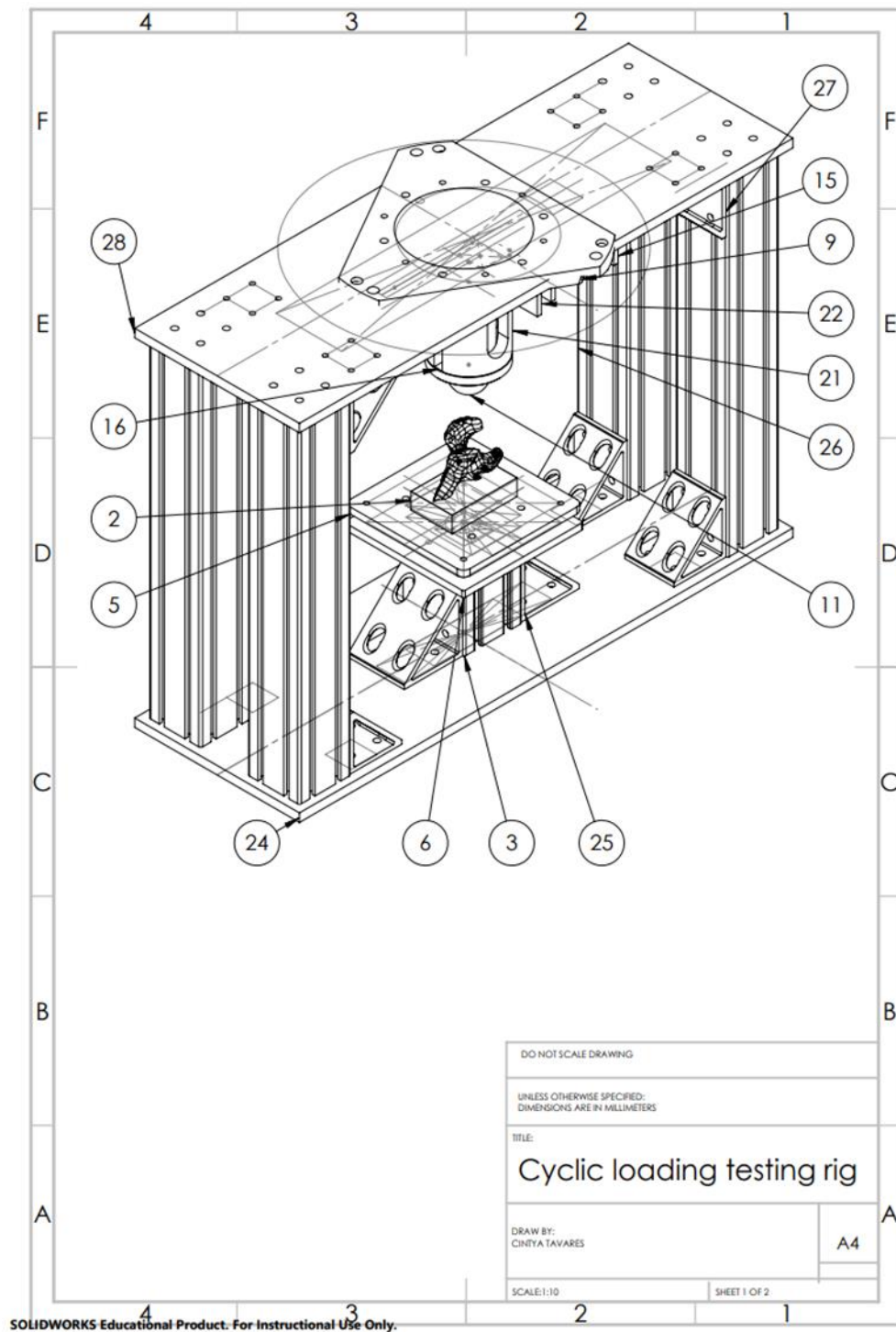
- [121] B. Dasgupta and T. S. Mruthyunjaya, “The Stewart platform manipulator: a review,” *Mech Mach Theory*, vol. 35, no. 1, pp. 15–40, Jan. 2000, doi: 10.1016/S0094-114X(99)00006-3.
- [122] J.-P. Merlet and C. Gosselin, “Parallel Mechanisms and Robots,” in *Springer Handbook of Robotics*, Berlin, Heidelberg: Springer Berlin Heidelberg, 2008, pp. 269–285. doi: 10.1007/978-3-540-30301-5_13.
- [123] M. R. Walker and J. P. Dickey, “New methodology for multi-dimensional spinal joint testing with a parallel robot,” *Med Biol Eng Comput*, vol. 45, no. 3, pp. 297–304, Feb. 2007, doi: 10.1007/s11517-006-0158-6.
- [124] I. A. Stokes, M. Gardner-Morse, D. Churchill, and J. P. Laible, “Measurement of a spinal motion segment stiffness matrix,” *J Biomech*, vol. 35, no. 4, pp. 517–521, Apr. 2002, doi: 10.1016/S0021-9290(01)00221-4.
- [125] “Standard Test Methods for Dynamic Evaluation of Glenoid Loosening or Disassociation.” <https://www.astm.org/f2028-17.html> (accessed Jun. 05, 2022).
- [126] B. S. Schoch *et al.*, “The effect of radial mismatch on radiographic glenoid loosening,” *JSES Open Access*, vol. 3, no. 4, pp. 287–291, Dec. 2019, doi: 10.1016/j.jses.2019.09.007.
- [127] N. K. Poppen and P. S. Walker, “Forces at the glenohumeral joint in abduction,” *Clin Orthop Relat Res*, no. 135, pp. 165–70, Sep. 1978.
- [128] M. Apreleva, I. M. Parsons, J. J. P. Warner, F. H. Fu, and S. L.-Y. Woo, “Experimental investigation of reaction forces at the glenohumeral joint during active abduction,” *J Shoulder Elbow Surg*, vol. 9, no. 5, pp. 409–417, Sep. 2000, doi: 10.1067/mse.2000.106321.
- [129] C. Smith, “Development of Force-Space Navigation for Surgical Robotics,” *Electronic Thesis and Dissertation Repository*, Jan. 2018, Accessed: Aug. 10, 2022. [Online]. Available: <https://ir.lib.uwo.ca/etd/5177>

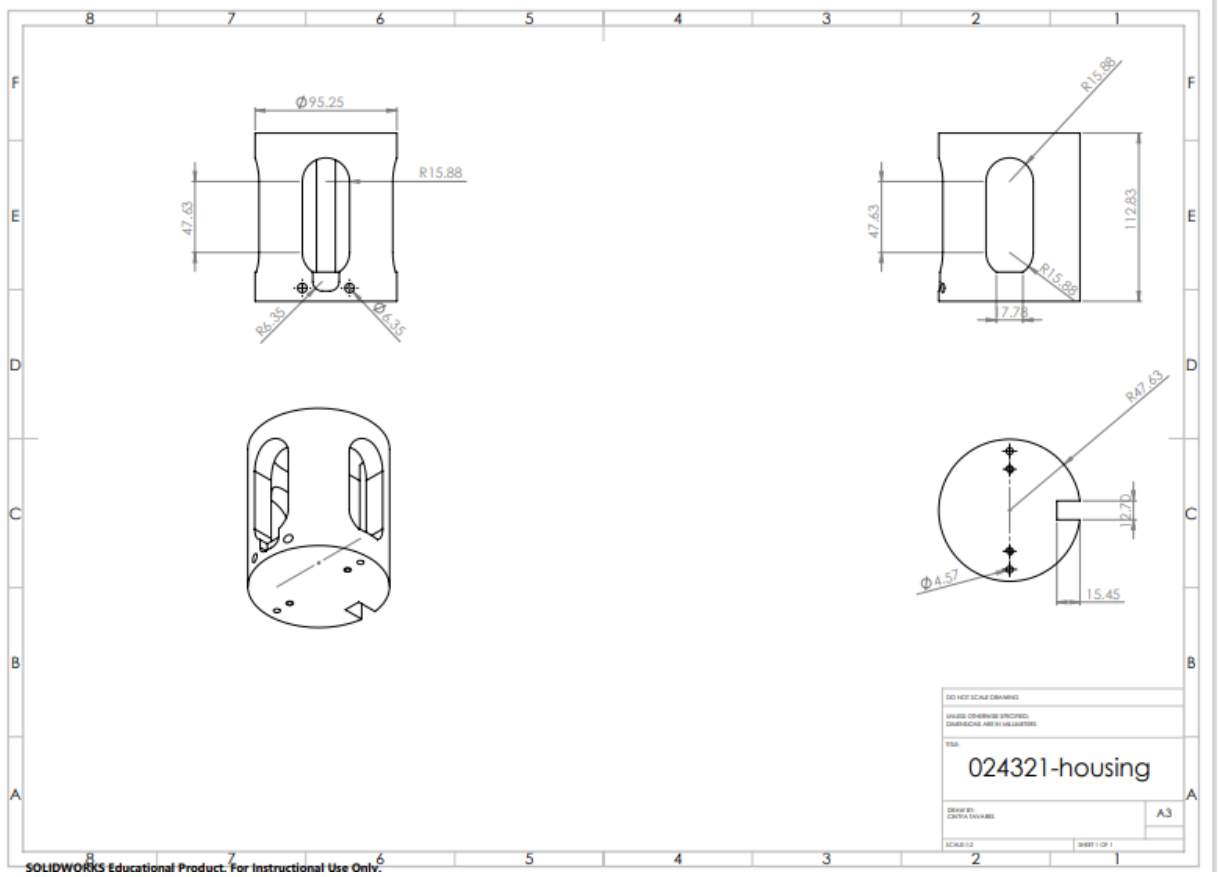
- [130] A. Terrier, P. Büchler, and A. Farron, “Bone–cement interface of the glenoid component: Stress analysis for varying cement thickness,” *Clinical Biomechanics*, vol. 20, no. 7, pp. 710–717, Aug. 2005, doi: 10.1016/j.clinbiomech.2005.03.010.
- [131] A. Terrier, V. Brighenti, D. P. Pioletti, and A. Farron, “Importance of polyethylene thickness in total shoulder arthroplasty: A finite element analysis,” *Clinical Biomechanics*, vol. 27, no. 5, pp. 443–448, Jun. 2012, doi: 10.1016/j.clinbiomech.2011.12.003.
- [132] T. B. Edwards, J. E. Labriola, R. J. Stanley, D. P. O’Connor, H. A. Elkousy, and G. M. Gartsman, “Radiographic comparison of pegged and keeled glenoid components using modern cementing techniques: A prospective randomized study,” *J Shoulder Elbow Surg*, vol. 19, no. 2, pp. 251–257, Mar. 2010, doi: 10.1016/j.jse.2009.10.013.
- [133] C. Yongpravat, H. M. Kim, T. R. Gardner, L. U. Bigliani, W. N. Levine, and C. S. Ahmad, “Glenoid implant orientation and cement failure in total shoulder arthroplasty: a finite element analysis,” *J Shoulder Elbow Surg*, vol. 22, no. 7, pp. 940–947, Jul. 2013, doi: 10.1016/j.jse.2012.09.007.
- [134] H. Rahme, P. Mattsson, L. Wikblad, J. Nowak, and S. Larsson, “Stability of Cemented in-Line Pegged Glenoid Compared with Keeled Glenoid Components in Total Shoulder Arthroplasty,” *The Journal of Bone and Joint Surgery-American Volume*, vol. 91, no. 8, pp. 1965–1972, Aug. 2009, doi: 10.2106/JBJS.H.00938.
- [135] A. Terrier, P. Büchler, and A. Farron, “Bone–cement interface of the glenoid component: Stress analysis for varying cement thickness,” *Clinical Biomechanics*, vol. 20, no. 7, pp. 710–717, Aug. 2005, doi: 10.1016/j.clinbiomech.2005.03.010.
- [136] D. Nuttall, J. F. Haines, and I. I. Trail, “A study of the micromovement of pegged and keeled glenoid components compared using radiostereometric analysis,” *J Shoulder Elbow Surg*, vol. 16, no. 3, pp. S65–S70, May 2007, doi: 10.1016/j.jse.2006.01.015.

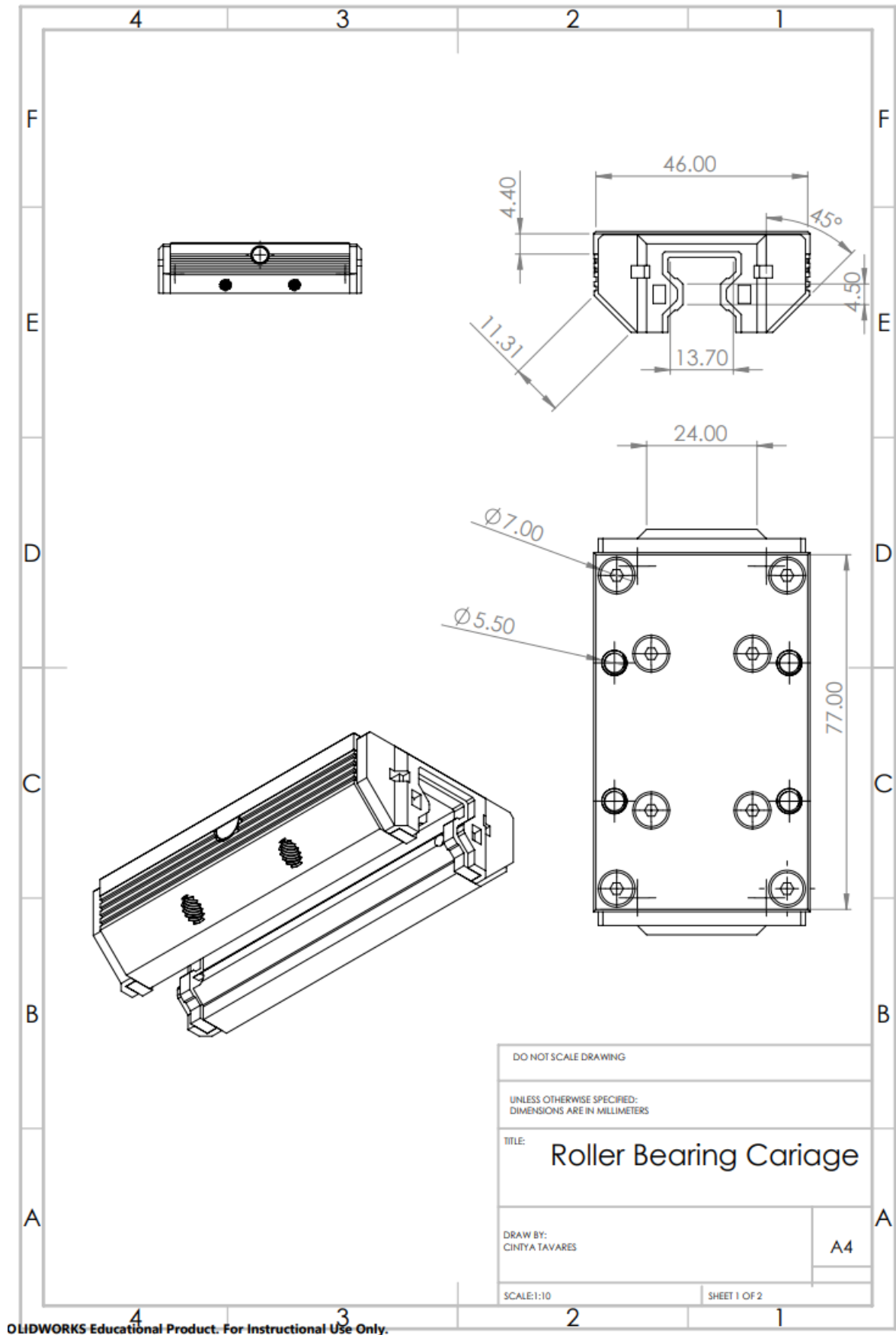
- [137] P. Mansat, J. Briot, M. Mansat, and P. Swider, "Evaluation of the glenoid implant survival using a biomechanical finite element analysis: Influence of the implant design, bone properties, and loading location," *J Shoulder Elbow Surg*, vol. 16, no. 3, pp. S79–S83, May 2007, doi: 10.1016/j.jse.2005.11.010.
- [138] D. Lacroix, L. A. Murphy, and P. J. Prendergast, "Three-Dimensional Finite Element Analysis of Glenoid Replacement Prostheses: A Comparison of Keeled and Pegged Anchorage Systems," *J Biomech Eng*, vol. 122, no. 4, pp. 430–436, Aug. 2000, doi: 10.1115/1.1286318.
- [139] C. Anglin, U. P. Wyss, R. W. Nyffeler, and C. Gerber, "Loosening performance of cemented glenoid prosthesis design pairs," *Clinical Biomechanics*, vol. 16, no. 2, pp. 144–150, Feb. 2001, doi: 10.1016/S0268-0033(00)00078-4.
- [140] A. H. Abdul Wahab, M. R. Abdul Kadir, T. Kamarul, M. N. Harun, and A. Syahrom, "Analysis on stress and micromotion on various peg fixation at glenoid implant," *Tribology - Materials, Surfaces & Interfaces*, vol. 10, no. 1, pp. 26–32, Jan. 2016, doi: 10.1080/17515831.2015.1125984.
- [141] D. Lacroix, L. A. Murphy, and P. J. Prendergast, "Three-Dimensional Finite Element Analysis of Glenoid Replacement Prostheses: A Comparison of Keeled and Pegged Anchorage Systems," *J Biomech Eng*, vol. 122, no. 4, pp. 430–436, Aug. 2000, doi: 10.1115/1.1286318.
- [142] N. J. Giori, G. S. Beaupré, and D. R. Carter, "The influence of fixation peg design on the shear stability of prosthetic implants," *Journal of Orthopaedic Research*, vol. 8, no. 6, pp. 892–898, Nov. 1990, doi: 10.1002/jor.1100080615.
- [143] C. Anglin, U. P. Wyss, R. W. Nyffeler, and C. Gerber, "Loosening performance of cemented glenoid prosthesis design pairs," *Clinical Biomechanics*, vol. 16, no. 2, pp. 144–150, Feb. 2001, doi: 10.1016/S0268-0033(00)00078-4.

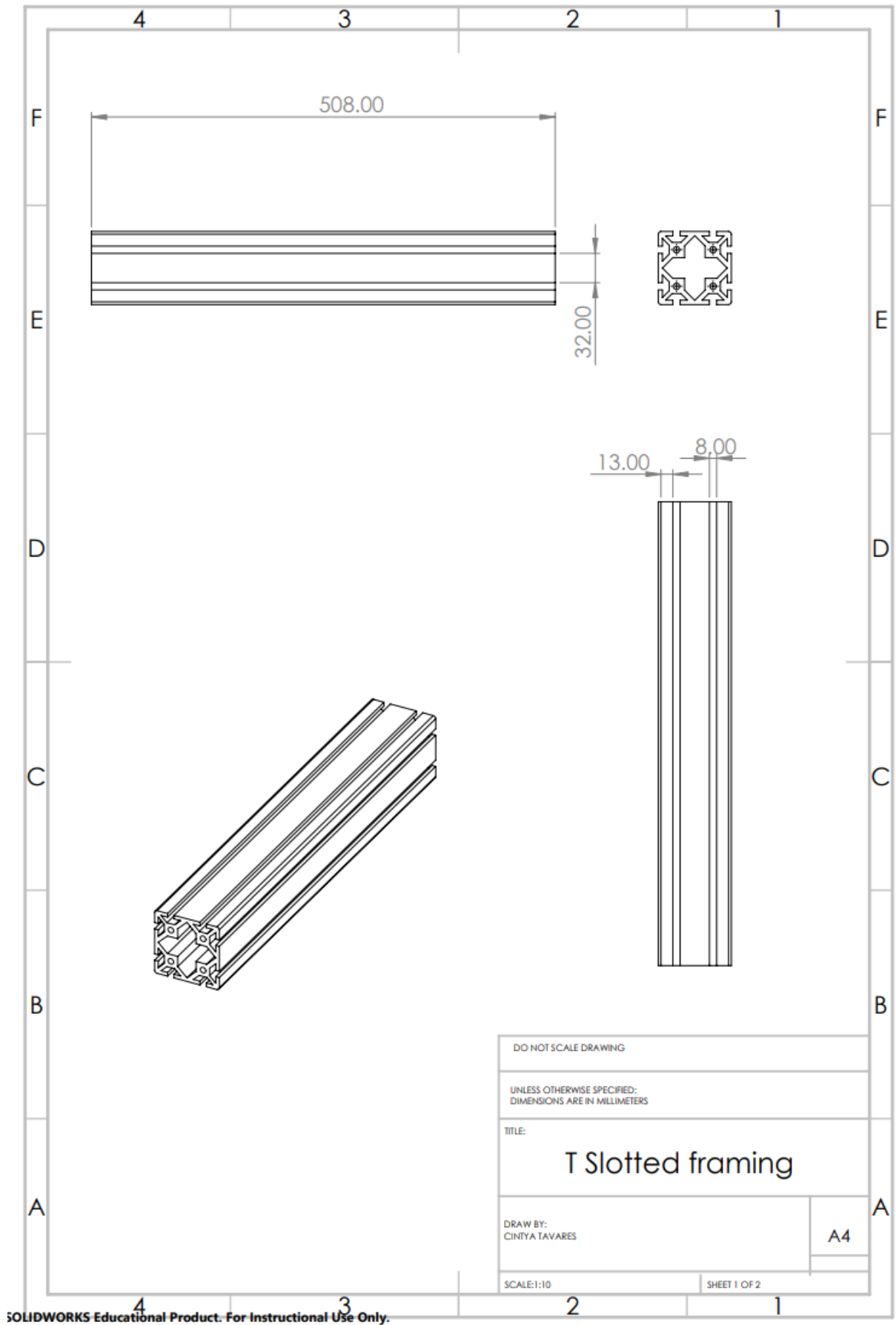
Appendix A: Developed Experimental Apparatus Component Drawings

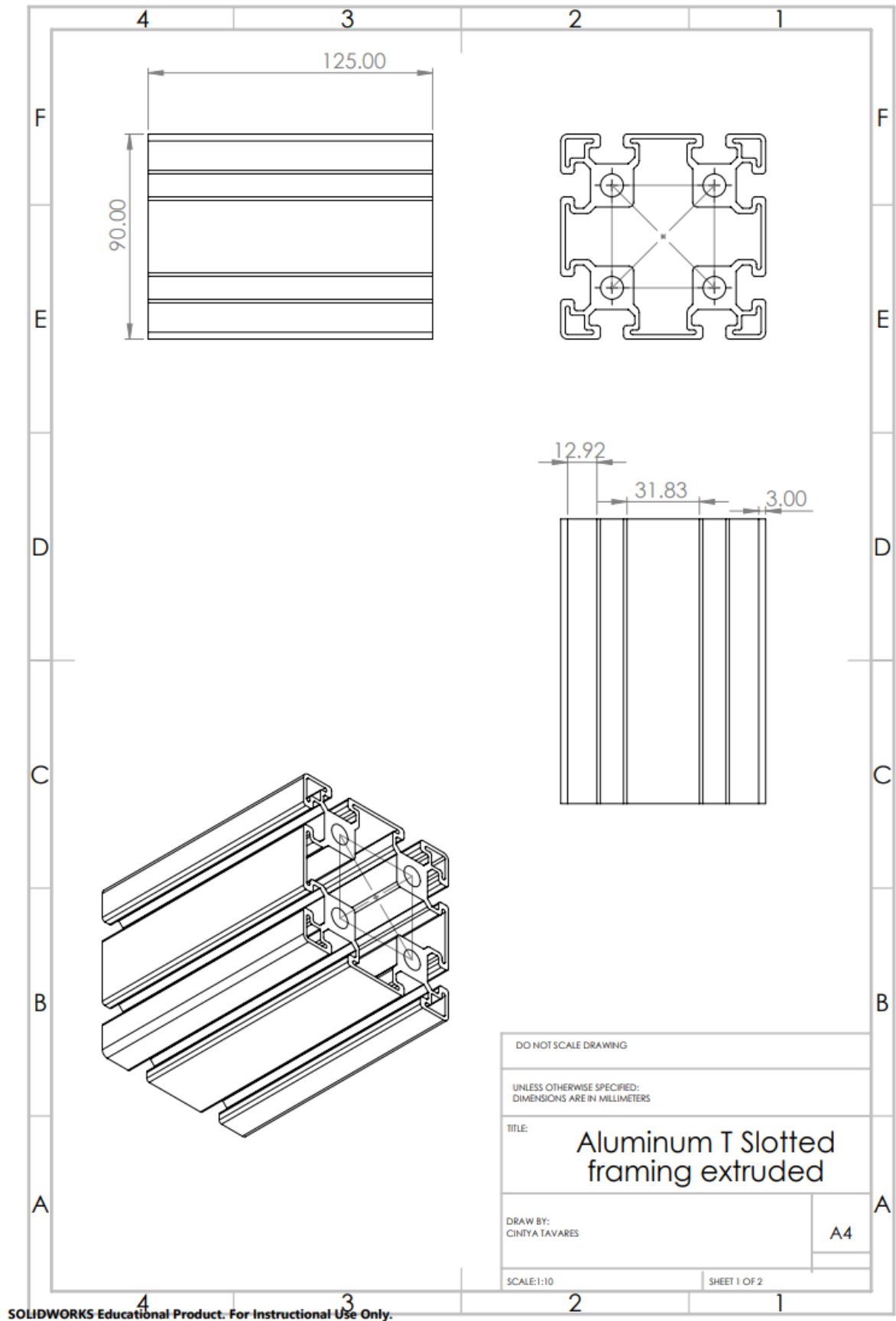
Note: All dimensions are in millimeters (mm).

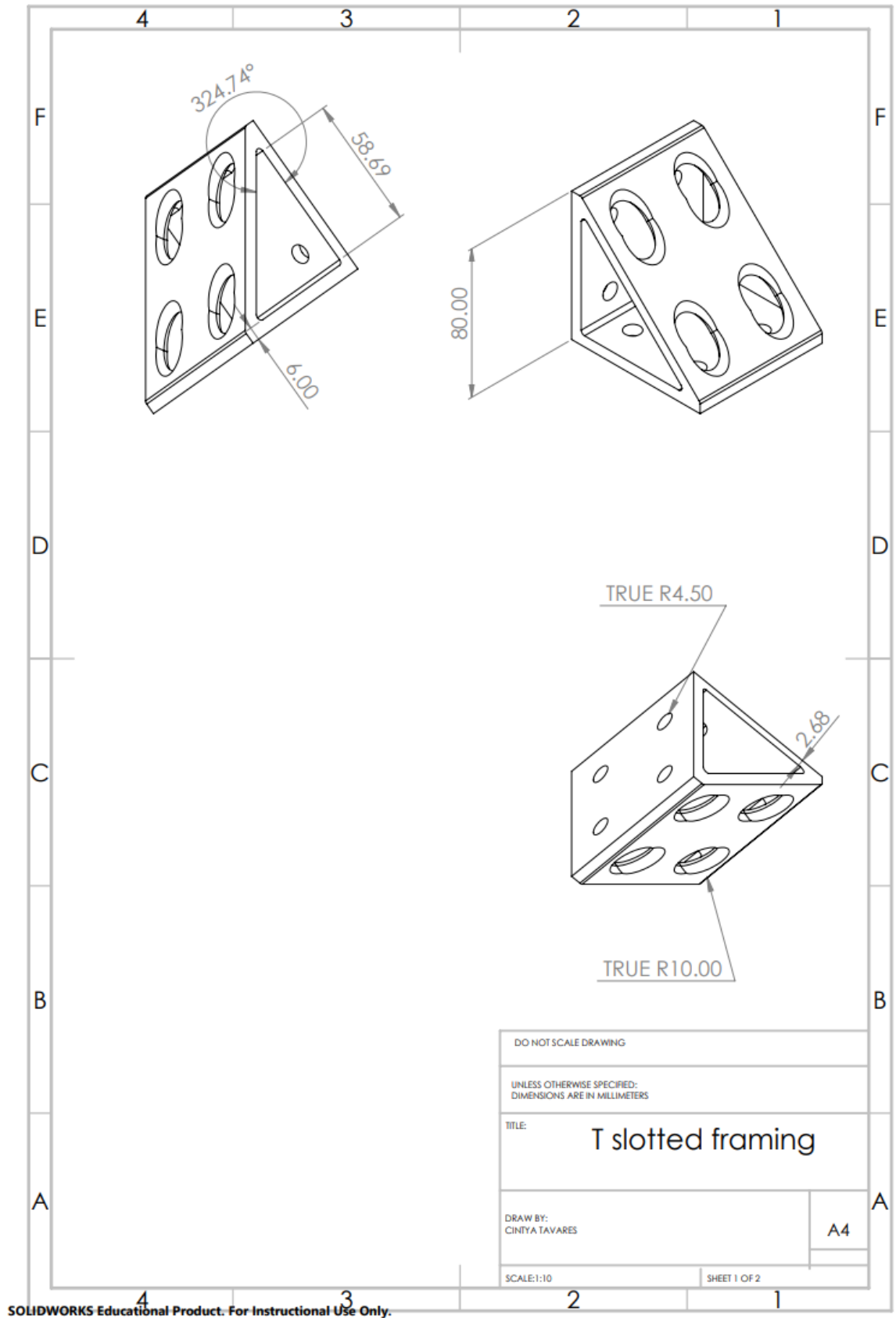




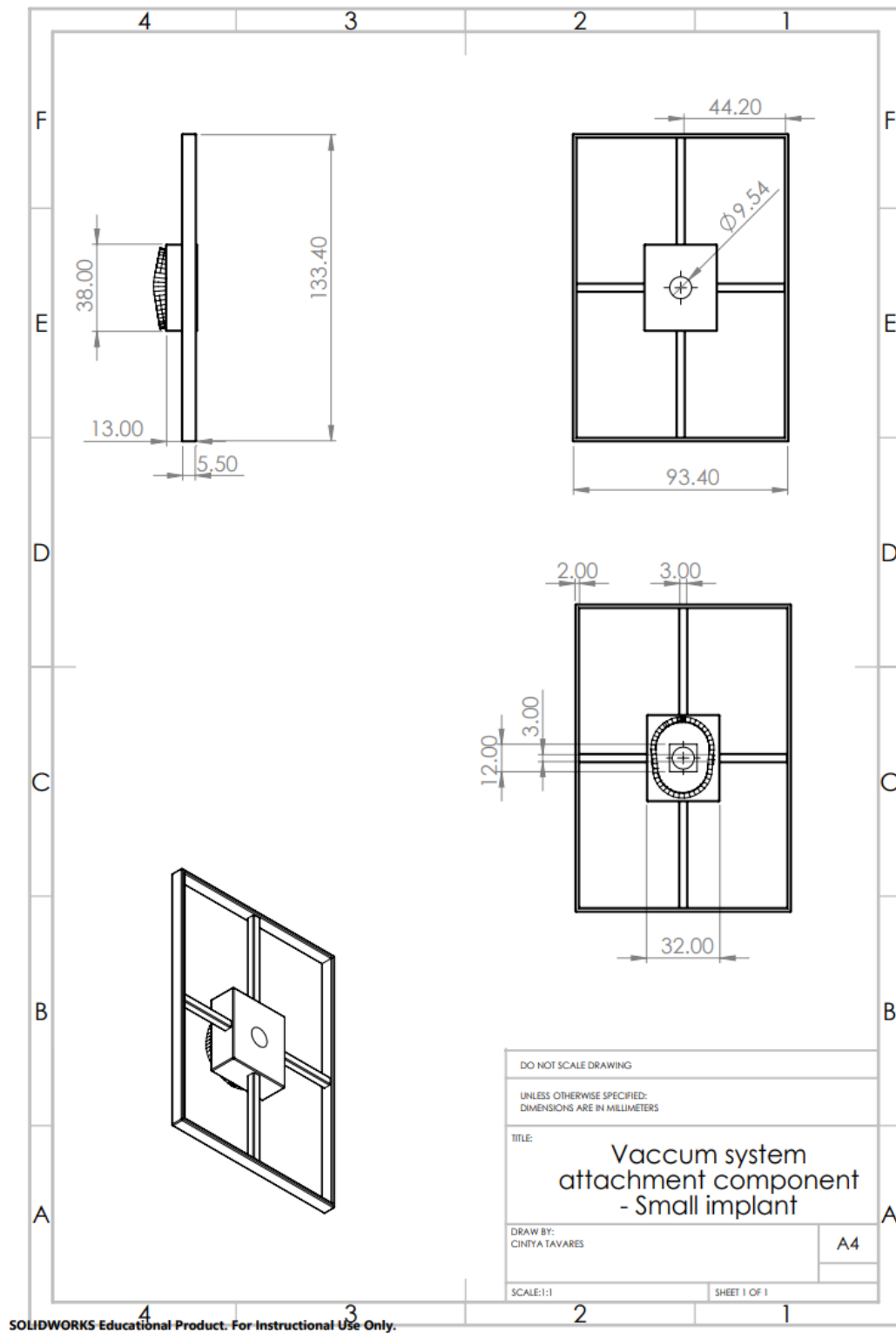


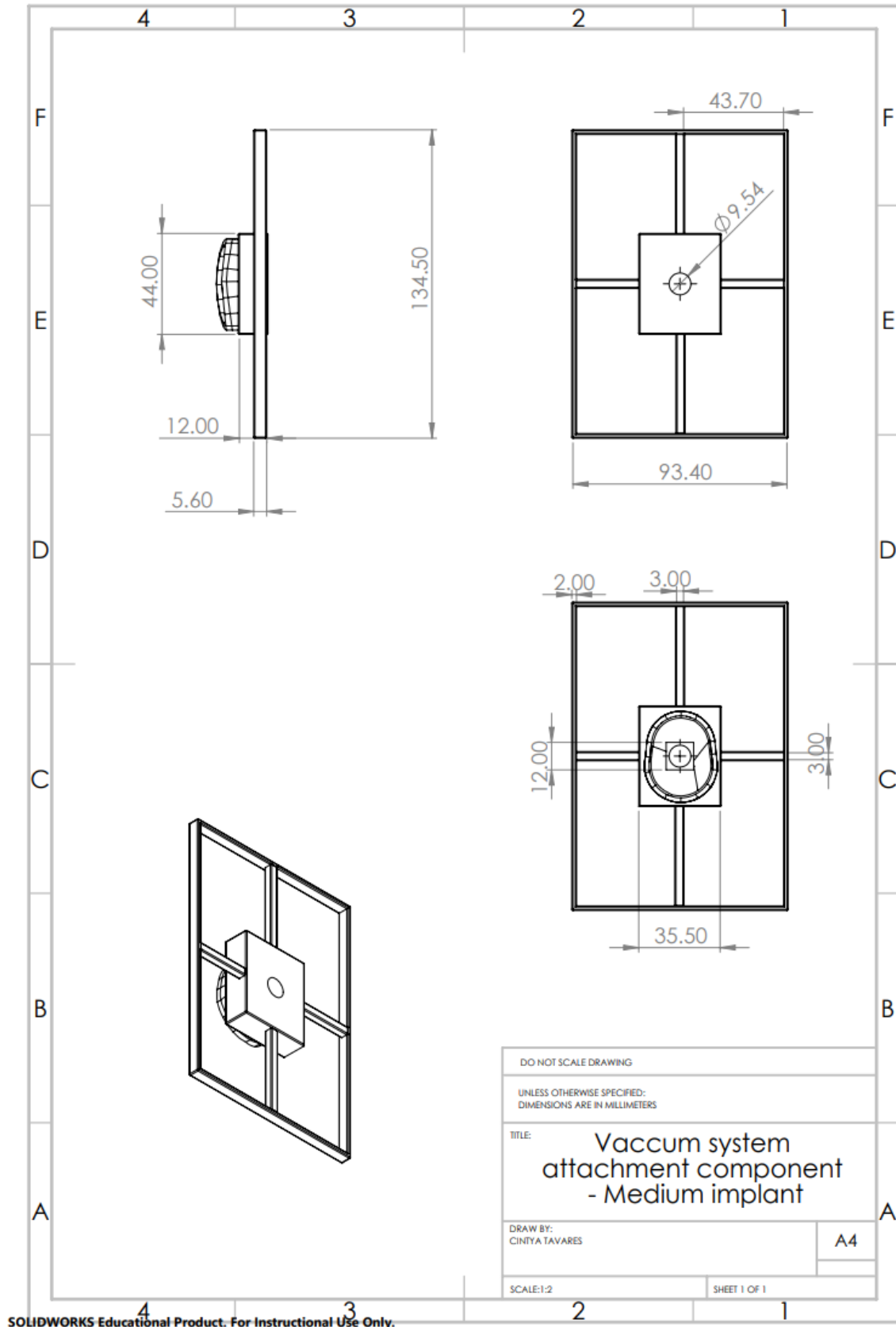


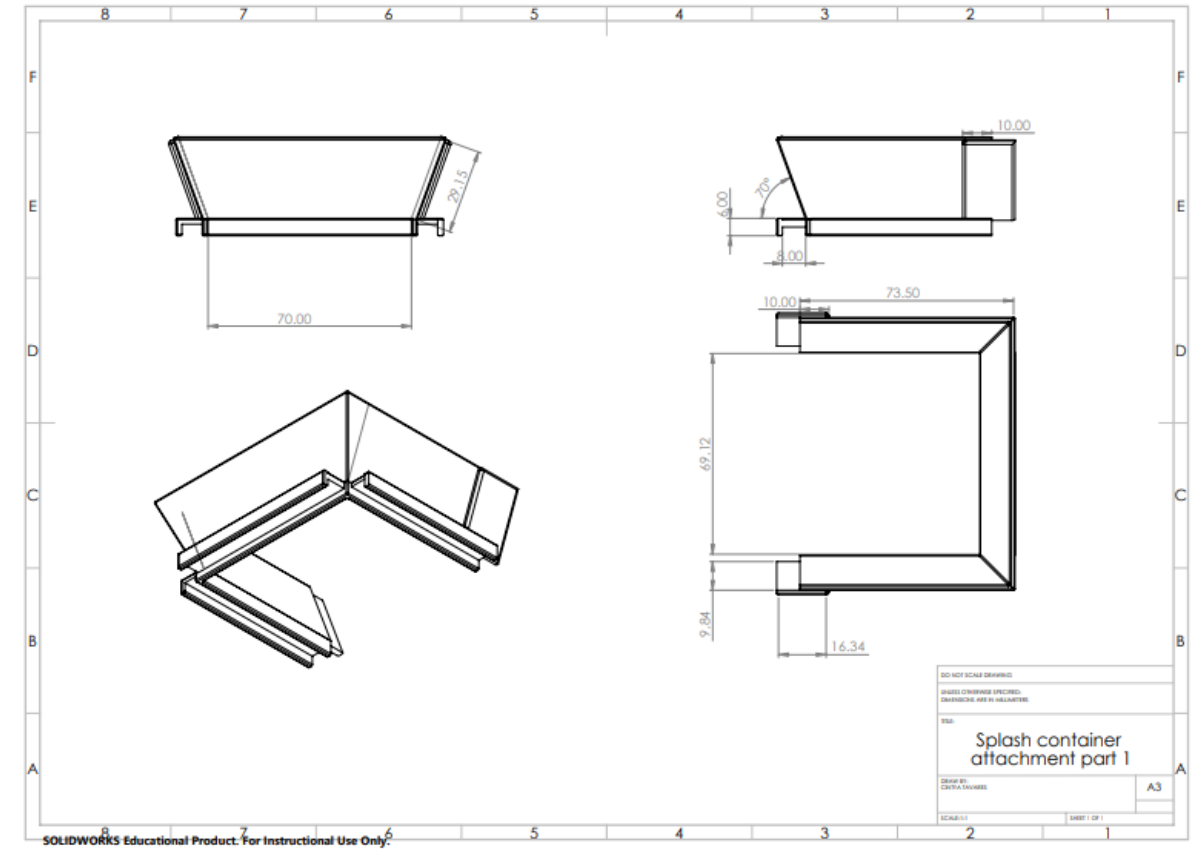


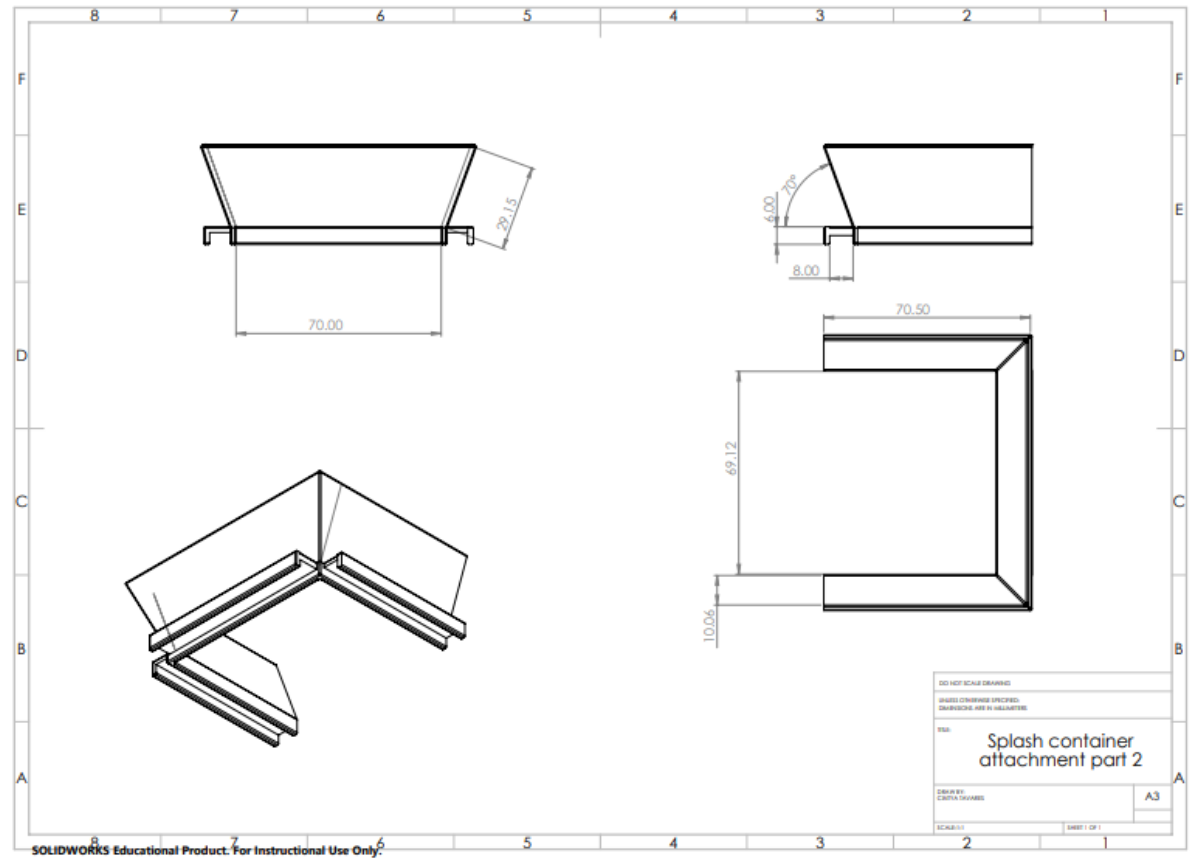


Appendix A1: Vacuum-system Attachment Components and Splash Component Parts Drawings









Appendix B: Supplementary Tables of the Test Results Presented in Chapters 3 and 4

Table. 1: Percent Error for the two Testing Apparatus- 300N Load Trial.

		<i>Rectangular Design</i>	<i>Triangular Design</i>	<i>Concave Design</i>
<i>Hexapod Apparatus (A)</i>		$F_Z = -269.146\text{N}$	$F_Z = -166.758\text{N}$	$F_Z = -239.580\text{N}$
<i>Cyclic Loading Simulator (B)</i>		$F_Z = -289.759\text{N}$	$F_Z = -239.673\text{N}$	$F_Z = -273.010\text{N}$
<i>% Error (F_Z)</i>	<i>(A)</i>	10.285%	44.414%	20.140%
<i>Target load (-300N)</i>	<i>(B)</i>	3.414%	20.109%	8.997%

((-) Denotes the negative position in the Z axis)

Table. 2: Percent Error for the two Testing Apparatus- 500N Load Trial.

		<i>Rectangular Design</i>	<i>Triangular Design</i>	<i>Concave Design</i>
<i>Hexapod Apparatus (A)</i>		$F_Z = -108.234\text{N}$	$F_Z = -369.234\text{N}$	$F_Z = -323.29\text{N}$
<i>Cyclic Loading Simulator (B)</i>		$F_Z = -426.422\text{N}$	$F_Z = -406.422\text{N}$	$F_Z = -483.012\text{N}$
<i>% Error (F_Z)</i>	<i>(A)</i>	78.353%	26.153%	35.342%
<i>Target load (-500N)</i>	<i>(B)</i>	14.716%	18.716%	3.398%

((-) Denotes the negative position in the Z axis)

Table. 3: Percent Error for the two Testing Apparatus- 700N Load Trial.

		<i>Rectangular Design</i>	<i>Triangular Design</i>	<i>Concave Design</i>
<i>Hexapod Apparatus (A)</i>		$F_Z = -623.885\text{N}$	$F_Z = -517.017\text{N}$	$F_Z = -534.48\text{N}$
<i>Cyclic Loading Simulator (B)</i>		$F_Z = -684.453\text{N}$	$F_Z = -631.214\text{N}$	$F_Z = -686.939\text{N}$
<i>% Error (F_Z)</i>	<i>(A)</i>	10.874%	26.140%	23.646%
<i>Target load (-700N)</i>	<i>(B)</i>	2.221%	9.826%	1.866%

((-) Denotes the negative position in the Z axis)

Table. 4: Maximum and Minimum Load values obtained using the Hexapod Model.

<i>Design</i>		<i>Applied load (300N)</i>	<i>Applied load (500N)</i>	<i>Applied load (700N)</i>
<i>Rectangular</i>	Min.	$F_Z = -236.329\text{N}$	$F_Z = -304.221\text{N}$	$F_Z = -587.229\text{N}$
	Max.	$F_Z = -340.294\text{N}$	$F_Z = -506.346\text{N}$	$F_Z = -675.141\text{N}$
<i>Triangular</i>	Min.	$F_Z = -24.032\text{N}$	$F_Z = -323.467\text{N}$	$F_Z = -474.943\text{N}$
	Max.	$F_Z = -323.345\text{N}$	$F_Z = -415.742\text{N}$	$F_Z = -544.567\text{N}$
<i>Concave</i>	Min.	$F_Z = -175.753\text{N}$	$F_Z = -123.076\text{N}$	$F_Z = -421.08\text{N}$
	Max.	$F_Z = -359.76\text{N}$	$F_Z = -547.278\text{N}$	$F_Z = -716.213\text{N}$

((-) Denotes the negative position in the Z axis)

Table. 5: Maximum and Minimum Load values obtained using the Cyclic Loading Simulator Model.

<i>Design</i>		<i>Applied load (300N)</i>	<i>Applied load (500N)</i>	<i>Applied load (700N)</i>
<i>Rectangular</i>	Min.	$F_Z = -259.477\text{N}$	$F_Z = -408.809\text{N}$	$F_Z = -587.229\text{N}$
	Max.	$F_Z = -330.172\text{N}$	$F_Z = -547.089\text{N}$	$F_Z = -718.715\text{N}$
<i>Triangular</i>	Min.	$F_Z = -13.156\text{N}$	$F_Z = -1.692\text{N}$	$F_Z = -474.943\text{N}$
	Max.	$F_Z = -310.906\text{N}$	$F_Z = -506.012\text{N}$	$F_Z = -610.441\text{N}$
<i>Concave</i>	Min.	$F_Z = -202.278\text{N}$	$F_Z = -450.114\text{N}$	$F_Z = -656.947\text{N}$
	Max.	$F_Z = -335.033\text{N}$	$F_Z = -510.092\text{N}$	$F_Z = -719.435\text{N}$

((-) Denotes the negative position in the Z axis)

Appendix C: Experimental Apparatus Pilot Test Results Plots and Tables

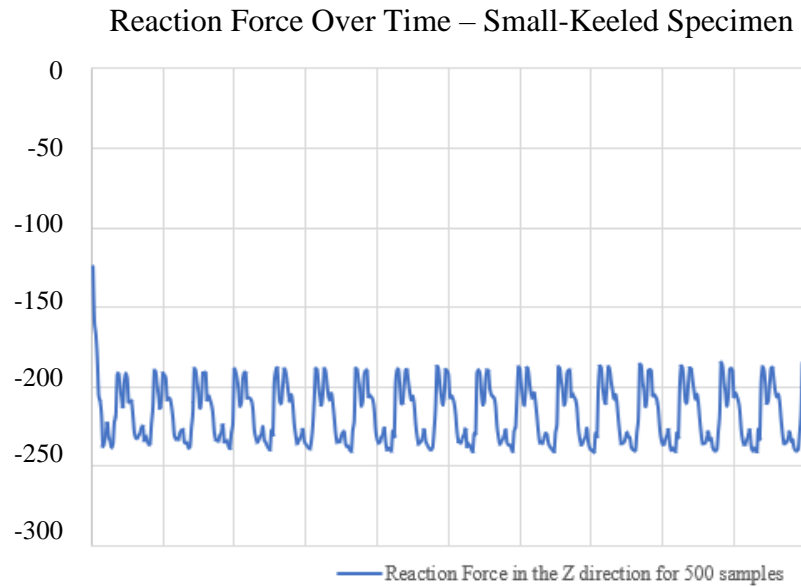


Figure. C1: F_z over Time graph (Small-Keeled Specimen – 500 samples).

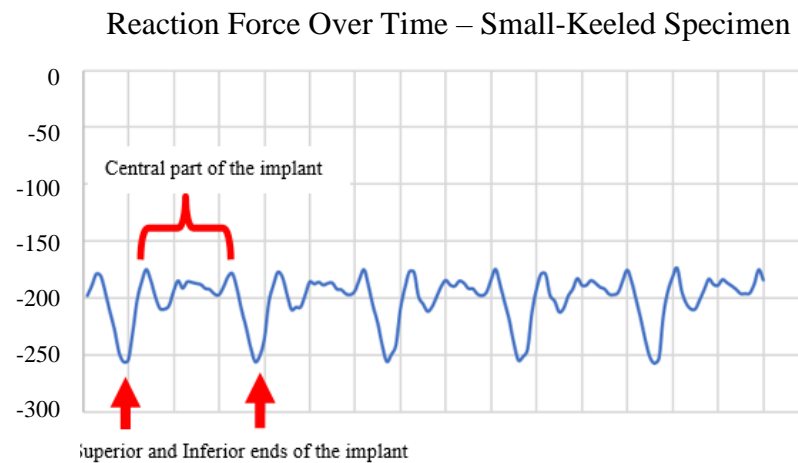


Figure. C2: F_z over Time graph (Small-Keeled Specimen – 100 samples).

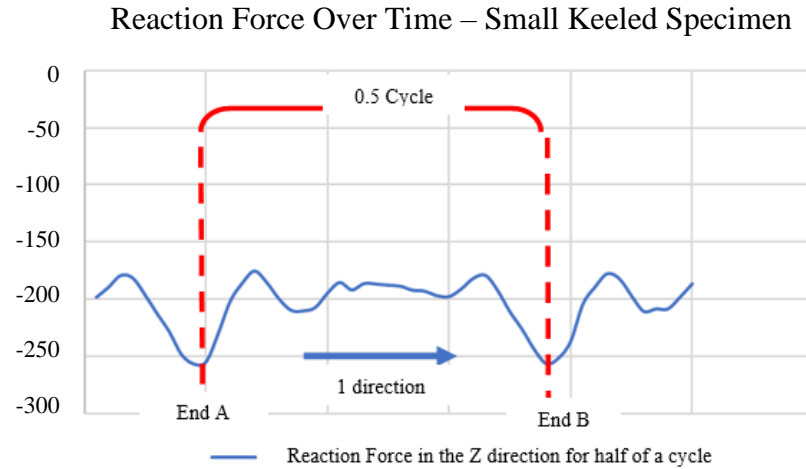


Figure. C3: Reaction Force in the Z direction over Time for half of a Cycle – Small-Keeled Specimen.

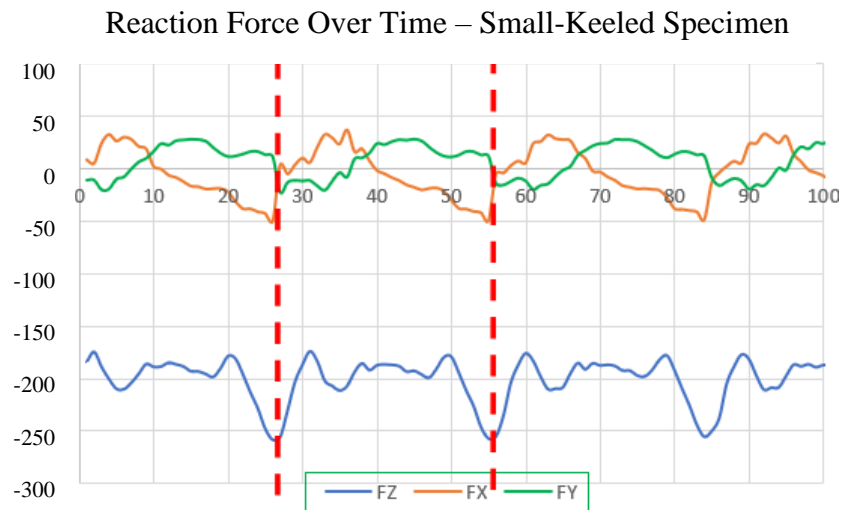


Figure. C4: F_x , F_y and F_z over Time (Small-Keeled Specimen – 100 samples).

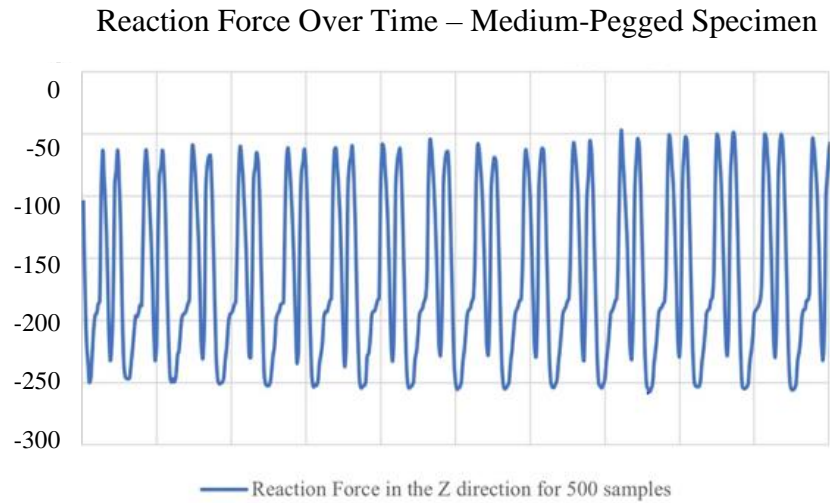


Figure. C5: F_z over Time graph (Medium-Pegged Specimen – 500 samples).

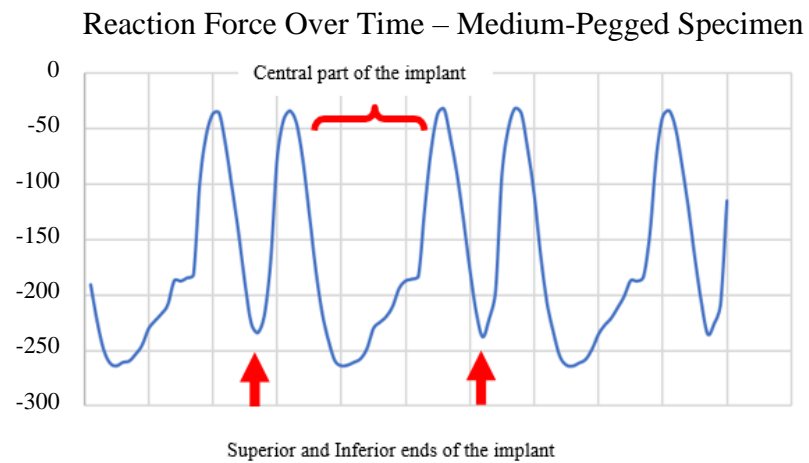


Figure. C6: F_z over Time graph (Medium-Pegged Specimen – 100 samples).

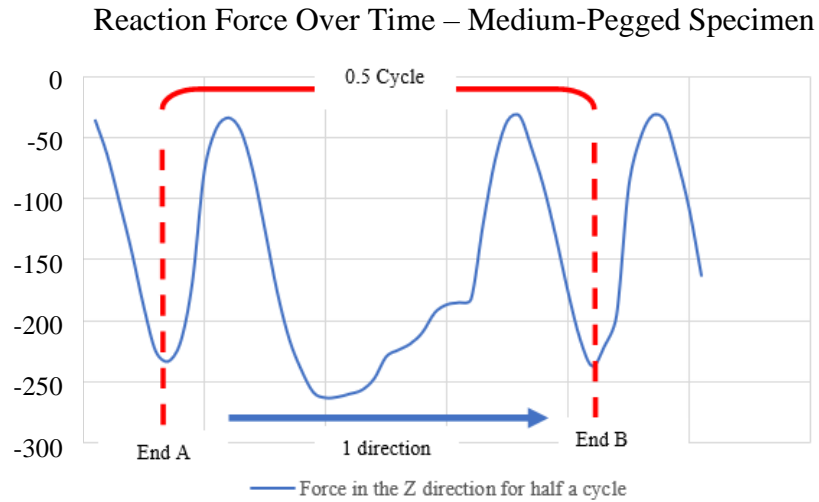


Figure. C7: Reaction Force in the Z direction over Time for half of a Cycle – Medium-Pegged Specimen.

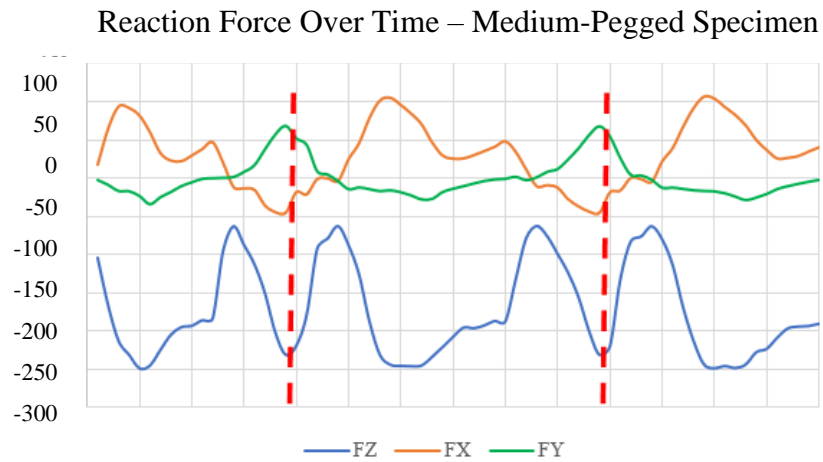


Figure. C8: F_x , F_y and F_z over Time (Medium-Pegged Specimen – 100 samples).

Table. 6: Reaction Forces Average Pilot Test Results.

<i>Tested Specimen</i>	<i>Average Results (200N Load)</i>
<i>Small-Keeled Specimen</i>	$F_X = -11.5602$
	$F_Y = 11.24738$
	$F_Z = -206.781$
<i>Medium-Pegged Specimen</i>	$F_X = 20.23175$
	$F_Y = -11.5444$
	$F_Z = -162.082$

Table. 7: Pilot Test Absolute Maximum and Minimum Reaction Forces in the Z direction.

<i>Tested Specimen</i>		<i>Applied Load (200N)</i>
<i>Small-Keeled Specimen</i>	Max.	268.421
	Min.	97.4266
<i>Medium-Pegged Specimen</i>	Max.	267.07
	Min.	20.5956

Table. 8: Percent Error Results.

		<i>Applied load of 200N</i>
<i>Small-Keeled Specimen</i>		$F_X = -11.5602$
		$F_Y = 11.24738$
		$F_Z = -206.781$
<i>Medium-Pegged Specimen</i>		$F_X = 20.23175$
		$F_Y = -11.5444$
		$F_Z = -162.082$
<i>% Error F_Z</i>	<i>Small-Keeled Specimen</i>	3.3905%
<i>Target load (-200N)</i>	<i>Medium-Pegged Specimen</i>	18.959%

Curriculum Vitae

Name:	Cintya Tavares
Post-secondary Education and Degrees:	Western University London, Ontario, Canada 2016-2020 B.E.Sc. Western University London, Ontario, Canada 2020-2022 M.E.Sc. Candidate
Honours and Awards:	Western Graduate Research Fellowship Western University 2020-2022 Dean's Honor List Western University 2016-2020
Related Work Experience	Teaching Assistant Western University 2020-2022